The Design, Construction and Hypervelocity Impact Testing of a Prototype Orbital Debris and Interplanetary Dust Detector

A thesis submitted for the degree of
Doctor of Philosophy

by

James Stephen Oliver New

School of Physical Sciences

University of Kent
Canterbury
U.K

April 2018

Declaration

This thesis has not been submitted as an exercise for a degree at any other university.

Except where stated, the work described therein was carried out by me alone.

I give permission for the Library to lend or copy this thesis upon request.

SIGNED: 

This thesis is dedicated to the memory of my amazing sister, Alexandra Grace New. You continue to be an inspiration.

Acknowledgements

I wish to thank my supervisor, Dr. Mark Price, for his continued guidance and support throughout my PhD. You are responsible for the fantastic opportunities that have come my way. Thank you. I've thoroughly enjoyed working with you and look forward to our next challenge.

I would also like to thank Mike Cole, your passion and expertise has made this entire project possible. Thank you. I look forward to our future collaboration.

I acknowledge the SDS team, Robert Corsaro and Frank Giovane, for their counsel and support. The advice has been invaluable. The Kapton films and PVDF sensors came in handy too!

Finally, to my wonderful family, and friends who supported me throughout this PhD, financially and emotionally, please accept my sincerest gratitude. This would not have been possible without you.

Abstract

The constant bombardment of millimeter and submillimeter interplanetary dust and orbital debris particles on spacecraft and other space assets leads to long term degradation of exposed surfaces and systems. In the past, post-flight surface analysis on the Space Shuttle provided regular data on these small particles in low Earth orbit. The accumulation of data provided by the characterisation of these particles is required for the development, and updating, of orbital debris environment models, which are essential to predict the conditions in space that can significantly affect the design, operation and cost of spacecraft.

Since the retirement of the Space Shuttle program in 2011, there has been very little new data generated. Consequently, there is now an increasing need for additional information on the characteristics of interplanetary dust and orbital debris for both commercial and research purposes. Dedicated dust detectors, rather than post-flight data collection from collision damage, have successfully demonstrated the potential for characterising particles in the past, and provide the most likely method of analysis going forward. However, current versions have a number of limitations and there is an opportunity to make significant advancements in the next generation of detectors. Designing, testing and analyzing improved detector systems was the primary focus of this research.

Interplanetary dust and orbital debris properties of specific interest include; flux, size, velocity, trajectory, kinetic energy, density and mass. Although previously flown detectors are capable of measuring a number of these parameters, no previous detector has integrated the capacity to measure all of them simultaneously. This thesis describes concepts for a detector capable of collecting, processing and transmitting back the data for all of the parameters listed above and in real time, which is a significant advancement on current state-of-the-art detectors.

Prototypes were designed incorporating selected adaptations of previous detectors, utilising the basic principle of sequential detection gates. Proof-of-concept experiments were conducted on the prototypes using the light gas gun at the University of Kent in order to replicate orbital impacts with simulated space particles in the laboratory. Algorithms written in Python were developed for the five subsystems to analyse data collected by PVDF sensors on each of the three detection gates, and to directly calculate the flux, velocity, trajectory, diameter and kinetic energy of particles interacting with the prototypes. In turn, these results were used to derive mass and density. The characteristics of particles calculated by the subsystems during the experiments were compared with their known properties in order to quantify the accuracy of each measurement. The velocity, trajectory and diameter calculations had an average confidence within 6.5 %, 0.5 % and 10.0 %, respectively. Measurement of the kinetic energy was accurate to ∼26.0 %, which is regarded as a significant step forward. Additionally, the experiments provided evidence that flux models can be accurately measured for particles larger than 50 µm. The prototypes designed and validated in this research can

be used as templates for future detectors capable of providing real-time data on the characteristics of interplanetary dust and orbital debris. These data will contribute directly to the design of future instrumentation and assist the development of more detailed environment models with both commercial and research applications.

Contents

List of Tables

List of Figures

Chapter 1

Introduction

Since the launch of Sputnik-1 in 1957 and with it the dawn of the space age, space exploration has continued to grow and develop into a multi-billion pound industry, demanding close cooperation between governments and commercial companies, such as the NASA–SpaceX and ESA–Airbus partnerships (Anderson, 2013). Modern day life on Earth now relies on a sophisticated network of satellites and a constant orbital presence to support global systems including communication, weather, mapping and transportation. Maintaining such delicate systems requires meticulous organisation and planning, and spacecraft must be equipped with appropriate protection systems to withstand the constant threat from orbital debris and interplanetary dust (OD/ID). The additional mass of these systems can significantly increase the cost of launching and maintaining spacecraft. However, protecting space assets cost-effectively from OD/ID can enhance their operational efficiency and scientific functionality.

The US Space Surveillance Network (SSN) currently catalogues and monitors over 12 000 objects in orbit larger than $\sim$10 cm (Liou et al., 2010) and achieves this with a network of ground-based radars and optical sensors (Sridharan and Pensa, 1998) to warn spacecraft that are on a collision course with orbital debris, so that avoidance manoeuvers can be performed (e.g. the International Space Station (ISS) in 2009). Unfortunately, only a small fraction of the objects in Earth orbit are observable, and

there are millions of objects that are too small (<10 cm) to be detected but are still potentially dangerous (Sanchez-Ortiz et al., 2006).

Software such as the Meteoroid and Space Debris Terrestrial Environment Reference (MASTER; Klinkrad and Sdunnus 1997), developed by the European Space Agency (ESA), and the Orbital Debris Engineering Model (ORDEM; Liou et al. 2002), developed by the National Aeronautics & Space Administration (NASA), attempt to model the orbital debris and micrometeoroid environment surrounding Earth at an altitude between 200 km and 40 000 km (Krisko et al., 2015). Spacecraft designers and operators use these environment models to design spacecraft and their respective protection systems to minimise risk, increase operational efficiency and reduce cost.

MASTER and ORDEM have gone through significant advancements in recent years, such as the ORDEM 3.0 update (Krisko, 2014), but in order to maintain this progress, accurate model validation and continued orbital debris and micrometeoroid characterisation are imperative. Post-flight impact analysis and state-of-the-art in situ impact detectors offer a means for the study of some characteristics (Klinkrad, 2006), but lack the ability to accurately measure others. Advancements in technology have raised the possibility of a next generation detector that will more accurately analyse a wider range of characteristics than those before them, or currently in use, which lack analytical diversity and are limited to the measurement of individual parameters, such as the flux, or velocity, or size, of orbital debris and micrometeoroids. The results of the research reported here will contribute directly to the advancement of the next generation of detectors.

1.1 Research Objective

Background research and collaboration between the University of Kent and NASA suggested that significant improvements could be made in the design of OD/ID detectors in current use, and those undergoing development. The objective of this research was

to design and construct a working prototype of an improved detector, and perform hypervelocity impact experiments as a proof-of-concept. The detector was designed in order to achieve the following scientific objectives in relation to the small OD/ID population:

1. Measure the flux in real time.
2. Calculate the trajectory.
3. Calculate the speed.
4. Determine the size.
5. Determine the kinetic energy.
6. Approximate the mass and density.

In addition to the scientific objectives, the detector was expected to achieve the following design objectives:

7. Include a large enough detection area for reliable statistical sampling of the debris population.
8. Be constructed with low cost materials which are space qualified, or easily qualifiable.
9. Have a lightweight construction to minimise launch costs.
10. Function efficiently with low computational and electrical requirements to minimise operation and maintenance costs.

The design objectives are addressed in Chapter 4 and 5, and the scientific objectives, including the proof-of-concept experiments, are discussed in Chapters 6 – 10.

1.2 Thesis Outline

Chapter 2 provides a general overview of space dust followed by an in-depth discussion about OD/ID that includes details regarding their origin, composition and location. The hazards arising from OD/ID are then outlined with some illustrative case studies. This is followed by a discussion of the different methods of tracking and analysing the debris and dust, concentrating on past, present and future dust detectors.

Chapter 3 provides details about the two-stage light gas gun (LGG) facility at the University of Kent, which was used extensively throughout this research to conduct the proof-of-concept experiments. The details include the operating procedure, construction, and limitations of the LGG.

Chapter 4 present the theoretical design for a detector that is capable of achieving the scientific and engineering objectives identified above. Additionally, there is a detailed description of the physical constituents and hardware that would be required to successfully construct the prototype. Finally, a brief description of the analytical subsystem used to measure each parameter is presented.

Chapter 5 describes each of the prototypes that were constructed during this research and includes an account of the experiments that were conducted during the development of the prototypes. The challenges that were encountered by each prototype are also highlighted, together with the steps that were taken to overcome them.

Chapter 6 begins with a discussion outlining the importance of measuring the impact coordinates of OD/ID on the detector. It then explains how the Impact Cartesian Coordinate (ICC) subsystem measures the coordinates of impacts on the detector.

Chapter 7 outlines why knowledge of the trajectory of OD/ID is of interest. It then explains how the Unit Vector Trajectory (UVT) subsystem calculates the trajectory of OD/ID particles that interact with the detector.

Chapter 8 describes the importance of measuring the velocity of OD/ID. It then explains how the Impact Gate Velocity (IGV) subsystem calculates the speed of OD/ID particles that interact with the detector.

Chapter 9 explains why the size of OD/ID is of interest. It then explains how the Peak-Trough Diameter (PTD) subsystem determines the size of OD/ID that interacts with the detector, and why it is important to do so.

Chapter 10 outlines why the kinetic energy of OD/ID is of interest. It then explains how the Peak-Trough Energy (PTE) subsystem determines the kinetic energy of OD/ID that interacts with the detector. Additionally, a sample of data was used to calculate the mass and density of particles and compared with the known pre-impact particle characteristics.

Each of the Chapters (6-10) describes the proof-of-concept experiments conducted to measure and demonstrate the capability and accuracy of the subsystems, followed by a presentation of the results and a discussion of its overall performance. Furthermore, approximations of particle mass and density are included at the end of Chapter 10.

Chapter 11 summarises the main achievements and findings of this research, and draws conclusions from the results. It also suggests future work that could be conducted to build on, and complement, the advancements described herein.

Appendix A contains additional tables with extended details of each experiment, including the University of Kent shot ID numbers (raw data files can be provided by the author). Appendix B contains supplementary items including labelled screenshots to explain the contents of the raw data files, lookup tables and examples of the Python scripts used by the subsystems.

Chapter 2

Background

Cosmic dust, also referred to as extraterrestrial dust or space dust, has no consistent definition. Lal and Jull (2002) describe cosmic dust as extraterrestrial particles with a diameter between 10^{-4} cm and 10 cm. In contrast, Corsaro et al. (2016) define cosmic dust as particles with a diameter smaller than 2 mm. In this research, dust is defined as all solid particles (i.e. low porosity) with a diameter less than 2 mm. This definition was chosen to maintain continuity between the descriptions of particles with different dimensions used during the experiments in this research, which have diameters ranging between 0.1 mm and 2.0 mm. Cosmic dust can be broadly categorised depending on its astronomical location and behaviour. For example, intergalactic dust is found in the medium between galaxies and is reponsible for intergalactic clouds, which have been known to interfere with intergalactic distance measurements (Kreowski, 2017). Interstellar dust is found in the medium between star systems and is reponsible for interstellar clouds (Juvela, 2015).

Interplanetary dust (ID) is found in the medium between planets in planetary systems and contributes to the material that makes up the Zodiacal cloud in our solar system (Liou et al., 1995) and the population of micrometeoroids (smaller than $\sim$2 mm). In this research, interplanetary dust is defined as all natural particles with a diameter less than 2 mm residing in the solar system. Circumplanetary dust is found in orbit

about individual planets. Planetary rings, such as those surrounding Saturn, are an example of circumplanetary dust. The circumplanetary dust in the solar system surrounding the planets is naturally occuring. However, in Earth orbit, and regions of the solar system visited by spacecraft, an additional form of anthropogenic objects have evolved as a result of human space activities, known as orbital debris (OD) (National Research Council and others, 1995).

2.1 Orbital Debris & Interplanetary Dust

All spacecraft in Earth orbit, and those visiting other astronomical bodies, could encounter OD/ID at some point during their mission. The dynamics of OD/ID particles can significantly affect the design and operation of spacecraft. High energy collisions between spacecraft and OD can have impact velocities exceeding $14\,\mathrm{km\,s^{-1}}$, whereas collisions with ID, such as micrometeoroids, range between $11\,\mathrm{km\,s^{-1}}$ and $72\,\mathrm{km\,s^{-1}}$ (Christiansen, 1993). It is important to mention that the energy of such impacts is not only dependent on the relative impact velocity, but on the velocity ratio. Consider two separate collisions between particles with equal mass and a relative impact velocity of $10\,\mathrm{km\,s^{-1}}$. The first impact, between two particles travelling $10\,\mathrm{km\,s^{-1}}$ and $0\,\mathrm{km\,s^{-1}}$, respectively, and the second, between two particles traveling at $5\,\mathrm{km\,s^{-1}}$ in opposite directions. The kinetic energy between the $10\,\mathrm{km\,s^{-1}}$ and stationary particles would be 100 J. In contrast, the kinetic energy between the $5\,\mathrm{km\,s^{-1}}$ particles would be 50 J. Long term exposure to the bombardment of OD/ID causes degradation of space exposed systems such as solar arrays and thermal protection systems, in addition to windows and unshielded sensitive equipment onboard spacecraft. Furthermore, impacts can directly damage spacesuits worn by astronauts if a collision occurs with the suit during an extravehicular activity (EVA).

There is an added scientific interest in the production and dynamics of ID. The density of ID, which can range between $300\,\mathrm{kg\,m^{-3}}$ and $7800\,\mathrm{kg\,m^{-3}}$ can indicate where,

and how, it was formed (Grün et al., 2012). For example, particles originating from metallic asteroids have a much higher density than porous particles (e.g. chondritic porous ID particles) thought to originate in comets. The trajectory of OD/ID can be used to estimate which parent body a dust particle originated from and potentially provide information on the primitive solar system.

2.1.1 Origin of Orbital Debris and Interplanetary Dust

Much of the interstellar dust, located in the interstellar medium, forms in highly evolved stars, specifically, in the asymptotic giant branch (AGB) stars on the Hertzsprung–Russell diagram. Additionally, a considerable amount of interstellar dust originates in the envelopes of supernovae (SN) explosions (Grün et al., 2012). The dust originating in AGB stars and SN explosions is formed when gas, ejected by stellar winds, cools and condenses to form solid particles (Whittet, 1989). Eventually, accretion of interstellar dust occurs in molecular clouds (Zhukovska et al., 2008), leading to the formation of stars (Greenberg, 2002). Further processing in molecular clouds and star systems leads to the formation of astronomical bodies such as planets, comets and asteroids.

Most ID originates from ejecta escaping cometary nuclei and collisions between bodies in the asteroid and Kuiper belts (Leinert and Grün, 1990). The origin of ID, however, is not exclusive to comets and asteroids. The E-ring of Saturn is an example of ID (Spahn et al., 2006b), formed of ice particles escaping from the subsurface ocean of Enceladus, one of Saturn's moons (Porco, 2017). Figure 2.1 is an image of the ice plumes escaping Enceladus taken from the Cassini spacecraft (Mitri et al., 2018). The trajectory of ID can be used to track a dust particle's path back to its origin. This is important as it could indicate the space weathering and processing that larger bodies experience at different locations in their orbit about the solar system. Comets, for example, undergo periods of high particle ejection during their perihelion, and the trajectory of dust particles could be traced back to a specific comet, at a particular point in space and time.

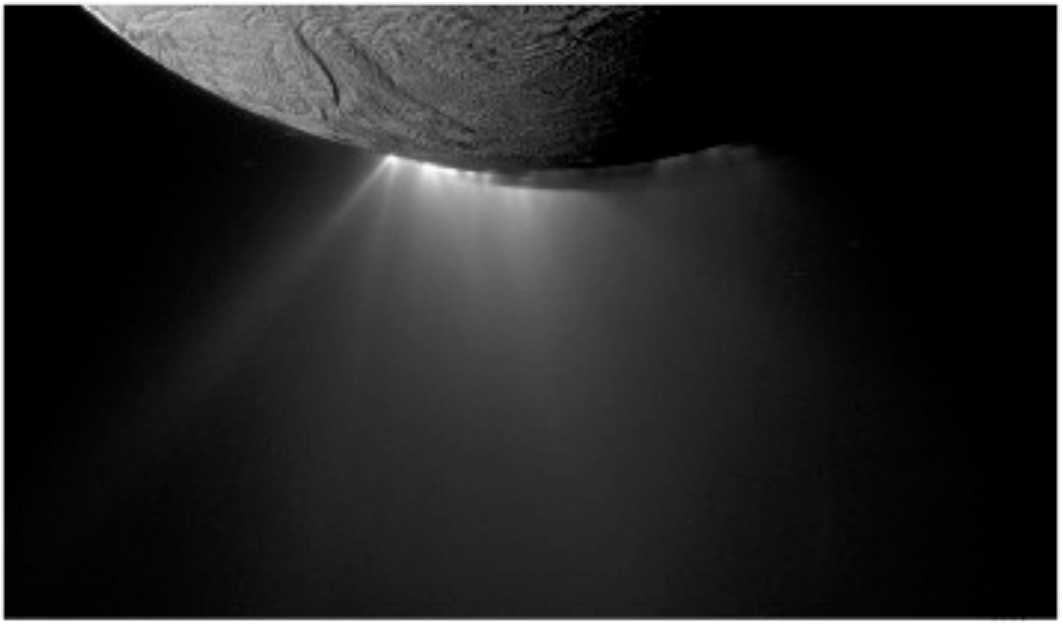

Figure 2.1: Image of the ice plumes escaping from the subsurface ocean of Enceladus. The plumes are illuminated by the sun. Image extract from Mitri et al. (2018).

OD is a by-product of human activities in space, some of which include; the degradation and erosion of discarded upper stages, defunct satellites, pieces of debris from staging and tank explosions that impact one another (Levin et al., 2012). This self-perpetuating process has lead to an accumulation of OD since the beginning of the space age, which ranges in size from microscopic paint flakes to defunct satellites meters in size. It is the OD in the millimeter and sub-millimeter size regime that is of interest to the research described herein.

2.1.2 Composition of Orbital Debris and Interplanetary Dust

The composition of naturally occurring ID is dependent on its origin and formation and can be devided into two categories; (1) micrometeoroids and (2) ice and organic particles.

Micrometeoroids are the most common type of dust found in the vicinity of Earth, and mostly originate from asteroids and comets, but could also come from the Moon,

Mars or other rocky and metallic parent bodies. Micrometeoroids have a rocky and/or metallic composition and commonly consist of the elements silicon, aluminium, magnesium, iron, calcium and oxygen (Ortner and Stadermann, 2009). Real micrometeoroid material is generally polyminerallic, therefore, in this research homogeneous silicate (glass) or metal projectiles were used for simplicity.

The ice and organic particles are rich in water ice and organics, such as the dust that forms Saturn's E-ring (Postberg et al., 2008). These ID particles are not reffered to as micrometeoroids due to their dissimilar composition and origin. Ice particles originate from liquid or frozen parent bodies.

The composition of OD includes the materials that are most abundantly used in spacecraft design and is only defined as OD if it is anthropogenic. Impact analysis on STS windows between STS-50 and STS-110 demonstrated that the composition of OD impacting the STS included aluminium (44%), paint flecks (37%), steel (12%), copper (5%) and titanium (2%) (Christiansen et al., 2004).

2.1.3 Location of Orbital Debris and Interplanetary Dust

ID is not evenly distributed throughout the solar system. Much of the dust populates the asteroid and Kuiper belts and, additionally, a large amount of ID is located in the vicinity of planets, such as the planetary rings of Saturn (Ye et al., 2016), where the E, G and Phoebe rings consist of dust particles in the nanometer to micrometer size range (Spahn et al., 2006a; Throop and Esposito, 1998). A process known as gravitational focusing, described as the attraction due to Earth's gravity of sporadic micrometeoroids, enhances the flux of ID surrounding planets and other large astronomical bodies (Humes, 1993). For low-altitude orbits, gravitational focusing can increase the flux density by up to 60% (Nazarenko and Usovik, 2013). Hence, all of the planets, not just those with rings, have a certain quantity of natural ID surrounding them.

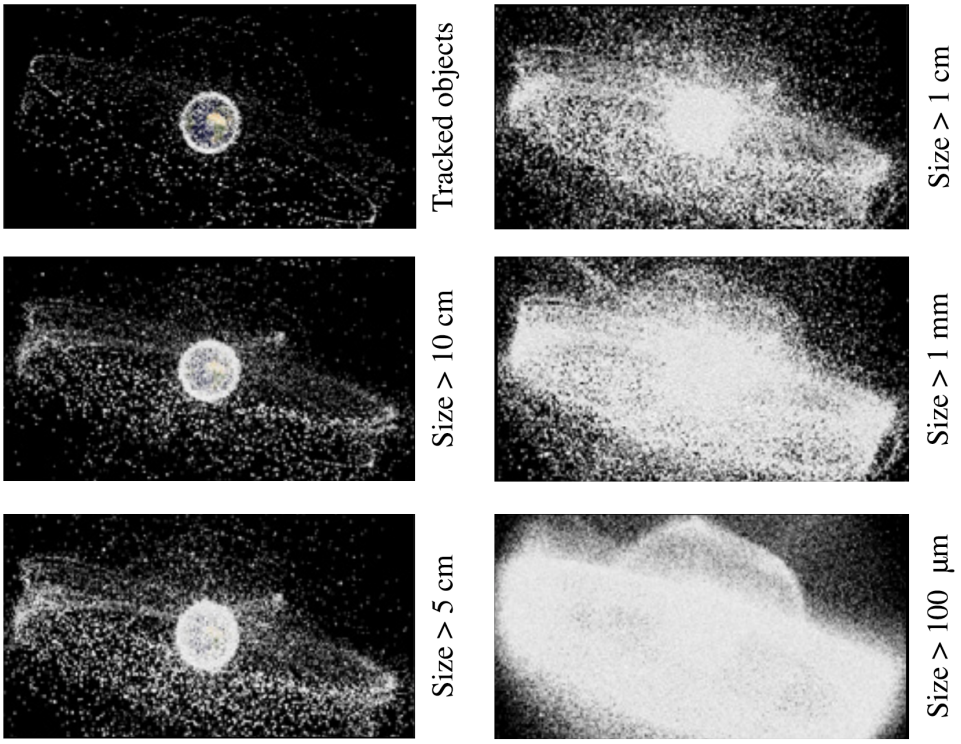

Figure 2.2: Computer generated image of the OD surrounding Earth. Each dot represents the location of an individual piece of debris. Image adapted from Bauer et al. (2014) & Skinner (2017).

Earth is unique in the solar system, as it has natural ID (micrometeoroids) and anthropogenic OD surrounding it, or passing through its vicinity. It is believed that, in the smaller size regime (d $< \sim$30 µm), there are more OD particles surrounding Earth than micrometeoroids (McBride et al., 1999; Zook et al., 1990). As size increases (d $> \sim$30 µm), however, the number of micrometeoroids begins to dominate (McDonnell et al., 1997; Bernhard et al., 1997). The dominance of OD throughout the size distribution, however, is up for debate due to the relatively low sample number of data points available from returned surfacs. The number of OD particles in low Earth orbit (LEO) is in the trillions, and is increasing with each launch and collision (Bauer et al., 2014). Figure 2.2 is a computer generated image, created by NASA, showing the amount of OD surrounding Earth and its location, with respect to diameter.

According to Kessler et al. (1989), mathematical modelling and surface analysis of returned spacecraft suggest that there are approximately 200 kg of micrometeoroids within 2000 km of Earth's surface at any specific time, with the majority of this mass attributed to particles with a diameter of 0.1 mm or smaller. Additionally, there are 300 kg of OD smaller than 1 mm within the same 2000 km region, which is set to increase at twice the rate of larger debris due to fragmentation. Note that the amount of OD has significantly increased since these mathematical models were developed and additional surface analysis of returned spacecraft have been performed.

Naturally occurring micrometeoroids fall within two flux categories: (1) those that orbit around the Sun, with a similiar trajectory to their parent body, and cause periods of high flux, known as streams, and, (2) those with a more diffuse flux and isotropic trajectories, which are known as sporadic (Wiegert et al., 2009). OD, however, is dynamic, which makes its flux highly variable on short time-scales, but, the annual flux of OD/ID in LEO can be considered as a constant. This is helpful when calculating risk profiles for long term missions, but impractical in the short term.

Another mechanism that causes ID particles to migrate inwards from the outer Solar System is the Poynting-Robertson effect, and is defined as the process whereby ID particles slowly spiral into their parent star. Solar radiation, tangental to the motion of a dust grain, causes it to lose angular momentum relative to its orbit. In the Solar System, Poynting-Robertson drag affects dust grains from 1 µm to 1 mm in diameter.

2.2 Risks of Orbital Debris and Interplanetary Dust

Collisions between a projectile and a target, where the projectile velocity exceeds the speed-of-sound within the target material, are known as hypervelocity impacts and typically occur around, or faster than, $3\,\mathrm{km\,s^{-1}}$, depending on the properties of the projectile and target material. During the collision, shock waves propagate through the impacted material and reflect off its surfaces, altering the wave's direction of travel.

The superimposition of advancing and reflected waves leads to increased inertial stress that can exceed the material strength. During this period, solids lose their structural integrity and behave like fluids and, in extreme cases, can be vaporised (Povarnitsyn et al., 2008). Such an impact can have catastrophic consequences for the spacecraft.

The primary risks associated with OD/ID are collisions with spacecraft. This is, to a great extent, due to the typically high speed of objects in space. The average impact speed between OD and spacecraft in LEO is approximately $10\,\mathrm{km\,s^{-1}}$ (Rickman et al., 2017). Furthermore, the average impact speed between micrometeoroids and spacecraft is approximately 15–$20\,\mathrm{km\,s^{-1}}$ (Burchell et al., 2013). The impact speed of micrometeoroids is specifically mentioned as they represent the category of ID most abundently found in the vicinity of Earth and have diameters large enough to threaten spacecraft. Hypervelocity impacts with particles such as these are the reason why OD/ID collisions with spacecraft are considered to be such a serious threat. Therefore, instrumentation (such as the detectors described herein) that can accurately measure this flux is vitally important.

OD/ID collisions can occur on spacecraft windows, structural elements, electronic boxes, solar arrays, radiators, thermal protection system materials covering crew/cargo return vehicles, as well as crew modules (Rickman et al., 2017). Collisions with sensitive components can lead to payload degradation, anomalies or failures in spacecraft operation and scientific investigations, or even loss of mission (Bauer et al., 2014). An example of an impact into glass is shown in Figure 2.3, which is a crater found on one of the space shuttle windows. The crater has a diameter of 10.0 mm and depth of 1.9 mm, with SEM/EDX analysis indicating that it was the result of an impact with a fleck of paint.

The orbital location of spacecraft can also influence the risk associated with an OD/ID collision, as the probability of a collision is determined by the size of the spacecraft and the flux of OD/ID in the vicinity. Spacecraft in LEO are at greater risk than those in geostationary Earth orbit (GEO) due to the larger number of spacecraft in

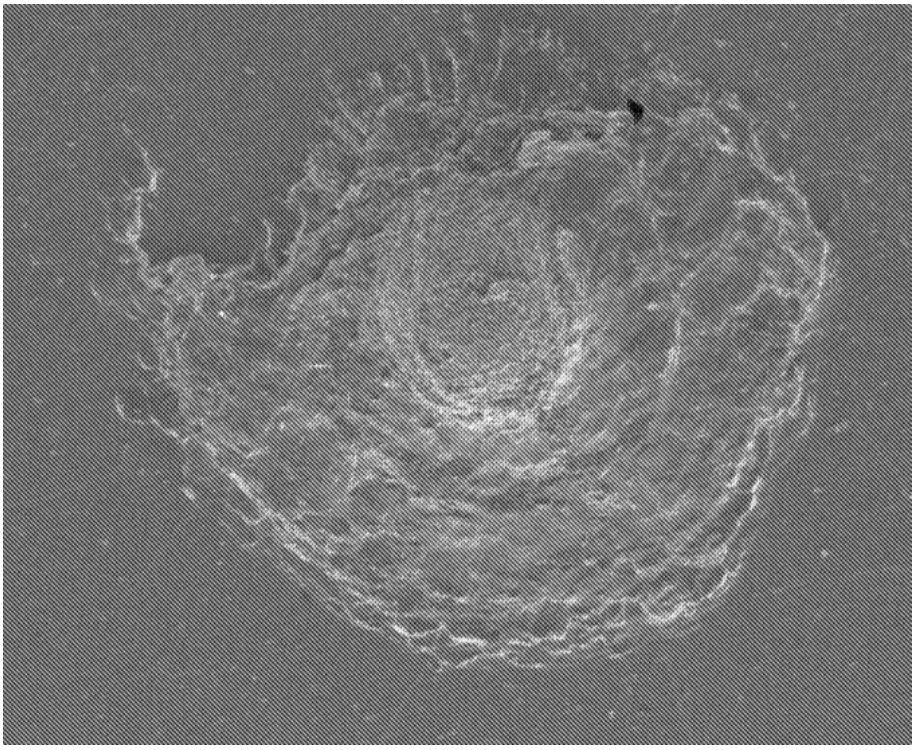

Figure 2.3: Crater caused by a paint particle impact on the STS-92 window. The impact crater has a diameter of 10.0 mm and depth of 1.9 mm. Image extract from Hyde et al. (2001).

LEO. Additionally, spacecraft in lower orbits are exposed to a higher flux of OD/ID. Furthermore, there is a lower statistical probability of collisions between objects in higher orbits, which is a result of the cubic relationship between the volume of a sphere and its radius. In addition to the risk of OD/ID in Earth orbit, spacecraft on fly-by missions with astronomical bodies must account for the risk of collisions with natural ID.

As well as the direct risk to mission success, there is also a financial risk associated with such collisions. Spacecraft components may need to be repaired or replaced more frequently, or sensitive regions of spacecraft may need to be fitted with costly shielding solutions, such as Whipple shields (Christiansen et al., 2009). Repairs must be performed by astronauts during extravehicular activities (EVA), which can be very expensive and high-risk. Another less obvious cost associated with the risk of a catastrophic collision is insurance. In 2015, the total value of insured space assets was ∼20

billion USD and will continue to rise as more objects, such as new constellations of broadband satellites, are placed in orbit (Schaub et al., 2015). More precise characterisation of space dust, made possible by improved detectors, would provide engineers and policy makers (amongst others) with the necessary information to develop shields, protocols and policies to reduce these risks and costs.

2.2.1 Collision Case Studies

Catastrophic collisions between two spacecraft are uncommon, but when they do occur, a significant number of OD are generated. In 2009, an inactive Russian communication satellite, Cosmos 2251, collided with an active commercial (Iridium Satellite LLC) communication satellite (Liou, 2011). Approximately 2000 pieces of debris larger than 10 cm in diameter were produced during the collision, and many thousands more smaller pieces (Figure 2.4).

Impacts between spacecraft and small OD/ID particles, however, occur much more often than large particles. The STS represents a good case study for OD/ID impacts as it underwent frequent and meticulous post-flight impact analysis. For example, one of the crew module windows on STS-92 had to be replaced due to a collision with a fleck of paint (confirmed by SEM/EDX analysis). The resulting impact crater had a diameter of 10.0 mm and a depth of 1.9 mm (Figure 2.3). Penetration equations, based on hypervelocity impact tests in the laboratory, and the known flight details of STS-92, in conjunction with analysis of the crater geometry suggest that the piece of paint had an impact velocity of $9.3\,\mathrm{km\,s^{-1}}$ with a diameter of 0.76 mm and a thickness of 0.3 mm (Christiansen et al., 2004).

The STS-86 mission was also involved in a collision that left a crater in the manifold hard line on one of the radiators with a 0.8 mm diameter and a depth of 0.47 mm. The depth-to-wall thickness ratio was 0.52 and detached spall was found on the inside of the tube. If the collision had penetrated the hard line, Freon coolant would have leaked into space, shortening the mission (Hyde et al., 2001).

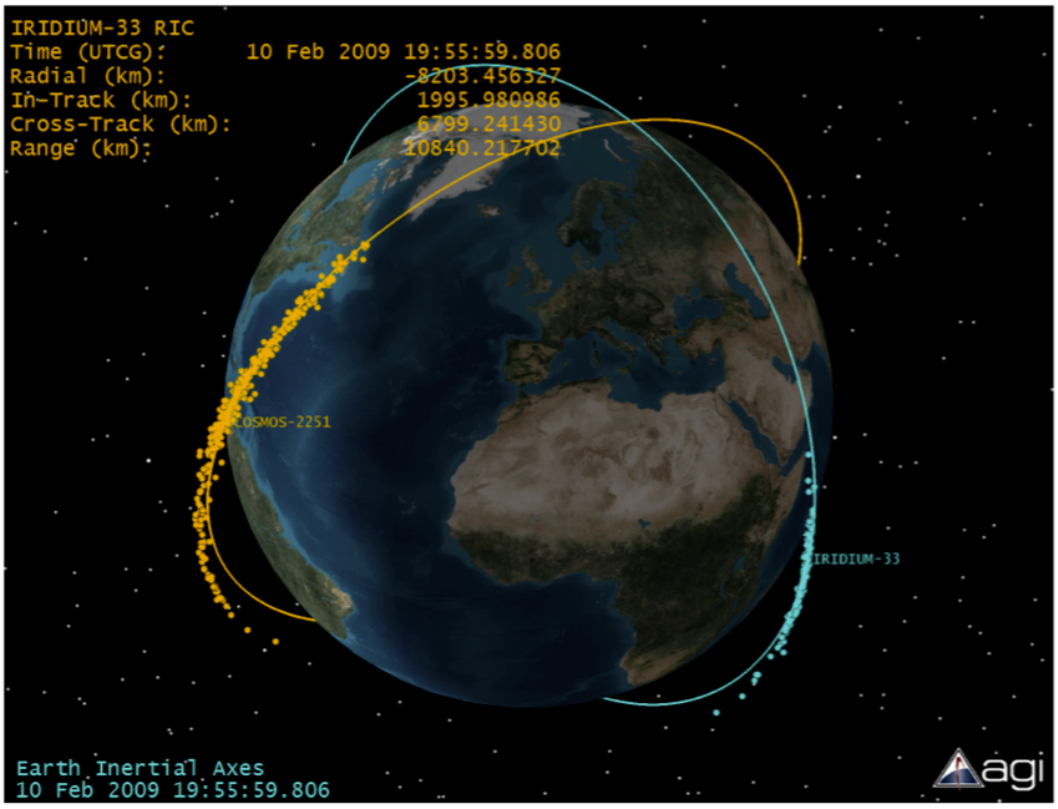

Figure 2.4: View of the Iridium (blue) and Cosmos 2251 (orange) debris 180 minutes post-collision. Credit: Kelso et al. (2009).

Figure 2.5 from Christiansen et al. (2004) shows the 20 most significant impacts, with respect to damage, that occured on the space shuttles between STS-50 in June 1992, and STS-110 in February 2002. This shows that 80 % of the impacts were anthropogenic OD.

In 1993, the OLYMPUS satellite went into an uncontrolled spin during the Perseid's meteoroid shower. Attempts to reorient the spacecraft using the automatic control system were unsuccessful, leading to the early termination of the mission (Caswell et al., 1995). It is beleived that an impact with a small meteoroid could have created structural damage, momentum transfer, or a plasma cloud that triggered a discharge of charged surfaces. Any, or a combination, of these reactions could have lead to the observed loss of attitude control.

Mission #	Orbiter components and payloads				
	Impact location	Damaged material	Hole diameter (mm)	Particle type (SEM/EDXA results)	Estimated particle diameter (mm)
STS-73	FRSI LH #4	Nomex felt	17.0	Orbital debris: Pb, Tin, Ag (solder)	3.0 length × 1.0 diameter
STS-72	Rudder Speed Brake	Inconel	3.4	Orbital debris: aluminum	1.30
STS-75	Payload Pallet Trunnion	Titanium	1.0	Orbital debris: aluminum	0.80
STS-90	DBA Box/Ku-band	Ag–teflon/Al	2.0	Orbital debris: steel	0.60
STS-56	Ku-band antenna	Graphite epoxy	1.4	Meteoritic	0.60
STS-92	Conical Seal Vert. Stab.	Inconel	1.2	Orbital debris: steel	0.42
STS-96	RCC Panel RH2 top	SiC/Carbon	1.2 × 0.85 deep	Orbital debris: aluminum	0.40
Mission #	Payload bay door radiators				
	Impact location	Tape hole diameter (mm)	Facesheet hole diameter (mm)	Particle type (SEM/EDXA results)	Estimated particle diameter (mm)
STS-103	RH #2	4.20	0.70	Orbital debris (Na, K)	1.09
STS-73	LH #4	8.30	1.10	Orbital debris: paint	1.07
STS-109	RH #3	4.00	0.60	Orbital debris: paint	0.86
STS-59	RH #1	5.25	0.95	Meteoritic	0.72
STS-85	RH #4	5.00	1.30	Meteoritic	0.68
STS-71	RH #4	3.10	Unknown	Orbital debris: human waste	0.64
STS-83	RH #4	4.67	0.57	Meteoritic	0.62
STS-93	LH #4	4.10	0.80	Orbital debris: paint	0.60
STS-86	Exterior manifold 1	0.9 diameter	0.5 depth	Orbital debris: steel	0.40
Mission #	Crew module windows				
	Impact location	Average crater diameter (mm)	Crater depth (mm)	Particle type (SEM/EDXA results)	Estimated particle diameter (mm)
STS-92	#2 LH Middle	10.0	1.90	Orbital debris: paint	0.33 × 0.76
STS-110	#2 LH Middle	7.9	0.38	Orbital debris: paint	0.28 × 0.20
STS-94	#7 RH overhead	7.1	0.55	Orbital debris: aluminum	0.25 × 0.28
STS-59	#11 Side Hatch	6.9	0.57	Orbital debris: paint	0.22 × 0.23

Figure 2.5: 20 most significant OD/ID impacts on the windows, radiators and other surfaces of the Shuttle between STS-50 and STS-110. Credit: Christiansen et al. (2004).

In 1996, the French microsatellite Cerise experienced a sudden loss of attitude, despite all of its subsystems being in full working order (Alby et al., 1997). Telemetry analysis indicated that changes in the satellite's moments of inertia had occured, suggesting that the gravity gradient boom had been damaged, leading to a tumbling motion. It was eventually concluded that the boom had been struck by a piece of OD large enough to partially, or fully, sever the boom.

Examples of OD/ID collisions are not limited to Earth orbit. In 1986, ESA's Giotto mission performed a flyby of Halley's comet shortly after its perihelion passage. There were ten experimental instruments on-board the payload: a camera for imaging the comet's nucleus, a photopolarimeter to measure the brightness of the comet's coma, plasma instruments to measure the solar wind/comet interaction, three mass spectrometers for analysing the cometary gas and various dust impact detectors for analysing the dust environment (Reinhard, 1982). The relatively high flyby velocity of $68\,\mathrm{km\,s^{-1}}$

meant that the active experiment time was only four hours. During this time, the Dust Impact Detection System (DIDSY) recorded approximately 1000 impacts with dust particles (Maas et al., 1989). Additionally, the Halley Multicolour Camera (HMC) identified several impacts with dust particles in the 1 mg to 50 mg range (Curdt and Keller, 1990). One impact caused Giotto to spin off its stabilised axis, temporarily preventing the antenna from pointing at Earth. Another impact destroyed the Halley Multicolor Camera, however, it did manage to photograph the nucleus of Halley before the collision (Thomas and Keller, 1988). Giottos's success was a result of a Whipple shield that protected it from large dust grains ejected from Halley's nucleus.

2.2.2 Risk Mitigation

In 1947 Fred Whipple proposed his meteoroid shield as a means of protecting spacecraft (Whipple, 1947), and today, enhanced Whipple shields are still the most effective way of protecting spacecraft from OD/ID. The basic Whipple shield design includes a thin "sacrificial" bumper plate extended from a thicker rear wall. The bumper is designed to shatter incoming projectiles, creating a cloud of material containing both projectile and bumper debris. This debris could be in a solid, molten, or gaseous state, depending on impact speed and composition of projectile. As the cloud expands, it loses momentum/kinetic energy and is distributed over a wide area of the rear wall (Christiansen, 2003). Figure 2.6 demonstrates the mechanics of a basic Whipple shield.

In addition to shielding, spacecraft can be designed in such a way that critical hardware is positioned in protected, or aft facing, regions of the spacecraft. This can reduce the statistical probability of collisions with specific components. The STS and International Space Station (ISS) have both benefited from vehicle design modifications to reduce risks from impacts. For example, automatic shut-off valves were added to the coolant systems on the Shuttle and 0.5 mm thick aluminum doublers were added over the radiator panel coolant tubes to improve the survivability of the shuttle's active thermal control system (Loftus et al., 1997).

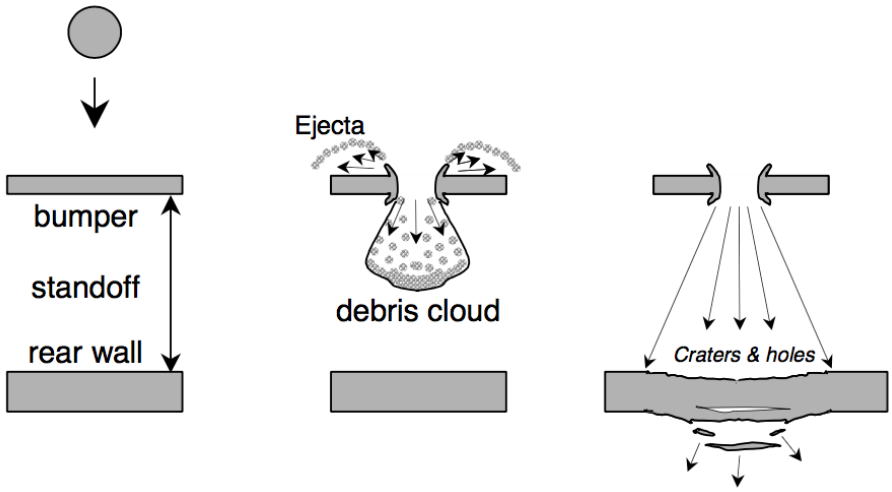

Figure 2.6: A hypervelocity impact on a basic Whipple shield. The cloud is composed of bumper and projectile debris (Christiansen, 2003).

Spacecraft operations can also be designed and controlled to reduce the risks associated with OD/ID collisions. For example, the ISS (and many other satellites) performs avoidance manoeuvres, such as the one in July 2009 where the ISS had to avoid debris from a Proton rocket body (Johnson, 2010). When the Shuttle was in operation it used attitude control to position itself in a favourable orientation, namely tail forward with its payload bay facing Earth, for debris protection (Levin and Christiansen, 1997). Furthermore, most spacecraft are given similar orbits to reduce their risk of collisions and reduce their relative velocities.

In the past, intentional satellite destruction, such as that of Fengyun-1C, has lead to severe and rapid escalations in the number of OD (Liou and Johnson, 2009). Not only do these debris clouds increase the risk imposed on other spacecraft, they often occur in regions that are highly populated with operational spacecraft, which can lead to a cascade effect. In recent years, a new form of indirect risk mitigation has been proposed and discussed, where satellites are equipped with end of life (EOL) disposal systems to prevent the build up of defunct satellites. These EOL systems are designed to either drag satellites into the atmosphere, where they burn up, or transfer them into "graveyard" orbits. Graveyard orbits, however, are not without their own problems as fragments can end up passing through lower orbits if collisions occur.

2.3 Dust Detectors and Sensors

Understanding the properties of OD/ID is necessary for both scientific interest and engineering applications. For example, identifying the properties of ID that originates from comets, asteroids, Kuiper belt objects, planetary satellites and rings can provide information on the primitive solar system. In particular, comets in the outer solar system are thought to contain unprocessed material from the pre-solar molecular cloud and analysis of materials preserved within their impact residues can provide details of this source region. The detector that was designed in this research accurately measures the trajectory of dust particles and if combined with equipment for chemical analysis could provide important evolutionary information.

Impacts with OD/ID can cause catastrophic system failures on spacecraft. In order to reduce these risks, spacecraft use Whipple shielding and strategically placed hardware for protection, but this can be scientfically and financially costly. In fact, the protection of the ISS incorporates tons of material and the associated launch costs are in the order of hundreds of millions of dollars (Lambert et al., 2001). The most heavily protected areas of the ISS have shielding with areal densities of the order of $30\,\mathrm{kg\,m^{-2}}$. Hence, there are engineering and financial advantages associated with a thorough understanding of cosmic dust; for example, shielding can be custom made for specific orbits, attitudes and risk tolerances to reduce mass. Dust detectors and sensors provide the essential data necessary for the design of improved shields.

2.3.1 Detection Methods and Detectors

Throughout the space age many methods of characterising dust have been deployed. Early dust detectors made use of perforations in thin plates to measure the size of dust. The size of a dust particle can be related to the diameter of a hole in the plate which, in turn, can be related to the loss of internal pressure with respect to time (Dietzel et al., 1973). Alternatively, the diameter of the hole can be related to the passage of light

through the hole from a known source to a sensitive detector (Dietzel et al., 1973). An example where such detection methods were used includes the Highly Eccentric Orbit Satellite (HEOS-2; Hoffman et al. 1975).

The development of retrievable spacecraft allowed the use of post-flight impact crater analysis to determine the characteristics of dust. Exposed surfaces on the NASA Space Shuttle would undergo a series of visual inspections after every mission (Bernhard et al., 2001). The entire surface of the Long Duration Exposure Facility (LDEF) was utilised as a dust detector (Zolensky et al., 1992), as well as several dedicated dust detectors onboard, such as the Space Debris Impact Experiment (Humes, 1993) and the Chemistry of Meteoroid Experiment (Hörz et al., 1995). However, post-flight analysis clearly has limitations, in particular it can only measure characteristics such as the flux, size and chemical composition of dust from individual impacts (Kearsley et al., 2007). Additionally, it can be difficult to differentiate between OD and ID on some of the surfaces due to the chemistry involved (e.g. impossible to identify the aluminium oxide OD from solid rocket motor burns when impacted onto aluminium surfaces of LDEF as no distinct chemistry to identify them by).

Dust detectors incorporating polyvinylidene fluoride (PVDF) sensors have become popular due to their versatility and low cost. PVDF sensors are permanently polarised polymers whose capacitance changes in response to mechanical stress caused by, in this case, hypervelocity impacts. The first documented use of PVDF sensors as a dust detector was on the Dust Counter and Mass Analyzer (DUCMA) onboard the two USSR Vega spacecraft that analysed dust in the coma of Halley's Comet (Perkins et al., 1985). Other examples of PVDF dust detectors include the Cosmic Dust Analyzer (CDA) onboard the Cassini-Huygens spacecraft (Srama et al., 2004) and the Dust Flux Monitor Instrument (DFMI) onboard the Stardust spacecraft (Tuzzolino et al., 2003). An example of a PVDF dust detector in Earth orbit is the Cosmic Dust Experiment (CDE) onboard the Aeronomy of Ice in the Mesosphere (AIM) satellite (Poppe et al., 2011).

Resistive-grid dust detectors are another method of measuring the size of dust in space. Copper lines are etched onto a substrate with a known total resistance. When the substrate is penetrated by dust, the copper lines are severed, which changes the overall resistance of the grid. The change in resistance can be related to the number of severed lines which, in turn, can be related to the size of the dust particle. The Space Debris Sensor (SDS; Hamilton et al. 2017), Space Dust Impacts Detector (SDID; Faure et al. 2013) and Space Debris Monitor (SDM; JAXA) are examples of resitive-grid dust detectors.

There are many other examples of exposed spacecraft surfaces and detectors used to investigate OD/ID particles. These include the multi-layer insulation (MLI) from the Space Flyer Unit (passive, non-dedicated), thermal blanket and aluminium thermal control covers from the Solar Max Satellite (passive, non-dedicated), solar cells and radiator panels from the Hubble Space Telescope (passive, non-dedicated), the Microabrasion Foil Experiment (MFE) flown on the space shuttle (passive, dedicated), the Timeband Capture Cell Experiment (TiCCE) on ESA's European Retrievable Carrier (EURECA) (passive, dedicated), the Debris In-Orbit Evaluator (DEBIE) (active, dedicated) and the Geostationary Orbit Impact Detector (GORID) (active, dedicated). Additionally, Figure 2.7 is an extract from Bauer et al. (2014) describing a number of other in-situ detectors and retrieved hardware.

2.3.2 Definition of an Ideal Detector

The ideal detector for characterising the population of OD/ID must be able to measure as many of their properties as possible, at a cost which is proportionate to the utility of the data. Properties of interest include the flux, size, speed, trajectory, kinetic energy, mass, density and chemical composition. Furthermore, it is advantageous to measure these properties in real-time as certain characteristics, such as flux, are time dependent. The capacity to process and send data in-flight would also be a major advantage.

Spacecraft	Detector	m (kg)	Pel (W)	A (m^2)	Sensitivity (g)		Reference
HEOS 2	DD	–	–	0.01	1E−17	1.4E−14	Srama et al. (2000) and Grün (2001)
Helios 1/2	DS	–	–	0.012	1E−17	1.4E−14	Srama et al. (2000) and Grün (2001)
VeGa 1/2	PUMA	10.3	13.5	0.0005	3E−16	5E−10	Grün (2001), Perkins et al. (1985) and
	DUCMA	3.0	2.0	0.0075	1E−13	1E−10	Fechtig and Rahe (1984)
LDEF	IDE	MOS-semiconductor $f = 0.4$ µm; $f = 4$ µm, $A \approx 1m^2$					McDonnell et al. (1993), Mandeville
	MAP	Al foil $f = 2$ µm; $f = 31$ µm, brass foil $f = 5$ µm					(1991), Stabroth et al. (2008) and
	SDIE	Al plate $f = 4$ mm, $A = 26$ m^2					Oliver et al.
	CME	Al plate $f = 3.2$ mm, $A = 1.1$ m^2					
	FRECOPA	Glass metallised foils $A = 0.2$ m^2					
Giotto	PIA	10.3	13.5	0.0005	3E−16	5E−10	Fechtig and Rahe (1984), Grün
	DIDSY	2.30	1.90	–	1E−16	1E−02	(2001), Grayzeck (2013), McDonnell
	CIS	–	–	0.10	>1E−10		et al. (1989), Mandeville et al. (1982),
	IPM-P	–	–	0.01	>2E−17		McDonnell (1987) and Fechtig and
	IPM-M	–	–	–	1E−10	1E−03	Rahe (1984)
Galileo	DDS	4.20	5.40	0.10	1E−16	1E−06	Grün et al. (1992) and Grün (2001)
Hiten	MDC	0.61	1.80	0.01	1E−16	1E−07	Iglseder et al. (1993)
Ulysses	DUST	3.75	2.0	0.10	1E−16	1E−6	Angrum (2014)
BremSat	MDC	0.61	1.80	0.01	1E−16	1E−07	Iglseder et al. (1993)
Nozomi	MDC	0.7	3.78	0.01	1E−15	1E−08	Senger (2002) and Grayzeck (2013)
EuReCa	TiCCE	Al foil, f = 0.85; 1.85; 5 µm, $A \approx 0.25$ m^2					Shrine (1999)
Clementine	OMDC	0.5	0.01	0.16	–	–	Kinard et al. (2001)
Express-2	GORID	4.48	3.40	0.1	>1E−14		Drolshagen et al. (2001)
Cassini	CDA	17.15	17.00	0.1	1.3E−16	1.2E−04	Srama et al. (2000) and Grün (2001)
	QP	3.50	1.70	0.10	8E−09	8E−03	
	IID	8.00	8.00	0.10	1E−15	1E−07	
	CAT	7.40	9.00	0.02	1E−15	1E−07	
	HRD	1.10	0.70	0.006	8E−13	1E−04	
Stardust	CIDA	–	–	0.01	–	–	Kissel et al. (2003), Grayzeck (2013),
	DFMI	1.76	1.80	0.022	1E−11	1E−04	Srama et al. (2000) and Tuzzolino
	LAMS	–		0.33	5E−07	2E−03	et al. (2000)
ARGOS	SPADUS	23.60	6.30	0.058	5E−11	1E−05	Tuzzolino et al. (2001)
Rosetta Orbiter	GIADA	5.90	20.70	0.01	–	–	Bussoletti et al. (1999)
	GDS/IS	3.32	7.50	0.01	–	–	
	MBS	0.17	0.05	0.3	1E−10	1E−04	
Rosetta Lander, Philae	DIM	0.41	0.17	0.007	6E−10	8E−04	Seidensticker et al. (2007)
PROBA	DEBIE-1	2.38	3	0.02	1E−14	1E−07	Kuitunen et al. (2001), Drolshagen
							(2003) and Schwanethal et al. (2005)
Cosmos-Oberstufe	MDD	1.40	–	0.1	>1E−05		Janovsky et al. (2005) and Spencer
							et al. (2005)
EuTEF/ISS	DEBIE-2	2.94	4	0.03	1E−14	1E−07	Kuitunen et al. (2001), Drolshagen
							(2003) and Schwanethal et al. (2005)
Spectr-R	MDD3	3.50	10	0.12	>1E−09		Schäfer et al. (2009)
IKAROS	ALADDIN	0.25	–	0.54	–	–	Yano et al. (2011)
Bepi Colombo MMO	MDM	0.60	4.00	0.006	1E−14	1E−08	Nogami et al. (2010) and Kobayashi
							et al. (2012)
Concept	RGS	1.80	1	1	>2E−07		Liou et al. (2009)
Concept	QPS	0.16	0.01	0.01	$> 2E-07$		Kitazawa et al. (2009, 2010)
Concept	AIDA	3	5	0.04	–	–	Herbst et al. (2009)
Concept	cal	–	–	0.003	1E−12	1E−03	Kobusch et al. (2009)
Concept	vel	–	–	–	$> 1E-08$		Bunte et al. (2008)
Concept	–	–	10	–	–	–	Liou et al. (2005)

Figure 2.7: Examples of in-situ detectors and retreived hardware. Extract from Bauer et al. (2014).

There are multiple examples of detectors capable of measuring one or two specific properties of OD/ID, however, acquiring information on all of the properties listed above using an all-in-one detector would significantly improve the data quality and subsequent analyses. Additionally, a single detector, capable of measuring these properties, would significantly reduce the financial costs associated with the development and launch of multiple detectors, each designed to measure only one or two parameters.

In summary, the ideal dust detector would measure the flux, size, speed, trajectory, kinetic energy, mass, density and chemical composition of OD/ID simultaneously, and

in real-time, rather than through post-flight analysis, with the capacity to process data in-flight and send it back to Earth using relatively low computing power.

Physically, the detector must be constructed of space qualified, or easily space qualifiable, materials (discussed further in Section 5.3.2). There are strict regulations regarding materials used in space, and not all materials are appropriate, regardless of their scientific advantages. Additionally, the detector must be low mass and low power, to reduce launch and maintenance costs, respectively. Finally, the detection area must be capable of measuring large dust, which has a low impact probability, within a reasonable time (2-3 years), as extending the duration of a dedicated mission to collect data on larger particles is expensive.

Chapter 3

Light Gas Gun

The detector in this research is designed to collide with OD/ID while in operation and uses three impact detection gates (IDGs) for its measurements. In order to validate the performance of the prototypes of the detector, it was necessary to demonstrate its capabilities under test conditions. Hypervelocity impacts between OD/ID and the different prototypes can be simulated in the laboratory, by accelerating millimeter and sub-millimeter particles, which subsequently impact the detector, to velocities in the kilometres per second range.

Two-stage light gas guns (LGGs), such as the facility at the University of Kent (UKC), were developed specifically for the study of hypervelocity impacts between millimetre/centimetre sized projectiles, accelerated to speeds above a few kilometres per second (Crozier and Hume, 1957), and targets. It is worth mentioning that other facilities, such as Van de Graaff accelerators and railguns, are capable of accelerating projectiles to hypervelocity, but were not used in this research. The UKC LGG is capable of firing 0.1 mm – 3.0 mm diameter projectiles at velocities up to $\sim$8.5 $\mathrm{km\,s^{-1}}$ (Loft et al., 2013), and was used extensively in designing the terminal IDG (described in Chapter 5), and for conducting the subsystem proof-of-concept experiments. For improved reliability, the LGG was operated in the 2 $\mathrm{km\,s^{-1}}$ to 5 $\mathrm{km\,s^{-1}}$ velocity range throughout this research, providing a means of demonstrating the detectors perfor-

mance accross a range of velocities. Projectiles were not accelerated to velocities of $\sim 8.5\,\mathrm{km\,s^{-1}}$ as these shots can damage the LGG.

3.1 LGG Overview

Light gas guns use the flow of a highly compressed gas through a small aperture to accelerate projectiles. The blast from a shotgun cartridge is used to drive a piston, which compresses a gas and when the gas reaches a specific pressure (typically ∼kbar), it ruptures a disc, which allows the gas to flow through the aperture and accelerate the projectile.

Figure 3.1 is a schematic of the LGG facility at the University of Kent. The key components have been labeled and a description of each component is included below, with an explanation of its specific function.

(1) Firing Pin and (2) Firing Mechanism

The firing pin is a solid cylinder that is used to ignite the shotgun cartridge. A pendulum is used to drive the firing pin into the firing mechanism, which in turn, ignites the cartridge. The firing pin slots into the firing mechanism, which is screwed onto the powder chamber.

(3) Powder Chamber

The powder chamber is used to house the shotgun cartridge. It is screwed in place between the firing mechanism and the pump tube. An O-ring is used to seal the connection and prevent the loss of pressure during ignition.

(4) Piston

The piston is a nylon cylinder with a similar diameter to the pump tube and is used to compress the light gas. It has two rubber O-rings around its circumference to ensure a tight seal and prevent loss of pressure. Grease is applied to the surface of the piston as a lubricant, allowing it to travel smoothly through the pump tube. It is inserted into the pump tube at the opposite end to the central breach.

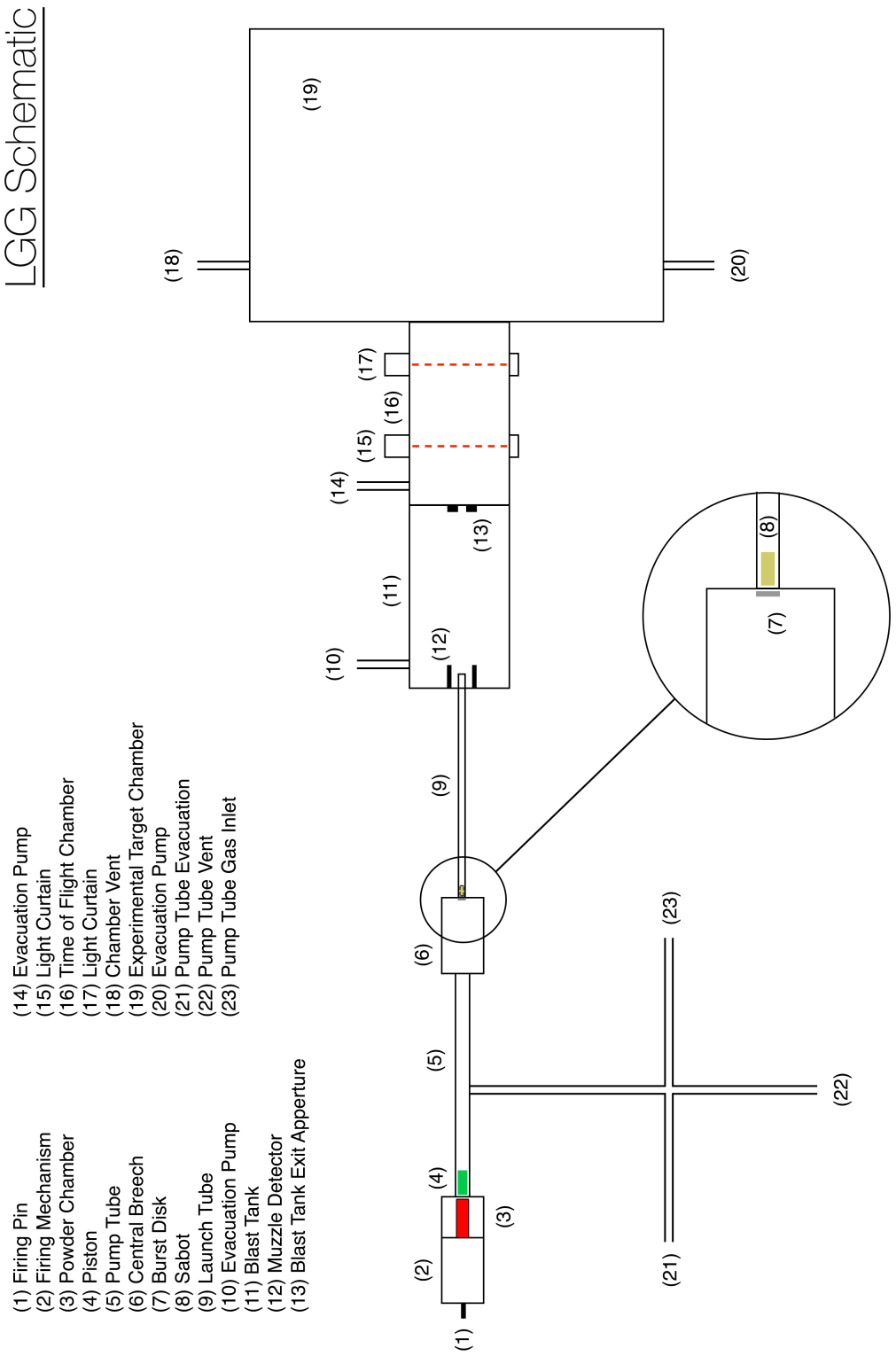

Figure 3.1: Schematic of the LGG facility at UKC. Not to scale.

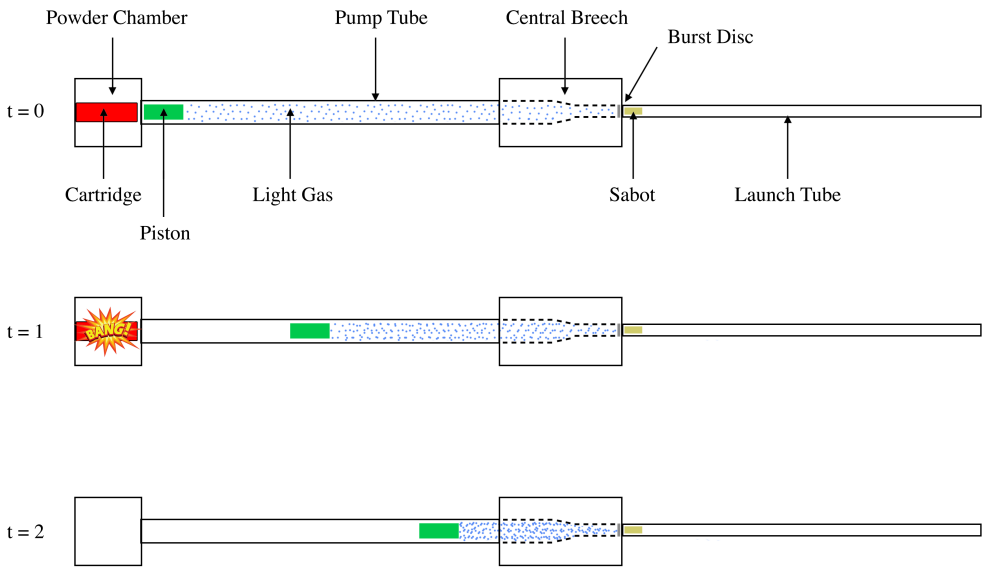

Figure 3.2: Schematic of the pump tube in operation. The cartridge ignites, driving the piston through the pump tube to compress the light gas.

(5) Pump Tube

The pump tube is filled with a gas of low relative molecular mass (typically hydrogen, helium or nitrogen), where it is stored until the gun is ready to be fired. The gas is pumped into the tube through a valve until a specific pressure is reached, depending on the desired velocity of the shot. The pump tube is screwed in place between the powder chamber and the central breech.

The ignition of the cartridge creates a gas blast that drives the piston through the pump tube at a velocity of $\sim 1\,\mathrm{km\,s^{-1}}$. This, in turn, compresses the light gas, as shown in Figure 3.2. Furthermore, additional pressure is created due to the increased temperature of the gas, which further increases its velocity.

(6) Central Breech

The central breech connects the pump tube and launch tube. It acts as a funnel compressing the light gas further as it moves from the pump tube into the launch tube. It is a reinforced cylinder designed to withstand the high pressure that builds up prior

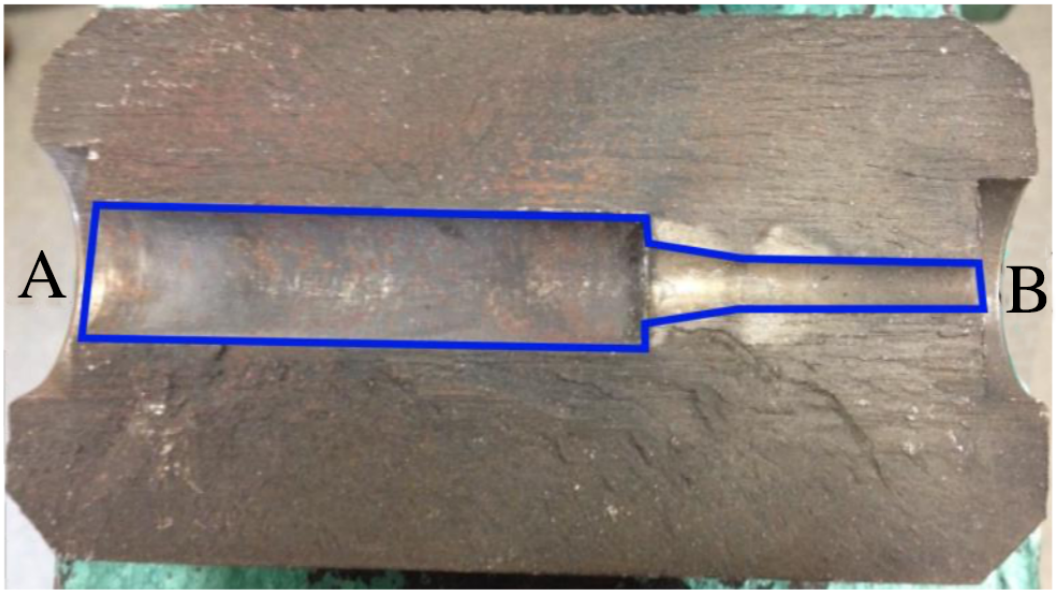

Figure 3.3: Photograph of the cross-section of the central breech. A and B represent where the pump tube and launch tube attach to the central breech, respectively. The change in aperture has been highlighted in blue.

to the rupturing of the burst disc. The central breech is located between the pump tube and launch tube, and held in place by an external clamping mechanism. O-rings are used to prevent gas leaks and maintain pressure in the pump tube.

Figure 3.3 shows a cross-section of the central breech. The left hand side (A) and the right hand side (B) show where the pump-tube and launch-tube attach to the central breech, respectively. Notice how the aperture changes inside the central breech, highlighted in blue.

(7) Burst Disc

The burst disc is a thin aluminium disc with a 12.7 mm diameter and is used to maintain pressure in the pump tube. When the desired pressure is achieved the burst disc ruptures, allowing the gas to flow from the pump tube into the launch tube, accelerating the sabot. The burst disc is positioned between the central breech and the launch tube.

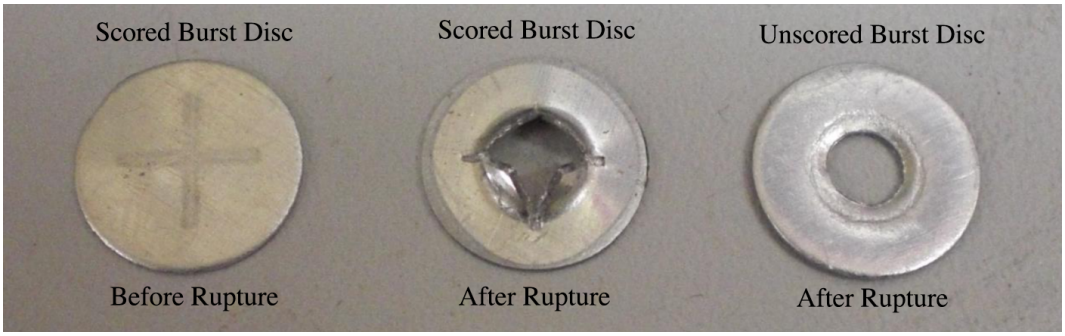

Figure 3.4: Photograph of a scored burst disc before and after rupture (left and middle) and an unscored burst disc after rupture (right).

Figure 3.4 shows a burst disc before and after rupture. Burst discs are scored with a central cross, depending on the desired velocity of the shot, to ensure they rupture into four "petals" at the required gas pressure. Scores are made with a pressure of either 7 kN or 9 kN, depending on the launch tube, for velocities below $\sim$5 km s^{-1}. Un-scored burst discs are used for velocities above $\sim$5 km s^{-1}.

(8) Sabot and Projectile

Light gas guns use the flow of gas to accelerate projectiles through a launch tube towards a target. Efficient acceleration occurs when the diameter of the projectile is similar to the bore of the launch tube. Projectiles with different diameters can be launched by placing them into a cylindrical container. These are known as sabots and they have a precise diameter that matches the bore of the launch tube. This tight fit allows the compressed gas to push the sabot through the launch tube without loss of pressure. There are different types of sabot, solid or split, and they can range in composition.

The sabots that were used during the proof-of-concept experiments in this research were 4-way split sabots. These are isoplast cylinders with a diameter of 0.170" and a hole in their central axis, where the projectile is positioned. They are divided into four identical pieces with serrated edges that are designed to keep the sabot intact during its acceleration through the launch tube, see Figure 3.5.

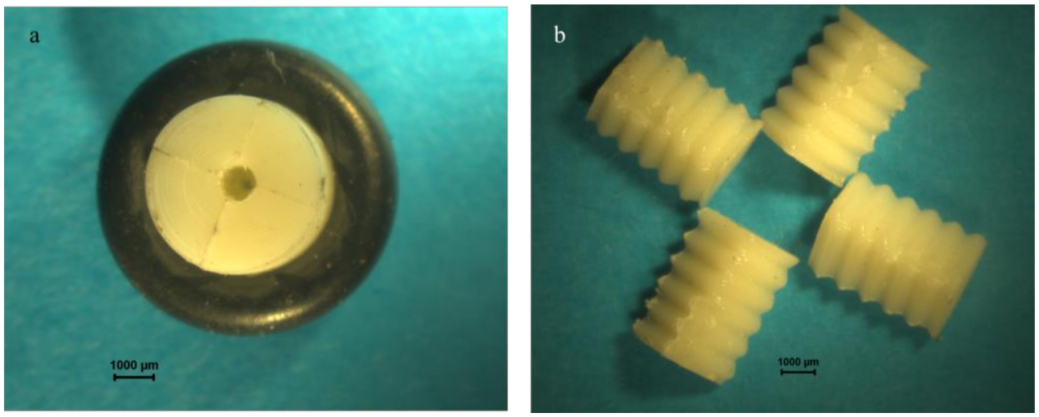

Figure 3.5: Photograph of a 4-way split sabot used in the LGG facility at the University of Kent.

Using a low power microscope, the projectile is carefully secured into the sabot and inserted into the launch tube. The split sabots can accommodate individual projectiles with a diameter up to 3.0 mm. Smaller particles, micrometers in diameter, can also be accelerated (and detected) in the split sabots as buckshots.

(9) Launch Tube

The launch tube is where the sabot and projectile are accelerated. There are two types of launch tube, rifled and non-rifled, which are interchangeable depending on the velocity, material, shape and size of the projectile. When using a split sabot, rifled launch tubes are used to rotate it. The angular momentum caused by this rotation allows the segments of the sabot to separate in the blast tank, which is necessary to prevent the sabot impacting the target. A non-rifled launch tube is used when accelerating projectiles without a sabot, such as frozen projectiles, where the rifling would cause the projectile to shatter. The launch tube is located between the central breech and the blast tank.

Prior to each shot the launch tube is pumped down to a vacuum of 0.5 mbar to prevent air resistance (ahead of the sabot) from slowing down the projectiles. When the desired pressure in the pump tube is achieved, and the burst disc ruptures, the light gas flows through the launch tube, driving the sabot (Figure 3.6).

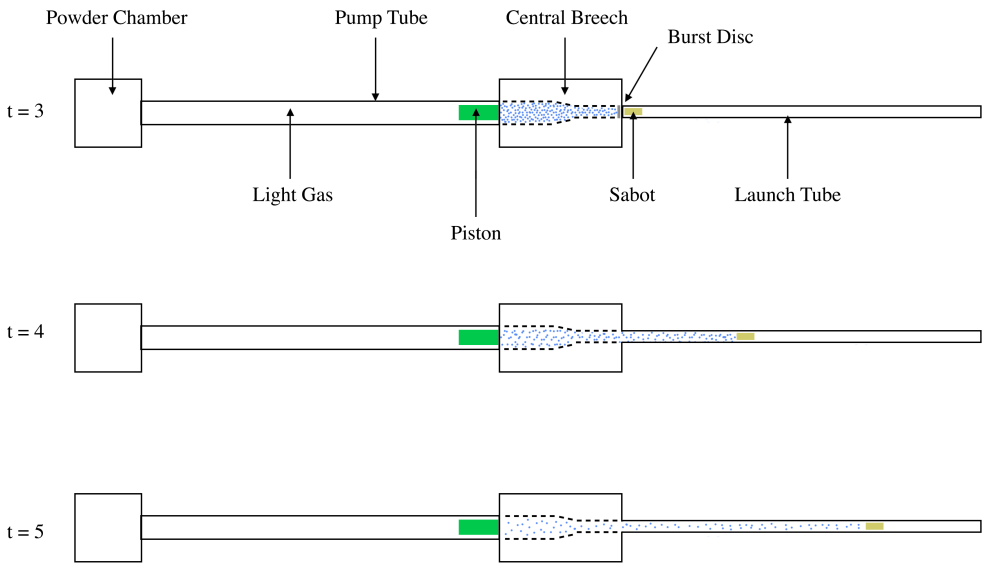

Figure 3.6: Schematic of the launch tube in operation. The burst disc ruptures allowing the gas to accelerate the sabot through the launch tube.

(11) Blast Tank, (12) Muzzle Detector and (13) Exit Aperture

As the sabot enters the blast tank it is no longer confined to the narrow barrel of the launch tube. The angular momentum of the sabot allows the segments to separate while the projectile maintains its original trajectory. The blast tank exit aperture is located at the end of the blast tank. The aperture is large enough to allow the projectile to pass through, while preventing the segments of the sabot from reaching the target chamber.

The muzzle detector is located at the start of the blast tank where the launch tube ends. It uses lasers to detect the sabot as it enters the blast tank. Additional sensors record when the sabot segments impact the blast tank exit aperture. These timings are used to calculate the velocity of the sabot (Figure 3.7).

(16) Time-of-Flight Chamber

The time-of-flight chamber is where the velocity of the projectile is measured. Two light curtains ((15) and (17) on Figure 3.1), with a 0.499 m separation, are connected

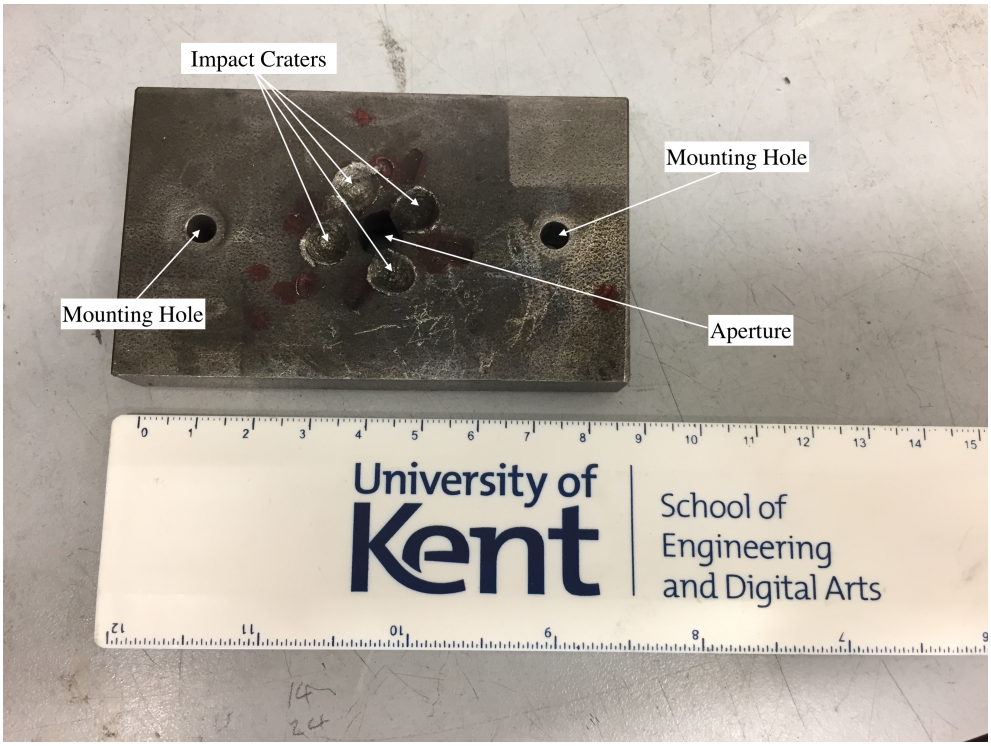

Figure 3.7: Photograph of an exit aperture. Notice the four impact craters caused by the segments of the sabot.

to an oscilloscope. The time is recorded when the projectile interrupts each light curtain, which can be used in conjunction with the separation distance to calculate the time of flight over their separation and, hence, velocity. The accuracy of the velocity measurements is correct to within ±1 % (Burchell et al., 1999).

(19) Target Chamber

The target chamber is where targets and experiments are placed and has dimensions of 1.14 ×1.14 × 1.15 m (kindly supplied to the University of Kent in 2012 by NASA). Small targets can be attached to a mount on the door of the target chamber and the mount is positioned so that impacts occur in the central region of the target. Larger targets, such as the prototypes used in this research, can be placed on freestanding jacks within the target chamber, as seen in Figure 7.3. Additional mounts allow for rotating and heated targets. There are electronic feed-throughs and two windows in the chamber for additional instrumentation and photography.

3.2 Velocity-Gas Relationship

The velocity of the sabot and, in turn, the projectile is dependent on the expansion velocity of the light gas. Hence, the desired velocity can be set and controlled by varying the pressure and temperature of the gas.

The maximum velocity, v_{max} ($\mathrm{m\,s^{-1}}$), of the particles in the gas is given by (Doolan, 2001):

$$v_{max} = \frac{2}{\gamma - 1} c \tag{3.1}$$

Where γ is the specific heat ratio between the compressed (via the piston) and uncompressed state of the (non-ideal) gas and c ($\mathrm{m\,s^{-1}}$) is the speed of sound and is given by the equation:

$$c = \sqrt{\frac{\gamma R T}{m}} \tag{3.2}$$

Where R ($\mathrm{J\,kg^{-1}\,K^{-1}}$) is the gas constant, T (K) is the temperature of the gas and m (g) is the mean molecular weight.

Hence, the expansion velocity, c, of a gas released from a compressed state depends on the inverse of the square root of the mean relative molecular mass, m, and the lighter the second-stage gas, the greater the final velocity of the projectile (Burchell et al., 1999).

3.3 Summary

The LGG facility at the University of Kent (Figure 3.8) can accelerate particles of sizes between 1.0 µm and 3.0 mm to speeds in excess of $7.0\,\mathrm{km\,s^{-1}}$. That, coupled with the large target chamber and extensive set of measurement instrumentation made it the ideal test-tool for the development of the detector in this research.

Figure 3.8: Photograph of the LGG at the University of Kent.

Chapter 4

The Orbital Debris & Interplanetary Dust Detector (ODIN)

The Orbital Debris & INterplanetary (ODIN) dust detector was conceived, designed and tested as the main focus of this research. It provides proof-of-concept data that a new type of active and direct measurement instrument that analyses OD/ID and provides real-time data is possible. An instrument such as this could prove to be a valuable asset in the ongoing development of OD/ID environment models, due to its low cost and extended operation time, large detection area and comprehensive in-situ OD/ID characterisation. ODIN uses three impact detection gates with strategically placed piezo-strain acoustic sensors to measure shockwaves that are generated during hypervelocity impacts with millimetre and sub-millimetre OD/ID dust particles.

ODIN has five analytical subsystems that measure the (1) flux, (2) trajectory, (3) speed, (4) diameter and (5) kinetic energy of OD/ID particles that interact with it. Additionally, the mass, momentum and density of OD/ID can be derived from the primary data with various levels of approximation.

4.1 ODIN Physical Overview

ODIN was, from its initial inception, envisioned as a system with three impact-detection-gates (IDGs) that are responsible for all of its data acquisition. The first two IDGs are used for time of flight calculations and the third is used to acquire kinetic energy readings of impacting particles. Individual diagnostic subsystems are then used to analyse the data and characterise OD/ID. The three IDGs (primary, secondary and terminal) are shown schematically in Figure 4.1, illustrating their configuration on ODIN.

The primary IDG is located at the front of the system, with the terminal IDG at the back, and the secondary IDG located in-between them. The blue line in Figure 4.1 represents an OD/ID particle, which passes through the primary and secondary IDGs and is captured by the terminal IDG.

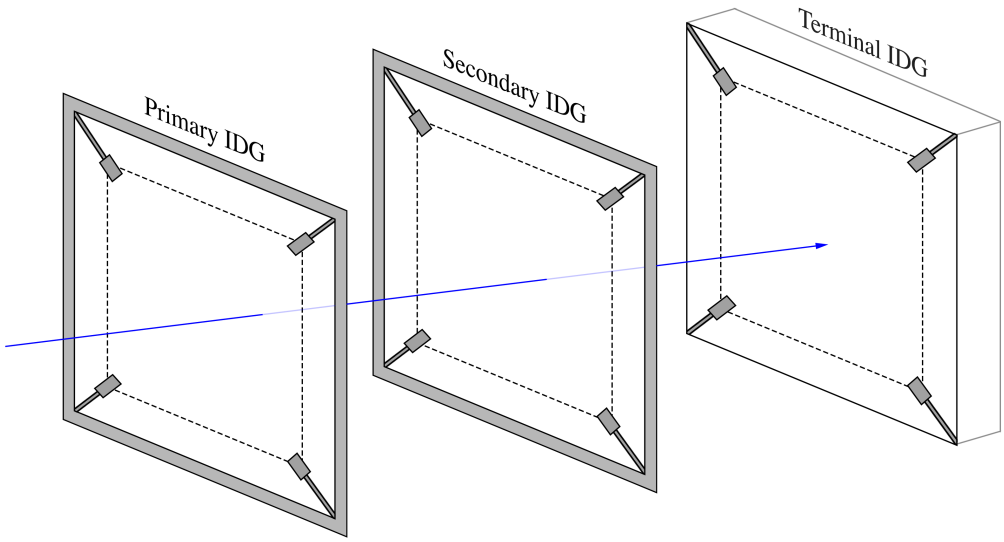

Figure 4.1: Schematic showing the configuration of the primary, secondary and terminal IDGs (not to scale). The blue line represents the passage of an OD/ID particle through the detector.

4.2 The Primary and Secondary IDG

The primary and secondary IDGs are composed of a thin (25 µm) Kapton substrate that is mounted on a rigid aluminium frame. Four polyvinylidene fluoride (PVDF) acoustic impact sensors are orthogonally adhered to the aft facing sides of the Kapton films. The PVDF sensors are positioned as close to the corners as possible, maximising the sensitive area of the detector. Figure 4.2 is a schematic of the primary and secondary IDGs showing the Kapton substrate, rigid frame and PVDF sensors.

The area within the dotted line on Figure 4.2 represents the acoustically sensitive region of the primary and secondary IDGs. Impacts that occur in this region are

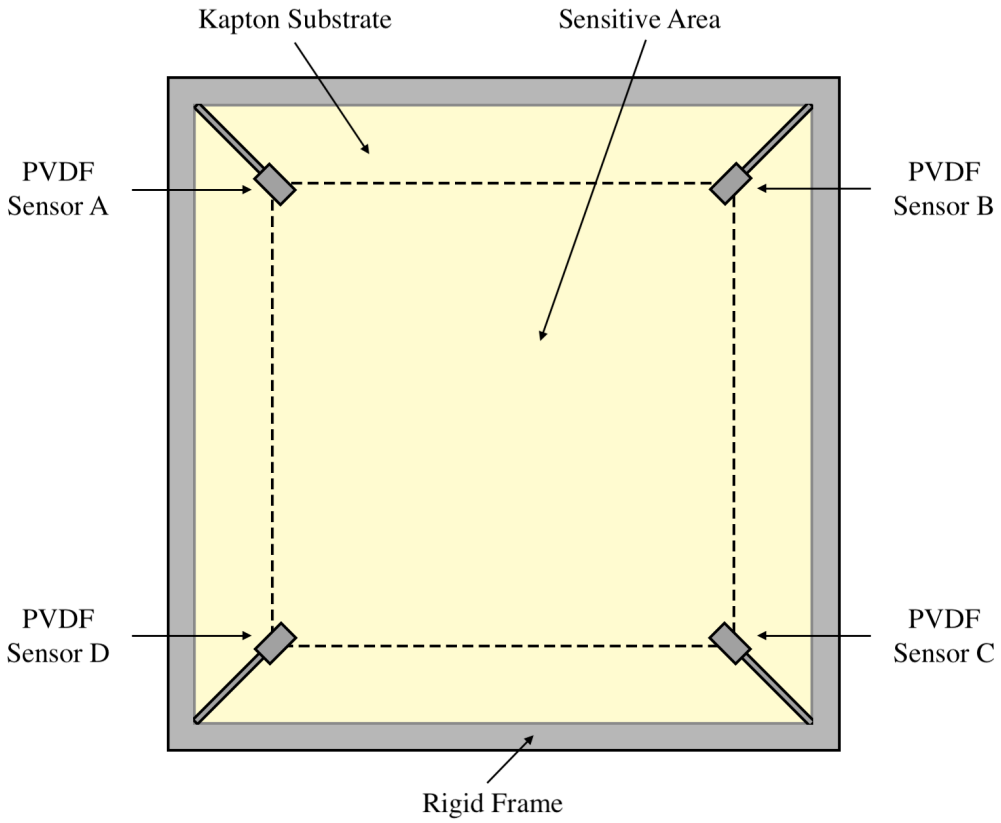

Figure 4.2: The configuration of the primary IDG. The labels represent (1) the aluminium frame, (2) one of the four PVDF sensors and (3) the Kapton film. The dotted line represents the acoustically sensitive region of the Primary IDG.

recorded and analysed by the analytical subsystems on ODIN. Impacts that occur outside this region are also recorded, however, the subsystems would require additional calibration in order to perform their analysis.

The actual length of the standoff between the primary and secondary IDGs is relatively unimportant, however, the separation must be large enough to provide an accurate measurement of the speed and trajectory of OD/ID particles as they perforate the primary and secondary IDGs. It is this perforation that makes it necessary to use such thin substrates on the primary and secondary IDGs, as thicker substrates might disrupt incoming particles and invalidate the data.

Kapton ($C_{22}H_{10}O_5N_2$) is a space-qualified polymer composed of imide monomers, known as polyimide (Inagaki et al., 1989). Imides are a functional group consisting of a single nitrogen (N) bound with two acyl groups and are typically found in high-strength polymers. Polymers mainly consist of carbon-based molecules that are synthesised into long chains, which give them their unique properties, such as high strength, low density, electrical resistance and high melting/boiling points. Kapton remains stable between 4 K and 673 K (DuPont Technical Data Sheet) and has very low outgassing in a vacuum with a total mass loss (TML) of less than 1.0 %, making it an ideal candidate for the primary and secondary IDGs (Willis and Hsieh, 2000). Kapton is also capable of withstanding high-energetic particle radiation environments, such as those found in space (Severin, 2008). Kapton, however, does erode in the presence of atomic oxygen if uncoated or untreated. In order to enable long expossures in space, different types of Kapton (e.g. Al-coated, Au-coated and Black Kapton) have been developed. The Kapton used in the development of the ODIN prototypes was untreated (for cost saving purposes), but would require a thin ($\sim$100 nm) coating for long exposure in space. The strength of Kapton is also desirable, as the IDGs will repeatedly be impacted by OD/ID particles and must not tear. Additionally, Kapton is readily available in films with a thickness ranging between 2.0 µm and 100.0 µm. Finally, prior experimentation conducted at the University of Kent has successfully demonstrated that Kapton has

favourable acoustic properties, permitting the use of PVDF acoustic sensors for impact diagnostics (Corsaro et al., 2016) and is the reason why it was chosen as the substrate material for the primary and secondary IDGs on ODIN.

4.3 The Terminal IDG

The terminal IDG is a syntactic foam block, situated behind the secondary IDG, which is used to capture OD/ID particles and measure their kinetic energy. Four PVDF acoustic impact sensors are orthogonally adhered to the ram surface of the syntactic foam. The PVDF sensors are adhered as close to the corners as possible to maximise the sensitive area of the terminal IDG. This results in a large acoustically sensitive area on the terminal IDG, similar to the primary and secondary IDGs.

Syntactic foam is a class of composite material that is synthesised using pre-formed hollow spheres called cenospheres, or microballoons (see Figure 4.3). The cenospheres can be made from glass, polymer, ceramic or metal and are bound together in a structured matrix with a polymer (Jayavardhan et al., 2017). The syntactic foam used on ODIN is a glass composite, which has the desirable properties of high strength and low density, and is commonly used in subsea buoyancy applications (Shams et al., 2017). It was chosen for the terminal IDG due to its ability to absorb projectiles with minimal local disruption and impact ejecta.

The syntactic foam used on ODIN is Bathypelagic Zone (BZ) syntactic foam (BZ-24) and is supplied by Engineered Syntactic Systems. BZ grade foams are composed of a variety of hollow glass spheres and have the lowest density in the industry (as stated by Engineered Syntactic Systems), with a density of 0.39 ± 0.03 g cm^{-3} and a compressive strength and compressive modulus of 24.1 MPa and 1.12 MPa, respectively. Syntactic foam was chosen for the terminal IDG after extensive studies involving a number of different materials. Details of the material selection process and the results are discussed in Section 5.3.1.

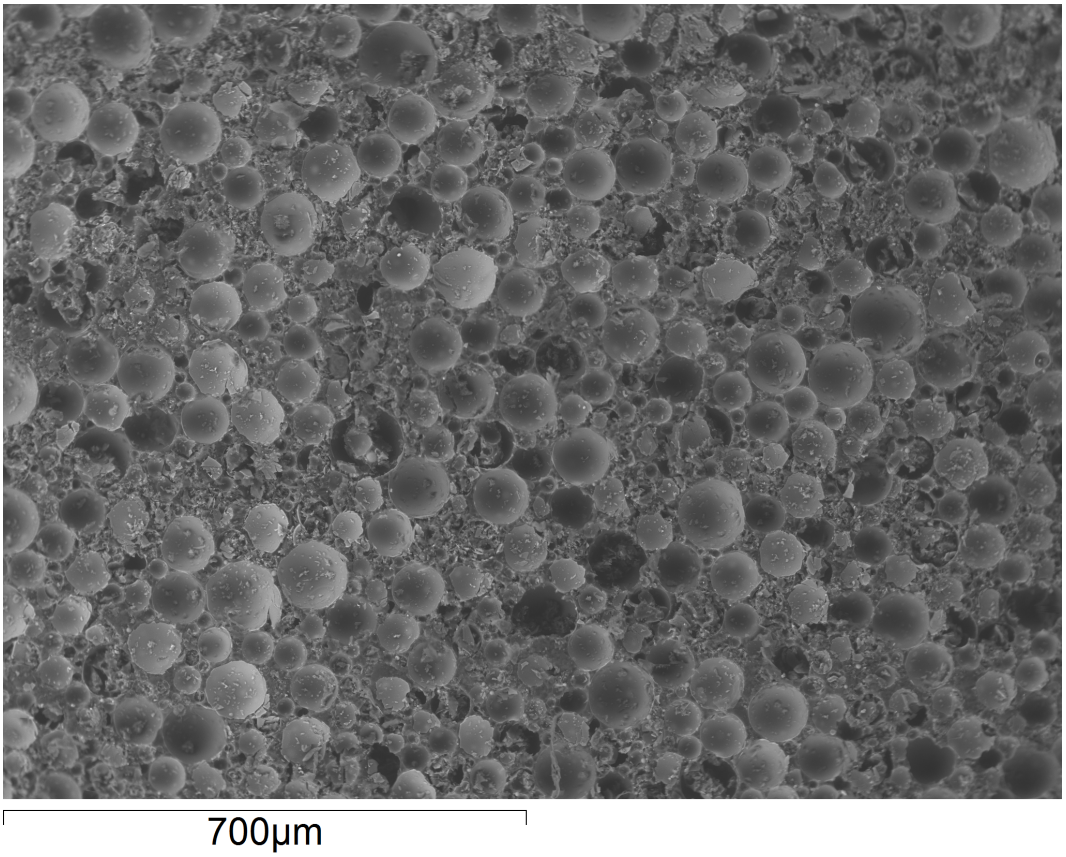

Figure 4.3: Backscatter electron image of the BZ-24 syntactic foam used on the terminal IDG.

Figure 4.3 is a backscatter electron image of the BZ-24 syntactic foam used for the terminal IDG showing the micrometer sized cenospheres embedded in the polymer.

4.4 Polyvinylidene Fluoride (PVDF) Acoustic Sensors

The primary requirements for the sensors used on ODIN are to: (1) be capable of real-time operation, (2) have a large area sensitivity to a wide range of impactor masses and diameters, (3) be excellent at locating impacts, (4) have long life capability, (5) have simple operation and (6) be cost effective. Furthermore, they must be space-qualified, or meet the criteria for space qualification.

The PVDF sensors used on ODIN are commercially available from Variohm-EuroSensor Ltd. and are constructed by placing a thin strip of polarised piezoelectric polymer between two electrodes. The bulk polymer has a volume polarisation that induces an electric charge in response to strain on the material (Simpson and Tuzzolino, 1985). This property is advantageous as the sensors are not reliant on a power source and can therefore remain continuously active. This means they satisfy the real-time operation, long-life capability and low cost requirements of ODIN. The four PVDF sensors also provide data that enable the location of impacts to be calculated accurately. If one sensor is damaged and fails, impact locations can still be calculated (with reduced accuracy) by switching from an algorithmic to an alebraic method. Additionally, intelligent PVDF sensor positioning can produce large area sensitivity to impactors with a wide range of masses and diameters, which satisfy the remaining analytical requirements of ODIN.

PVDF sensors have been used in OD/ID detectors for many years, and have an excellent pedigree as space-worthy detectors. Some examples include:

1. The Dust Counter and Mass Analyser (DUCMA) onboard the Vega spacecraft, which measured the mass and flux of dust particles originating in the nucleus of Halley's comet (Simpson et al., 1986).

2. The Dust Flux Monitor Instrument (DFMI) onboard the Stardust spacecraft, which measured the particle flux, intensity profile and mass distribution during passage through the coma of comet Wild 2 (Tuzzolino et al., 2003).

3. The High Rate Detector (HRD) onboard the Cassini spacecraft, which used two separate PVDF sensors to detect the particle flux and mass distribution throughout the Saturnian ring system (Srama et al., 2004).

4. The Space Dust (SPADUST) instrument onboard the Earth orbiting Advanced Research and Global Observation Satellite (ARGOS) measured dust trajectory and time-of-flight between two planar arrays (Tuzzolino et al., 2005).

5. The Venetia Burney Student Dust Counter (SDC) onboard the New Horizons spacecraft mapped the spatial and size distribution of dust during its long trip to Pluto and beyond (Horanyi et al., 2009).

6. The Cosmic Dust Experiment (CDE) onboard the Earth orbiting Aeronomy of Ice in the Mesosphere (AIM) satellite measured variability of cosmic dust (Poppe et al., 2011).

7. The Arrayed Large-Area Dust Detectors in INterplanetary space (ALADDIN) onboard the Interplanetary Kite-craft Accelerated by Radiation Of the Sun (IKAROS) measured the number density of dust in the Zodiacal cloud (Hirai et al., 2014).

8. The Space Dust Sensor (SDS) onboard the ISS combines several technologies to characterize the size, speed, direction, and density of OD/ID ranging from 50 µm to 500 µm in size (Hamilton et al., 2017).

The way in which the PVDF sensors are used on ODIN are similar to those on the SDS and represent a significant improvement in analytical measurements, relative to previous models, due to their placement and capacity to detect a range of particle characteristics as described below. For this reason, many of the advancements made during this research are directly compared with the SDS.

4.4.1 PVDF Sensor Characteristics

For applications on thin, low-modulus, substrates like the Kapton deployed on the primary and secondary IDG, it is important that the sensors do not significantly constrain the motion of the substrates, as this would degrade sensitivity. The PVDF sensors are flat and have an active thickness of 28 µm. The active area is 12 mm by 15 mm and is composed of overlapping silver ink screen-printed electrodes. Their capacitance is 1.37 nF and they have a nominal response of $0.012\,\mathrm{V}\,\mu\epsilon^{-1}$ (volts per microstrain). The sensors have 20 cm lead–ins with male connector pins at the end, which can be in-

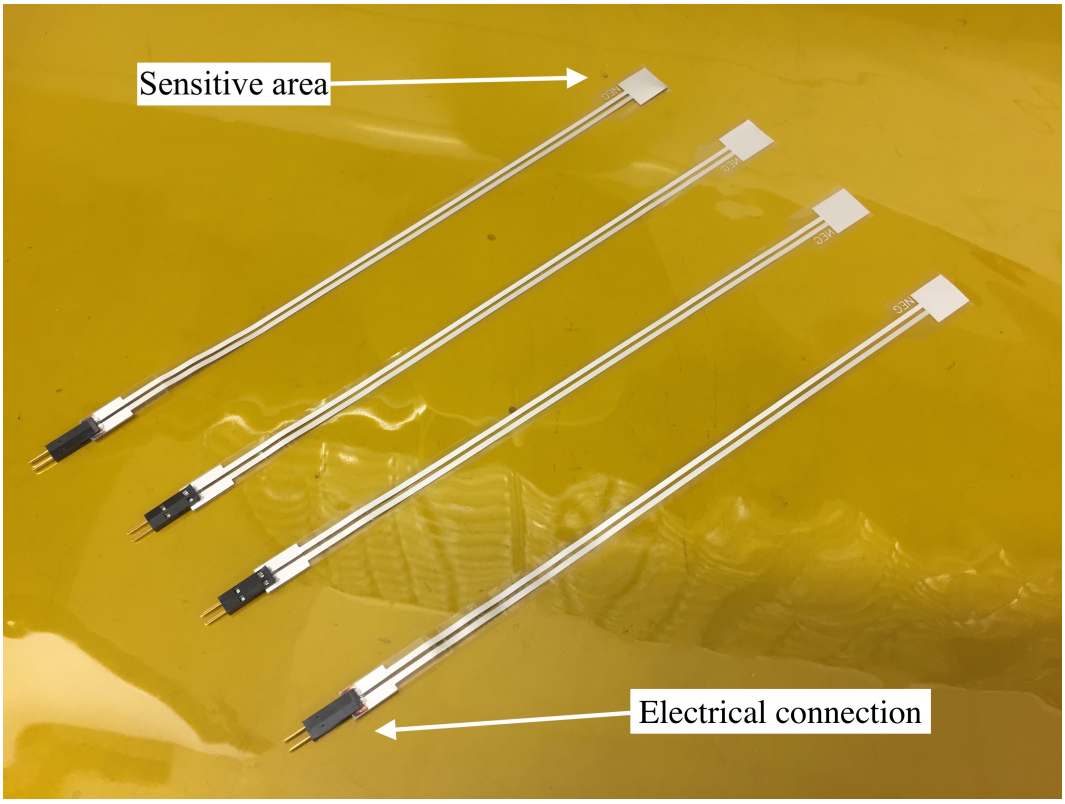

Figure 4.4: Photograph of four PVDF sensors used on a prototype of ODIN.

serted into a socket (Figure 4.4). The sensors have an operational temperature range of −200 °C to 50 °C for use in the laboratory. For use in space, tailored sensors are required with a wider temperature range of −200 °C to 115 °C.

4.4.2 Adhesion and Location Assignment

The actual location of the sensors on each IDG is not critical. However, it is important that their locations are known to a high degree of accuracy. Ideally the sensors are positioned in locations that maximise the path length from any impact location. It is therefore logical to place the sensors as close to the corners of the support frame as possible. The sensors, however, must be positioned far enough from the frame to give good temporal separation between the acoustic signals of interest and any edge reflections. Due to the possible compression of the Kapton film, the reflected waves

could be travelling approximately 20 % faster than the initial wave. Typically, the first few acoustic waves of interest arrive within a 50 µs period. To prevent interference, it was decided that a 75 µs interval between the arrival time of the initial and reflected waves would be sufficient. Assuming an initial sound speed of $1.59\,\mathrm{mm\,\mu s^{-1}}$ and a reflected sound speed of $1.91\,\mathrm{mm\,\mu s^{-1}}$, a distance of 64 mm was calculated. to provide an acceptable distance between the sensors and the frame. Hence, the centre of the active region of each sensor was positioned ~ 64 mm from the edge of the frame.

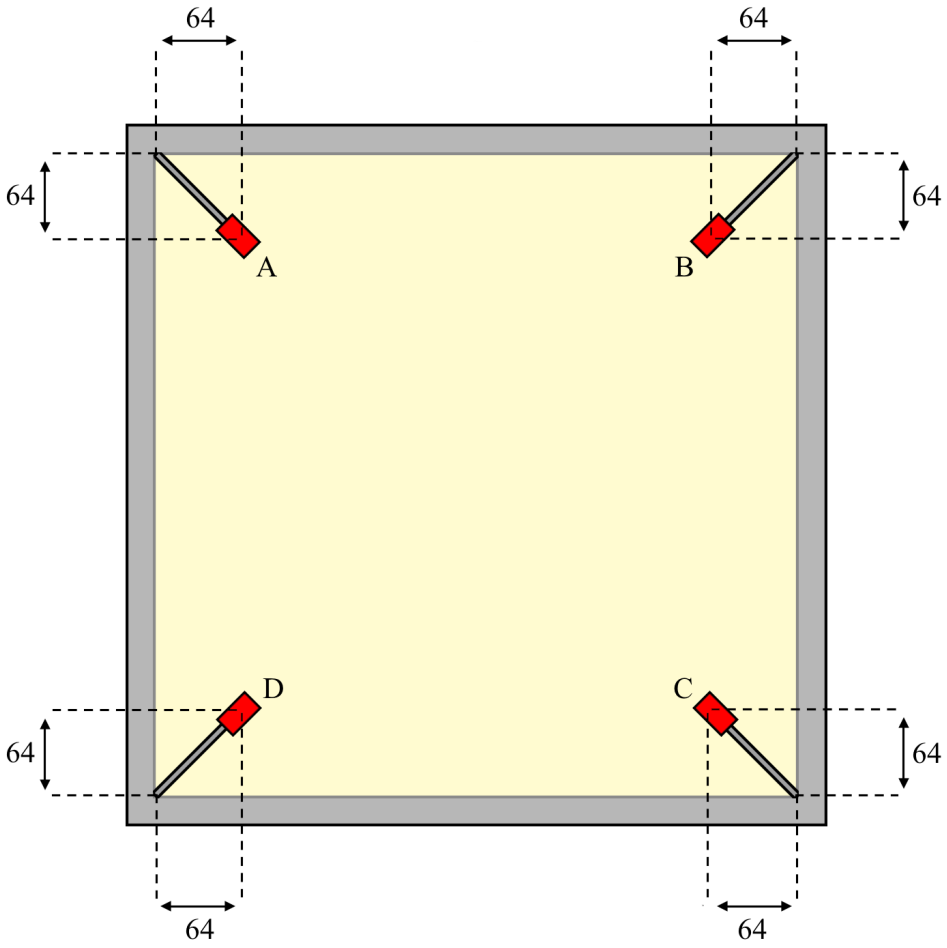

Figure 4.5: Schematic of the PVDF sensor placement on the primary IDG. The sensitive regions of the PVDF sensors are highlighted by the red rectangles. All dimensions are in millimeters (mm).

Based on previous experience, the sensors are most sensitive to strain in their length direction, with only 10 % of the sensitivity in the perpendicular direction. To take advantage of their lengthways sensitivity, the sensors are positioned 45° from the edge of the frame. Figure 4.5 shows a schematic of the PVDF sensor locations.

The position of the PVDF sensors on the terminal IDG is similar to those on the primary and secondary IDGs. The only difference is that the sensors are adhered to the ram side of the terminal IDG, in contrast to the aft side on the primary and secondary IDGs.

The adhesive used to attach the sensors to each IDG is GC 10-128 Super Adhesive. It was selected because it is an ethyl cyanoacrylic adhesive with high cure strength (5000 psi); it is solvent-free, with negligible shrinkage during curing; it has low viscosity (30 cps), allowing thin bonds; it cures in less than a minute; and its bond strength holds up to 160 °C. For use in space, Variohm-EuroSensor Ltd. provide PVDF sensors with self adhesive surfaces qualified for use in space. The Kapton used on the primary and secondary IDG is smooth enough that the PVDF sensors can be adhered directly onto the surface. The syntactic foam used in the terminal IDG has a rough face which prevents the sensors being adhered directly to the material. Hence, a thin layer of araldite was applied to the foam to create a smooth surface to which the PVDF sensors can be adhered. The araldite was chosen to prevent any acoustic impedance miss-match between the PVDF sensors and the rough surface of the syntactic foam. Space qualified araldite would be required for use in space, which is available from specific suppliers (e.g. Master Bond). Alternatively, the araldite used on ODIN could be tested for space qualification.

4.4.3 PVDF Data

PVDF sensors induce an electric charge in response to strain caused by acoustic shock-waves in the material. The charge can be recorded as a voltage by an acquisition board

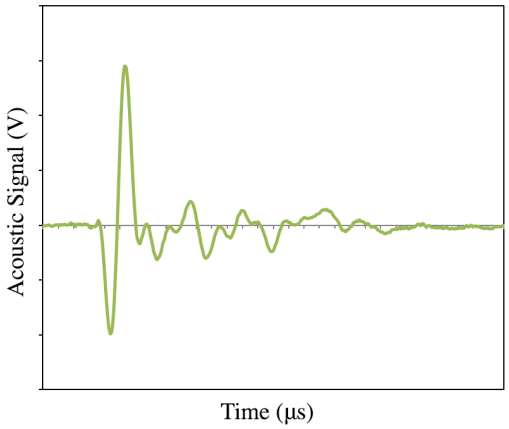

Figure 4.6: Typical PVDF signal on a Kapton substrate.

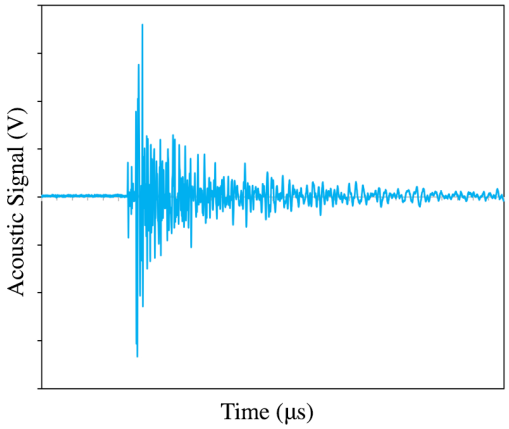

Figure 4.7: Typical PVDF signal on the syntactic foam

and computer. The data acquisition hardware in this research had a sample rate of one sample per microsecond. Hence, the voltage was recorded each microsecond from each of the PVDF sensors and can be visualised by plotting voltage (V) against time (µs).

Figures 4.6 and 4.7 are examples of a typical signal that was recorded by a PVDF sensor adhered to the Kapton substrate and syntactic foam respectively. Although slightly different, the shape of both signals is representative of a damped sine wave. Equation 4.1 is a simplified version of the general equation for an exponentially damped sinusoid, where $y(t)$ is the instantaneous amplitude at time t, A_0 is the initital amplitude, λ is the decay constant, ω is the angular frequency and ϕ is the phase angle at some arbitrary point.

$$y(t) = A_0 \cdot e^{-\lambda t} \cdot (cos(\omega t + \phi)) \tag{4.1}$$

During the course of this research attempts were made to utilise the amplitude (for diameter and kinetic energy measurements), frequency (for kinetic energy measurements), temporal phase shift (for impact locations and time of flight calculations) and decay constant to determine physical characteristics of projectiles impacting the Kapton substrates and syntactic foam. Section 10.7.4 details an attempt at Fourier analysis of the signals.

4.5 Subsystem Overview

All the diagnostic subsystems on ODIN use the PVDF sensors discussed in Section 4.4 to analyse the characteristics of OD/ID. The primary motivation for OD/ID analysis is to improve the accuracy of environment models so that protection systems, such as Whipple shields, can be applied to spacecraft more efficiently. Ballistic limit equations are used to calculate the performance of such shields and relate critical particle diameters with impact velocities, as well as other parameters such as impact angle and particle density (Christiansen and Kerr, 1993). Hence it is important to understand the velocity, size, impact angle and density of OD/ID to a high degree of accuracy. Hence, ODIN has five analytical subsystems, which include the following:

1. Impact Cartesian Coordinate (ICC) Subsystem

The ICC subsystem is responsible for counting the number of OD/ID particles that interact with ODIN, and measures the impact coordinates. It uses temporal phase shifts in the acoustic signals recorded by the PVDF sensors on the primary IDG and secondary IDG to determine the impact coordinates, and is the most important subsystem on ODIN. This is because accurate coordinates of impacts on the primary and secondary IDGs are required to perform the calculations in the other analytical subsystems.

2. Unit Vector Trajectory (UVT) Subsystem

The UVT subsystem is responsible for measuring the trajectory of OD/ID particles. It does this using the coordinates measured by the ICC and applying three-dimensional Pythagoras theorem. With regard to scientific interest, the trajectory of the particles can be used to investigate the origin of OD/ID, as discussed in Chapter 2. With regard to spacecraft operation, knowledge and an understanding of OD/ID trajectories may be used to avoid collisions by tailoring the orbit of spacecraft. Furthermore, knowledge of OD/ID trajectories can improve the efficiency of ballistic limit equations, as impact damage is a function of impact angle, which in turn, improves shielding capabilities.

3. Impact Gate Velocity (IGV) Subsystem

The IGV subsystem is responsible for measuring the speed of OD/ID as it passes through ODIN, using the known distance between the primary and secondary IDG, in conjunction with the impact time on each IDG. With regard to spacecraft operations, it is important to know the velocity range of OD/ID, so that efficient impact mitigation systems can be deployed on spacecraft. The velocity of a particle can also be used to differentiate between OD (lower speed) and ID (higher speed), such as micrometeoroids.

4. Peak-Trough Diameter (PTD) Subsystem

The PTD subsystem is responsible for measuring the size of OD/ID that interacts with ODIN, using the amplitude of acoustic signals recorded by the sensors on the primary IDG. It is also important to know the size of OD/ID so that efficient impact mitigation systems can be deployed on spacecraft. Additionally, knowledge of the size of OD/ID is required to update environment models, such as MASTER.

5. Peak-Trough Energy (PTE) Subsystem

The PTE subsystem is responsible for measuring the kinetic energy of OD/ID that interacts with ODIN. It uses the amplitude of acoustic signals recorded by the sensors on the terminal IDG to measure the kinetic energy. Kinetic energy measurements are important as they can be used in conjunction with the velocity to approximate the mass of OD/ID.

Mass, Momentum and Density Approximations

In addition to the analysis of OD/ID particles conducted directly by the analytical subsystems onboard ODIN, the mass, momentum and density of particles can be approximated. Certain assumptions, however, must be made to calculate the density of particles.

The velocity and kinetic energy of OD/ID particles that are recorded by the IGV and PTE respectively, can be used to calculate the mass, m (kg).

$$m = \frac{2E}{v^2} \tag{4.2}$$

Where E (J) is the kinetic energy and v ($\mathrm{m\,s^{-1}}$) is the velocity of particles passing through ODIN. The momentum, p ($\mathrm{kg\,m\,s^{-1}}$) of particles is simply calculated using the velocity, v ($\mathrm{km\,s^{-1}}$) and the mass, m (kg).

$$p = m\ v \tag{4.3}$$

The density, ρ ($\mathrm{kg\,m^{-3}}$) of particles is approximated using the mass and volume of particles passing through the detector. It is not possible to determine the shape of particles passing through the detector, hence, a spherical shape is assumed for these calculations, where the radius, r (mm), is calculated by the PTD subsystem.

$$\rho = \frac{3m}{4\pi r^3} \tag{4.4}$$

Where m (kg) is the mass and r (m) is the radius of particless passing through the detector.

4.5.1 Subsystem Schematic

As previously mentioned, all the subsystems use acoustic signals to investigate the properties of OD/ID. The acoustic signals are recorded by PVDF sensors positioned across three IDGs. Figure 4.8 is a subsystem schematic of ODIN, showing which IDG provides data to which subsystem.

Experiments were carried out to test the performance of all the subsystems on ODIN. Details of the experiments and their results are discussed in Chapters 6 – 10.

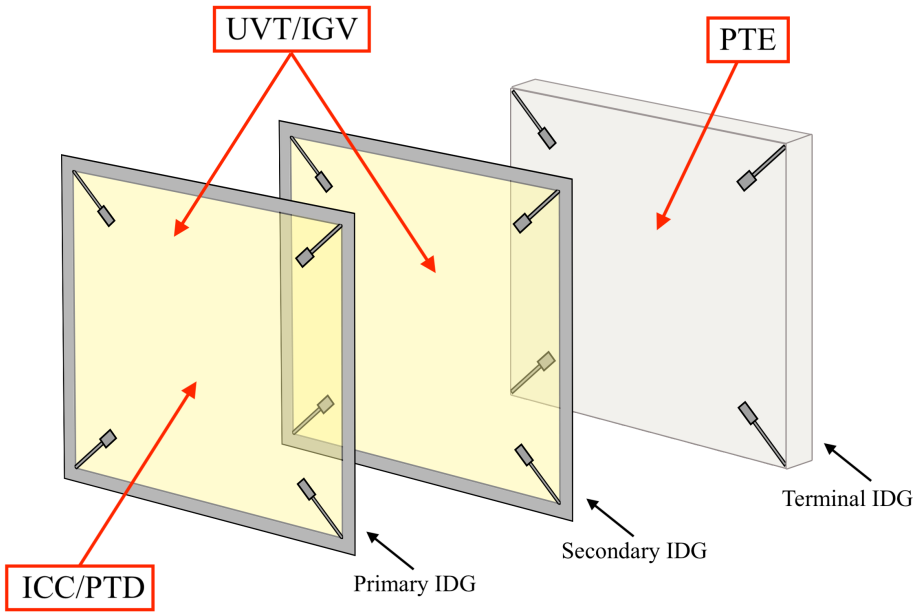

Figure 4.8: Subsystem schematic of ODIN, showing which IDG provides data to each subsystem.

4.6 Conceptual In-flight Data Analysis Protocol

The raw data collected by the twelve PVDF sensors across the three IDGs is approximately 1 MB per impact. In normal operation an instrument such as ODIN would have to store data for up to 24 hours before transmission to Earth. In a period of high flux this could lead to excessive data storage and transmission requirements. Therefore, it is conceived that ODIN will process raw data in real time and generate data products for transmission to Earth, thereby reducing the data overhead per impact.

Figure 4.9 is a schematic of the possible overall data processing and data polling to Earth requirements of ODIN. The processing system is where the raw data are analysed by the software algorithms and is performed onboard ODIN by a low power processor (i.e. Rasberry Pi). These data are then packaged and sent to the ISS for subsequent routine retransmission to Earth.

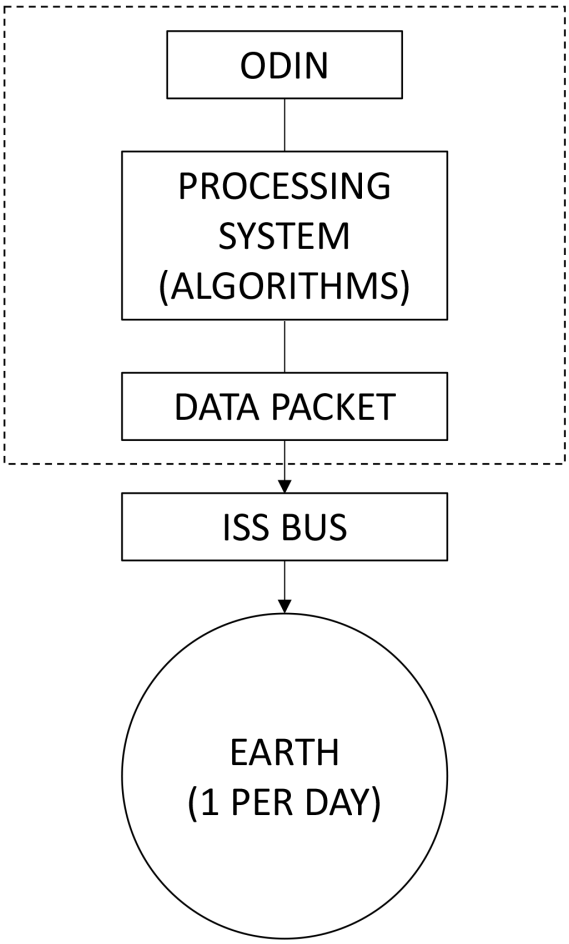

Figure 4.9: Schematic of data processing and data polling to Earth.

Figure 4.10 is a breakdown of the data-packet structure. It is envisaged that the number of impacts in a 24 hour period will not exceed 65535 (2 bytes). For each possible impact, ODIN records the location, trajectory, velocity, diameter and kinetic energy, even if the majority of the records are zero. The data for a maximum of 65535 impacts can be distilled into a data-packet of approximately 1 MB. This is a realistic data transmission rate expected on an in-flight instrument such as ODIN.

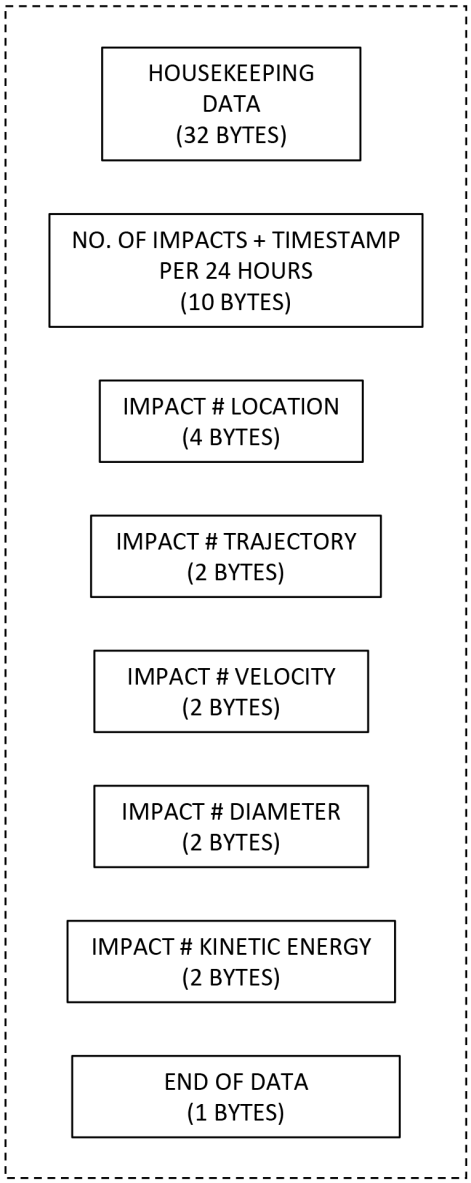

Figure 4.10: Conceptual in-flight data packet structure showing number of bytes per impact.

Chapter 5

ODIN Prototypes

The initial prototypes of ODIN were built to determine the optimum dimensions of the primary and secondary IDGs and select the material for the support frame, as well as testing the diagnostic subsystems (described in detail in Chapters 6 – 9). This was followed by a terminal IDG prototype and experimental analysis of possible terminal materials, as well as testing the kinetic energy subsystem (described in detail in Chapter 10). Finally, prototypes with full IDG configurations were built so that all of the analytical subsystems could be tested simultaneously.

In this Chapter the various incarnations of ODIN are described, with a discussion on the problems discovered with each prototype and how the lessons learnt through experimentation fed into the refinement of the design and construction of the next prototype. Table 5.1 shows the evolution of the ODIN prototypes.

5.1 Prototype: ODIN-Alpha

The first prototype, ODIN-Alpha, was a minature version of just the primary IDG. It had an acrylic frame with outer dimensions of 341 mm × 341 mm and inner dimensions of 280 mm × 280 mm. A Kapton substrate, 25 µm thick, was mounted parallel to the

Table 5.1: Evolution of the ODIN prototypes showing the IDGs, number of sensors, frame material and detection area.

Prototype	Configuration	No. of Sensors	Frame Material	Detection Area (m^2)
ODIN-Alpha	Primary IDG	3	Plastic	~ 0.02
ODIN-Beta	Primary IDG	4	Aluminium	~ 0.15
ODIN-SF	Terminal IDG	4	N/A	~ 0.03
ODIN-2	Primary IDG	4	Plastic	~ 0.15
	Secondary IDG	4	Plastic	~ 0.15
	Terminal IDG	4	N/A	~ 0.03
ODIN-3	Primary IDG	4	Aluminium	~ 0.15
	Secondary IDG	4	Aluminium	~ 0.15
	Terminal IDG	4	N/A	~ 0.03

acrylic frame and secured with adhesive tape. Three PVDF sensors were orthogonally adhered to the aft surface of the Kapton film. Three sensors were used so that the locations of impacts could be calculated algebraically. The sensors were positioned 64 mm from the edge of the frame, providing a large enough distance to prevent reflected waves from interfering with the useful acoustic signals, as explained in Section 4.4.2. and 152 mm apart from each other, creating a $23.1 \times 10^3\,mm^2$ sensitive region. A schematic and photograph of ODIN-Alpha showing the position of each PVDF sensor can be seen in Figures 5.1 and 5.2, respectively.

ODIN-Alpha was discontinued as a result of the poor acoustic data due to interference from gas blasts. Gas blasts are a common occurrence during LGG experiments and are caused by gas, originating in the blast tank, entering the impact chamber immediately before the projectile. During the ODIN-Alpha experiments, the gas blast was large enough to trigger all of the PVDF sensors simultaneously. Consequently, they were recording gas blast signals with a wide range of frequencies and large amplitudes immediately before the impact. These additional acoustic signals interferred with and swamped the signals of interest created by the projectile impact.

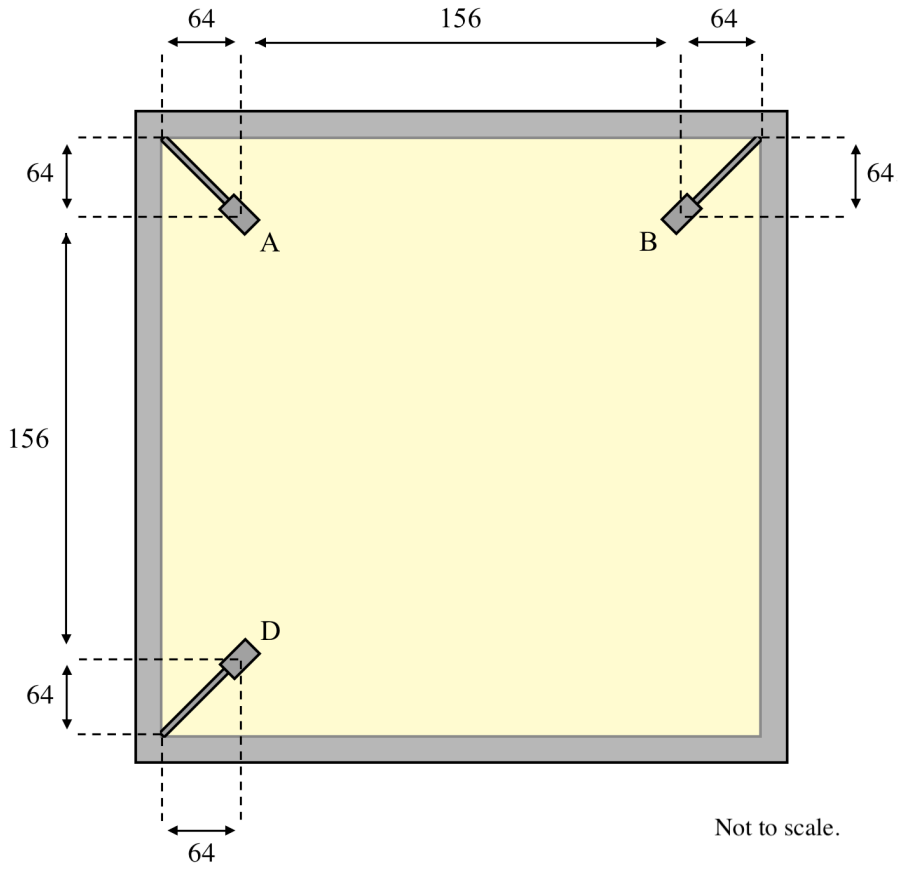

Figure 5.1: A schematic of the ODIN-Alpha prototype showing the three PVDF sensors, A, B and D, adhered to the top left, top right and bottom left corners of the Kapton substrate, respectively. All dimensions are in millimeters (mm).

Figure 5.3 and Figure 5.4 are two examples of acoustic data recorded during impacts between ODIN-Alpha and spherical stainless steel projectiles with a diameter of 2.0 mm and impact velocities of $\sim$5.0 km s^{-1}. Figure 5.3 is a representation of desirable acoustic data, where there are no contaminations in the signals. The signals caused by the gas blast, enclosed within the dotted grey box, do not interfere with the signals created by the projectile impact, highlighted with grey arrows. Figure 5.4 is a representation of undesirable acoustic data. In this example, the signals caused by the gas blast, again enclosed within the dotted grey box, do interfere with the signals created by the projectile impact, highlighted with grey arrows. This interference prevents ODIN's analytical subsystems from attaining meaningful results. The majority of data obtained by ODIN-Alpha had gas blast interference.

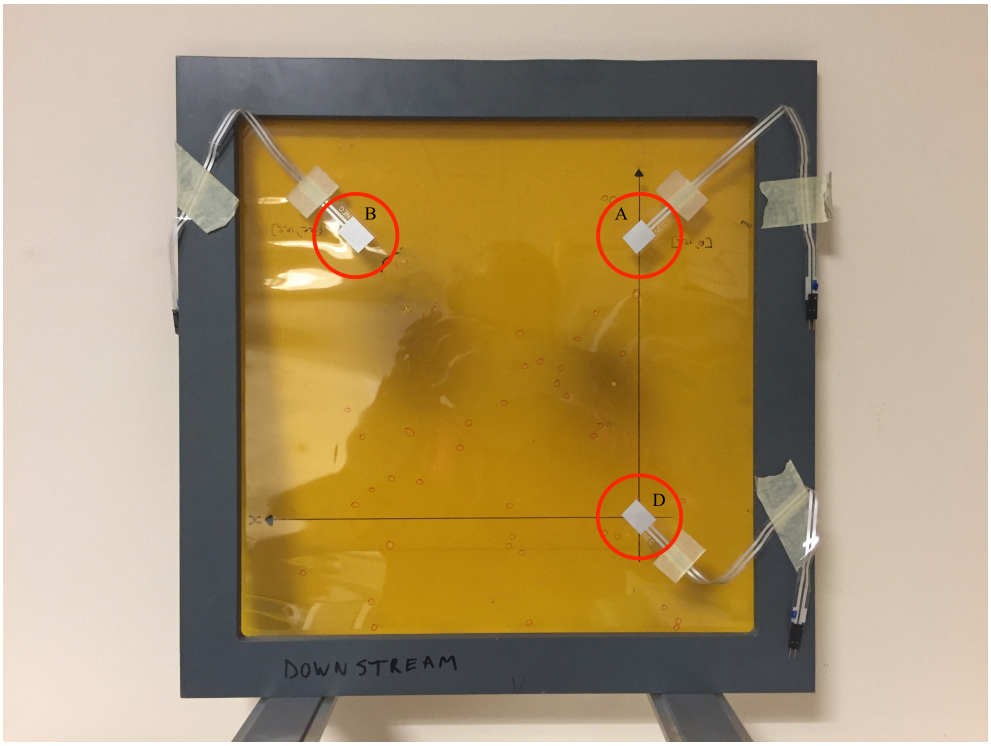

Figure 5.2: A photograph of the aft-side of ODIN-Alpha showing the three PVDF sensors, circled in red.

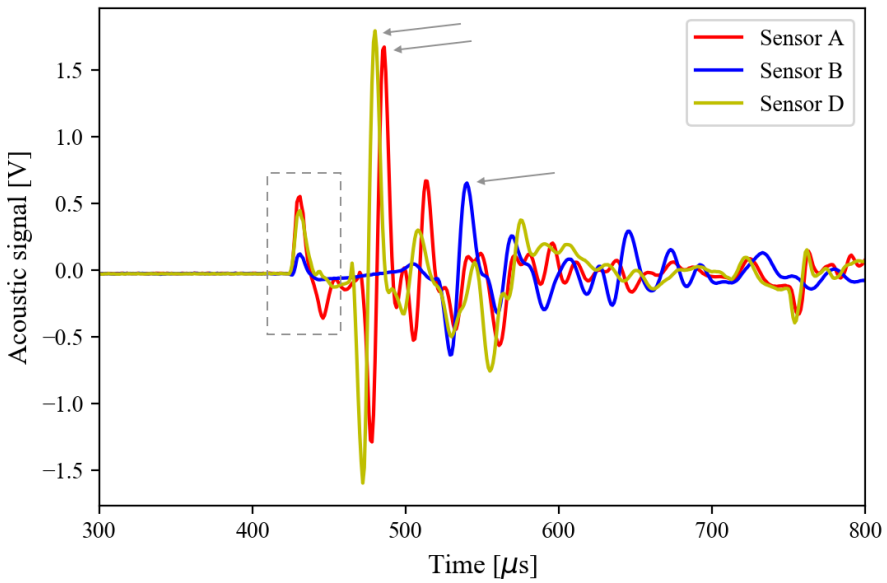

Figure 5.3: Clean acoustic signal recorded by the ODIN-Alpha prototype. The grey box shows the gas blast signal. The arrows point to the signals created by the impact.

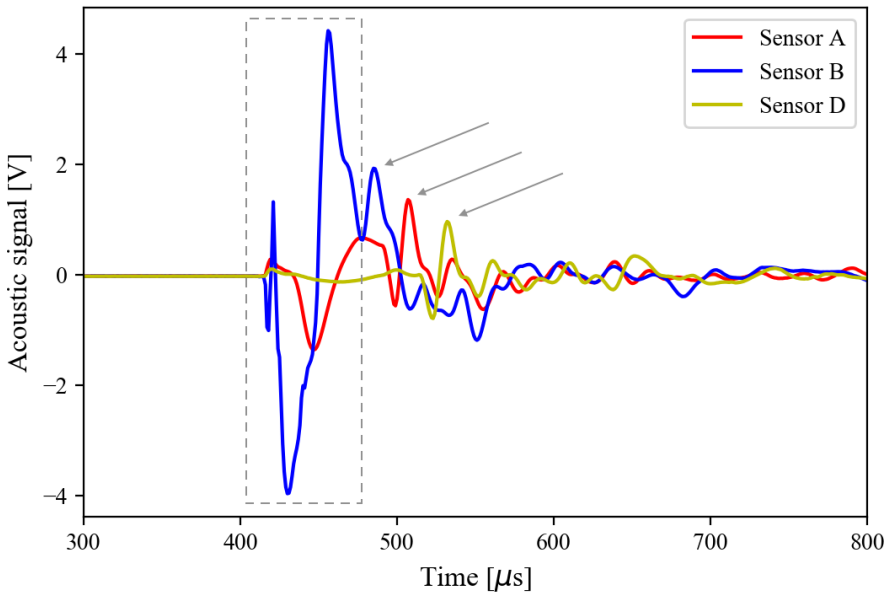

Figure 5.4: Contaminated acoustic signal recorded by the ODIN-Alpha prototype. The grey box shows the gas blast signal. The arrows point to the signals created by the impact.

5.2 Prototype: ODIN-Beta

The second prototype, ODIN-Beta, was a full size version of the primary IDG. It had an aluminium frame with outer dimensions of 565 mm × 565 mm and inner dimensions of 515 mm × 515 mm. A Kapton substrate, 25 µm thick, was mounted parallel to the aluminium frame and secured with adhesive tape that folded over the frame. Four PVDF sensors were orthogonally adhered to the aft surface of the Kapton substrate. The upgrade from a three-sensor system to a four-sensor system was implemented to allow algorithmic impact location calculations (explained in Chapter 6). The sensors were positioned 64 mm from the edge of the frame and 387 mm apart from each other, creating a $\sim 150.0 \times 10^3\,\mathrm{mm}^2$ sensitive region. A schematic and photograph of ODIN-Beta showing the position of each PVDF sensor can be seen in Figures 5.5 and 5.6, respectively.

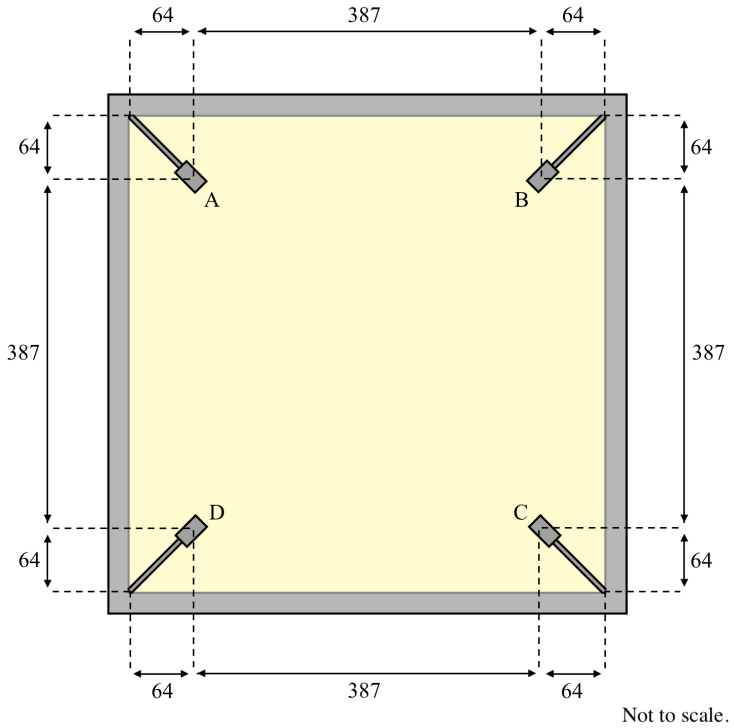

Figure 5.5: A schematic of ODIN-Beta showing the four PVDF sensors, A, B, C and D, adhered to the top left, top right, bottom right and bottom left corners of the kapton substrate, respectively. All dimensions are in millimeters (mm).

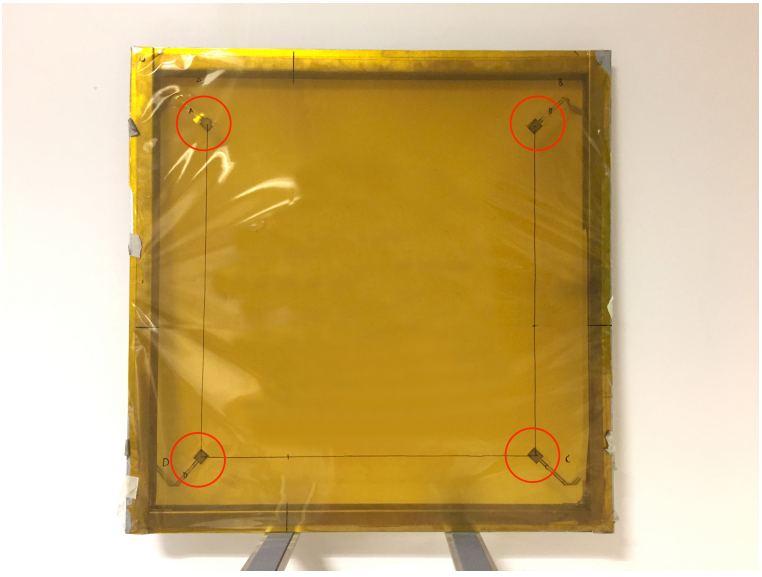

Figure 5.6: Photograph of ODIN-Beta showing the four PVDF sensors, circled in red.

The enlarged area of ODIN-Beta successfully increased the temporal separation between the gas blast signals and the impact signals of interest, thus removing the contaminating signal. The ODIN-Beta prototype was used in a series of successful experiments, specifically, the Impact Cartesian Coordinate (ICC) and Peak-Trough Diameter (PTD) subsystem proof-of-concept experiments, which are discussed in Chapters 6 and 9, respectively. ODIN-Beta was eventually discontinued so that a more advanced prototype, capable of testing different subsystems, could be developed and trialled.

5.3 Prototype: ODIN-SF

The third prototype, ODIN-SF, was a miniature version of the terminal IDG. It consisted of a 310 × 310 × 71 mm syntactic foam block with four PVDF sensors orthogonally adhered to its forward facing surface. The sensors were positioned 64 mm from the edge of the syntactic foam block and 182 mm apart from each other, creating a $\sim 33.1 \times 10^3\,\mathrm{mm}^2$ sensitive region. A schematic and photograph of ODIN-SF showing the position of each PVDF sensor can be seen in Figures 5.7 and 5.8 respectively.

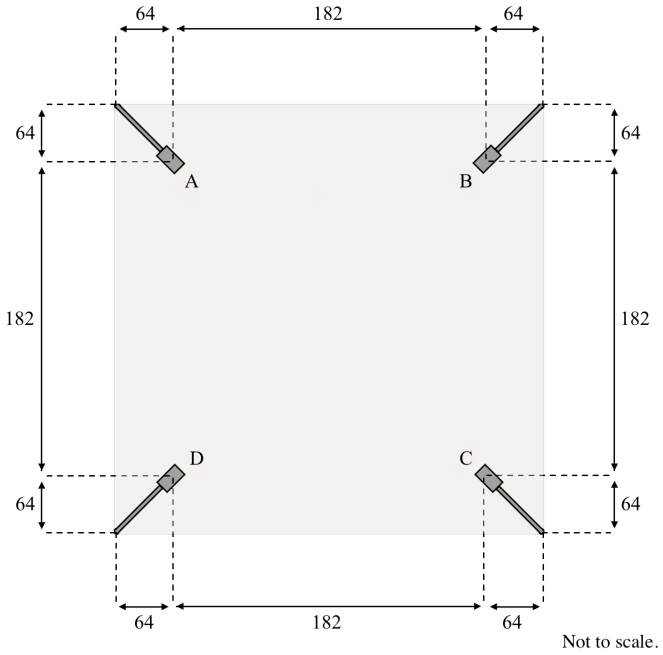

Figure 5.7: A schematic of ODIN-SF showing the four PVDF sensors, A, B, C and D, adhered to the top left, top right, bottom right and bottom left corners of the syntactic foam block, respectively. All dimensions are in millimeters (mm).

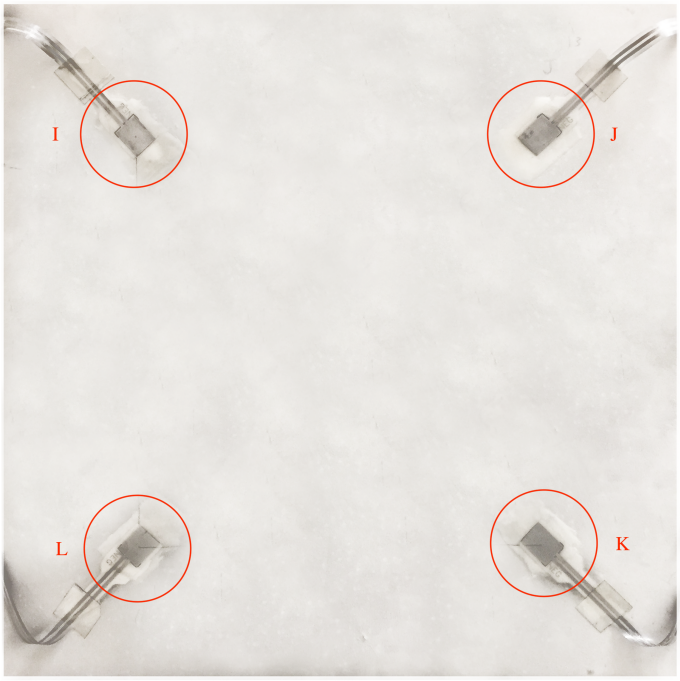

Figure 5.8: A photograph of the front side of ODIN-SF showing the four PVDF sensors, circled in red.

ODIN-SF was used in a series of successful experiments, specifically, the Peak-Trough Energy (PTE) subsystem proof-of-concept experiments, which are discussed in Chapter 10. ODIN-SF was eventually discontinued so that a full prototype, capable of testing all of the subsystems simultaneously, could be developed.

5.3.1 Terminal IDG Material Selection Experiments

Prior to the decision to use syntactic foam as the terminal IDG, reserch was necessary to determine which material would be best for the capture surface on the terminal IDG (a vital component of the final ODIN configuration) and thus a suite of experiments were carried out on a set of different materials to determine their resistance to impact disruption and fragmentation. Descriptions and results of that shot programme are detailed here.

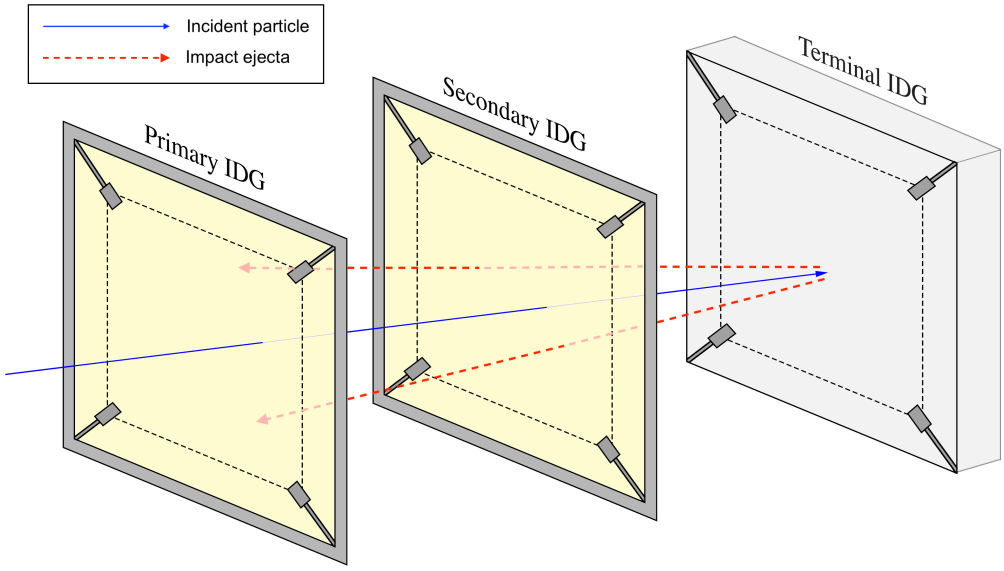

Figure 5.9: Schematic of impact ejecta travelling through the primary and secondary IDG in the opposite direction to incident particles.

The main criteria for the selected terminal IDG material was that it had to: (1) absorb incoming OD/ID particles travelling at hypervelocity with minimal local disruption and, (2) minimise ejecta caused during the impacts. Reducing energy loss caused by local disruption and the generation of ejecta increases the accuracy of the kinetic energy measurements, which is the main goal of the terminal IDG. Furthermore, acoustic data can be misleading if ejecta created during terminal IDG impacts come into contact with, or penetrate, the primary or secondary IDG in the reverse direction, see Figure 5.9.

Nine experiments were conducted using the LGG facility at the University of Kent to determine the most suitable material for the terminal IDG. The materials included in the study were: acetal, aluminium, high-density polyurethane, nylon, polycarbonate, polytetrafluoroethylene (PTFE), polyvinyl chloride (PVC), silicone elastomer and syntactic foam. These materials were readily available in the laboratory and selected due to their wide range in physical properties. During each experiment, a different material was placed into the target chamber of the LGG, where it was impacted by a spherical, stainless steel projectile with a 1.0 mm diameter, travelling at a velocity of

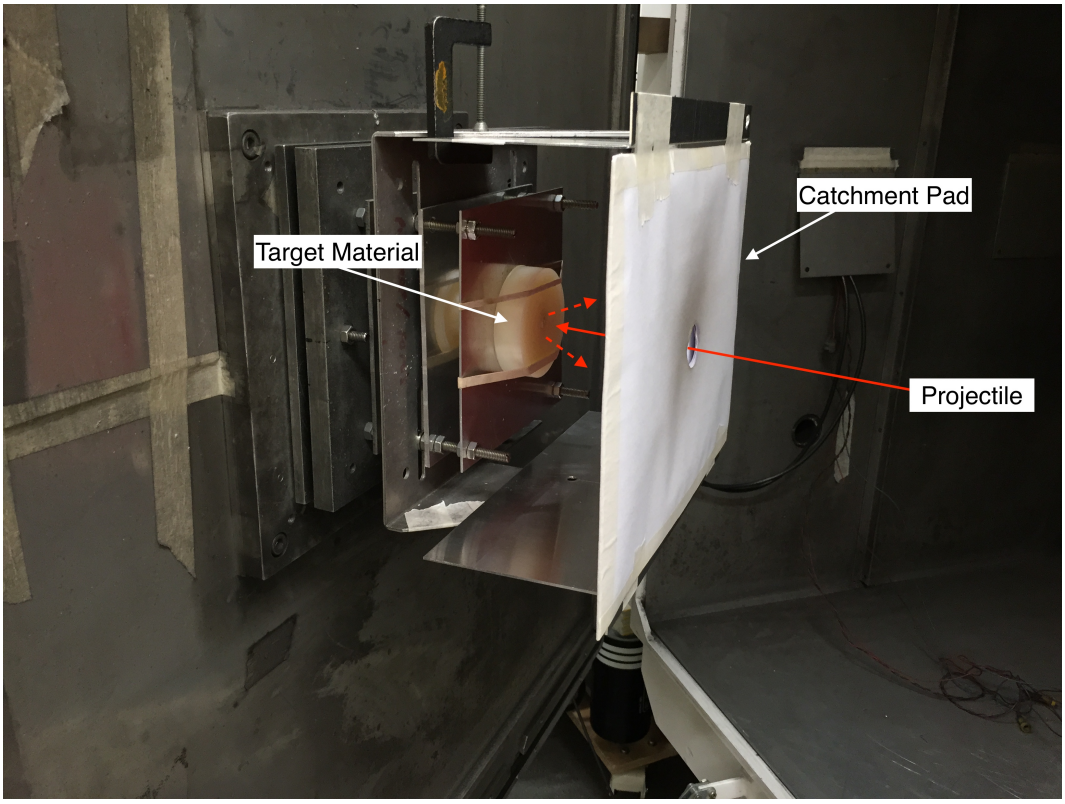

Figure 5.10: Photograph of the IDG material selection experimental setup with annotations. The red arrow represents the path of a projectile passing through the catchment pad hole and impacting the target material. The ejecta area is represented by the red dotted lines.

$\sim$5.0 km s^{-1}. The impact craters and ejecta produced during each impact were analysed to determine which material was most suitable for the terminal IDG.

A catchment pad, consisting of 16 sheets of paper with a central, 25 mm diameter, hole was used to collect and analyse ejecta. The incident projectiles passed through the hole, unaffected, before impacting the target material. Ejecta from the subsequent impact, traveling in the opposite direction to the incident projectiles, embedded itself within the aft facing side of the catchment pad. The catchment pad was positioned 90 mm in front of the target (Figure 5.10). Local disruption was quantitatively analysed by measuring the crater diameter, number of fractures and length of fractures in the target material (Table 5.2). The size of individual ejecta was quantitatively analysed by measuring the cross section of individual ejecta (Table 5.3). The penetration potential

was assessed by counting the number of penetrated sheets in the catchment pad (Table 5.3). The first sheet of the catchment pad was red, providing a contrast between the light and dark coloured ejecta and the paper. The remaining sheets of the catchment pad were white.

5.3.1.1 Local Disruption Analysis

Local disruption in the target includes the impact crater and regional fracturing caused by the impact. Each material, post-impact, was assessed by measuring the diameter of the impact crater, including the crater rim. The length of regional fractures were measured from the crater rim to the end of the fracture. These measurements were performed using calipers and a Leica optical microscope in the UKC Impact Laboratory.

Table 5.2 presents the data obtained during the local disruption analysis for each material, including the crater diameter, at its widest point, and the length of the largest regional fracture.

Table 5.2: Results obtained during the local disruption anaysis of the terminal IDG material selection experiments. In each case the projectile was a 1.0 mm diameter steel projectile impacting the terminal IDG at 5.0 $\mathrm{km\,s^{-1}}$. The longest fracture lengths on each target are listed.

Shot No.	Material	Crater Diameter (mm)	Fracture Length (mm)
IDG 01	Nylon	2.1	7.8
IDG 02	Acetal	3.8	1.2
IDG 03	PVC	2.9	4.7
IDG 04	PTFE	10.2	No fractures
IDG 05	Aluminium	2.9	No fractures
IDG 06	Syntactic foam	3.0	No fractures
IDG 07	Polycarbonate	3.2	10.2
IDG 08	Polyurathane	5.5	5.3
IDG 09	Silicone elastomer	2.1	4.2

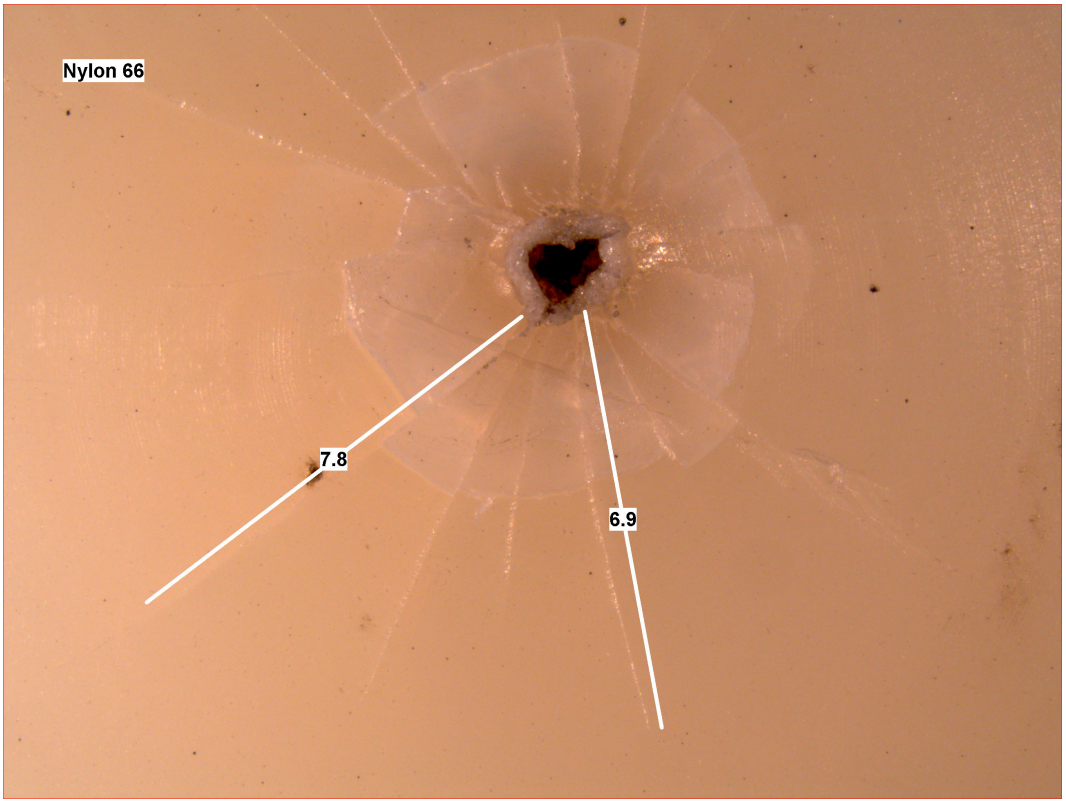

Figure 5.11: Photograph of the nylon target post impact. The dimensions of the fractures in the image are in millimeters (mm).

Disruption Analysis: Nylon

The nylon target had an impact crater with a diameter of 2.1 mm and a raised, melted, lip surrounded the crater. In addition to the crater, the nylon target had more than 15 axial fractures, and approximately four radial fractures, with different diameters. The longest axial fractures was 7.8 mm. Figure 5.11 is a photograph of the nylon impact crater and its regional fractures.

The overall local disruption on the nylon spanned a circular area with a diameter of 17.7 mm. Although the diameter of the impact crater was deemed acceptable, the number and length of the regional fractures were unacceptable, because such fractures could lead to further breakup in space and have an effect on acoustic waves passing through the material during subsequent impacts. Hence, nylon was ruled out of contention as a candidate for the terminal IDG material.

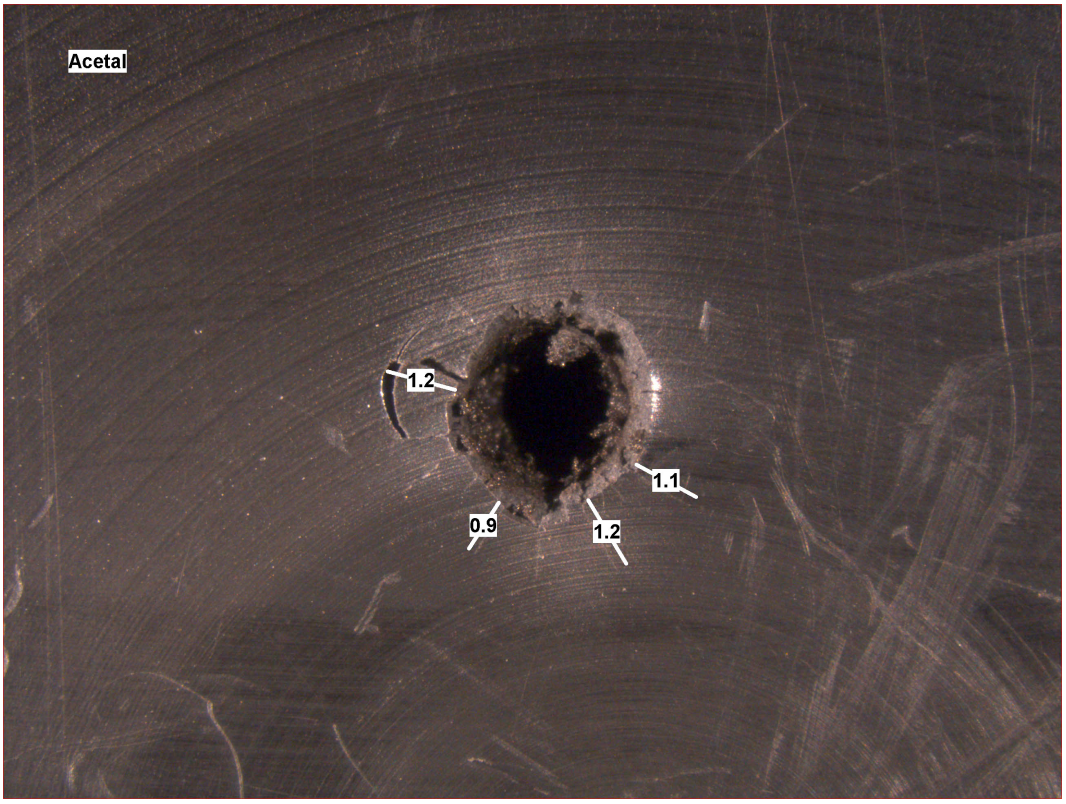

Figure 5.12: Photograph of the acetal target post impact. The dimensions of the fractures in the image are in millimeters (mm).

Disruption Analysis: Acetal

The acetal target had an impact crater with a diameter of 3.8 mm and there was no evidence of a raised lip surrounding it. In addition to its large impact crater, the acetal, had approximately 14 axial fractures and at least one radial fracture. Although the regional fractures in the acetal were relatively small, with a maximum length of 1.2 mm, they had caused part of the crater rim to detach from the material. This detachment of material would lead to unwanted ejecta. Figure 5.12 is a photograph of the acetal impact crater and its regional fractures.

The overall local disruption on the acetal spanned a circular area with a diameter of 6.2 mm and although the regional fractures were small, the size of the impact crater and the possible material detachment near the crater rim was also deemed unacceptable. Hence, acetal was ruled out of contention as a candidate for the terminal IDG material.

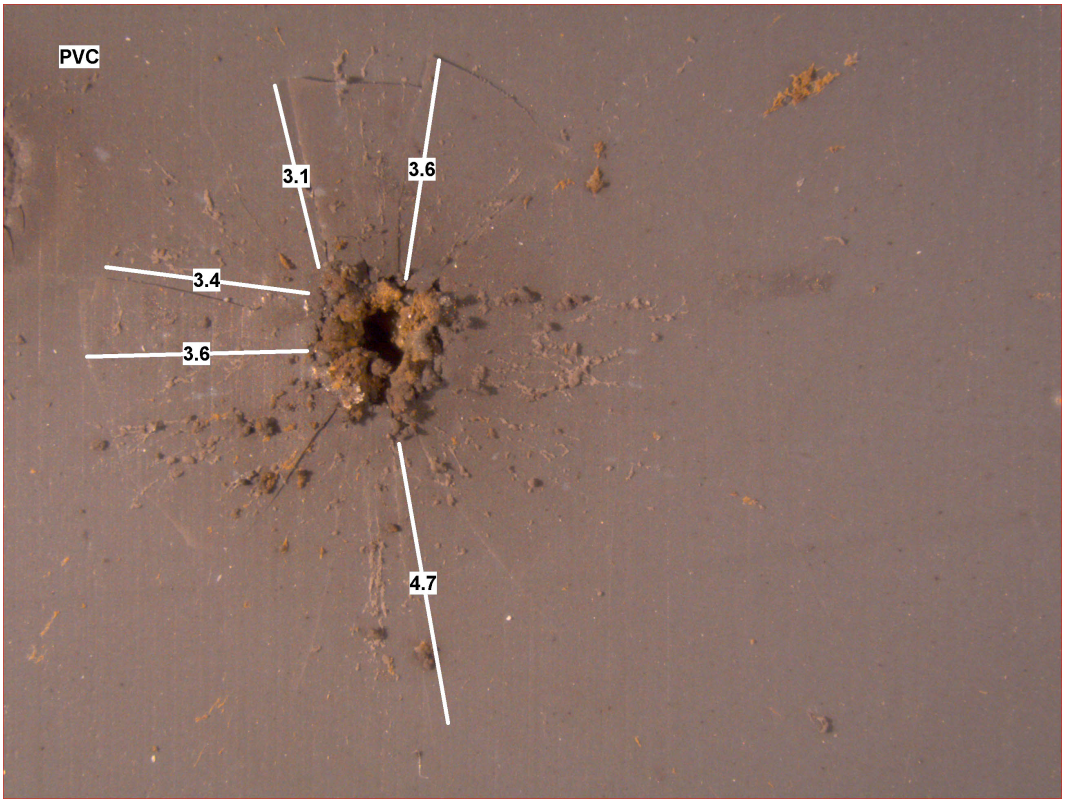

Figure 5.13: Photograph of the PVC post impact. The dimensions of the fractures in the image are in millimeters (mm).

Disruption Analysis: PVC

The PVC target had an impact crater with a 2.9 mm diameter and the crater experienced deformation, possibly, caused by melting. In addition to the impact crater, the PVC, had approximately 10 axial fractures and at least two radial fractures with different diameters. The longest axial fractures were 4.7 mm. Figure 5.13 is a photograph of the PVC impact crater and its regional fractures.

The overall local disruption on the PVC spanned a circular area with a diameter in the region of 12.3 mm. Although the diameter of the impact crater was acceptable, the number and length of the regional fractures were unacceptable. Hence, PVC was ruled out of contention as a candidate for the terminal IDG material.

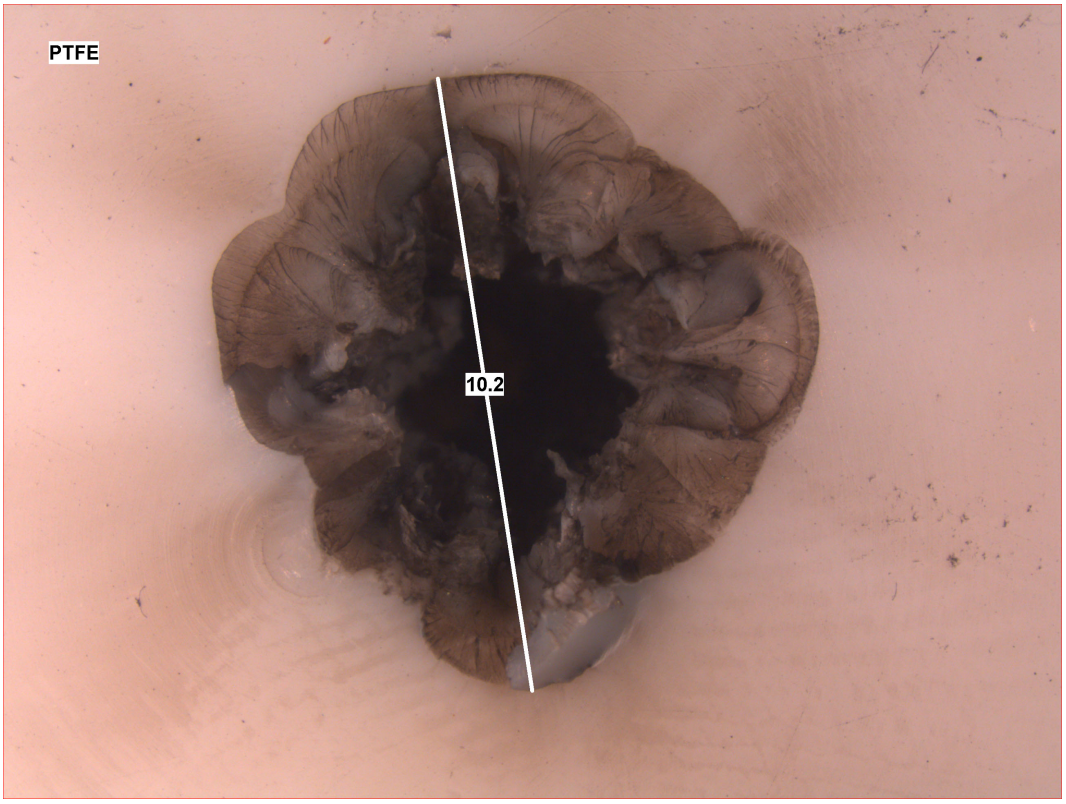

Figure 5.14: Photograph of the PTFE target post impact. The dimensions of the impact crater in the image are in millimeters (mm).

Disruption Analysis: PTFE

The PTFE target had a very large, 10.2 mm diameter, impact crater but, there was no evidence of a raised lip surrounding it. However, the impact crater's rim had a very irregular shape, which suggests significant fragmentation may have occurred during the impact (discussed in Section 5.3.1.2). Interestingly, the PTFE target exhibited no evidence of axial or radial regional fractures. Figure 5.14 is a photograph of the PTFE impact crater.

The overall local disruption on the PTFE spanned a circular area with a diameter in the region of 10.2 mm. Although the absence of regional fractures was extremely desirable, the diameter of the impact crater was too large and hence, PTFE was ruled out as a candidate for the terminal IDG material.

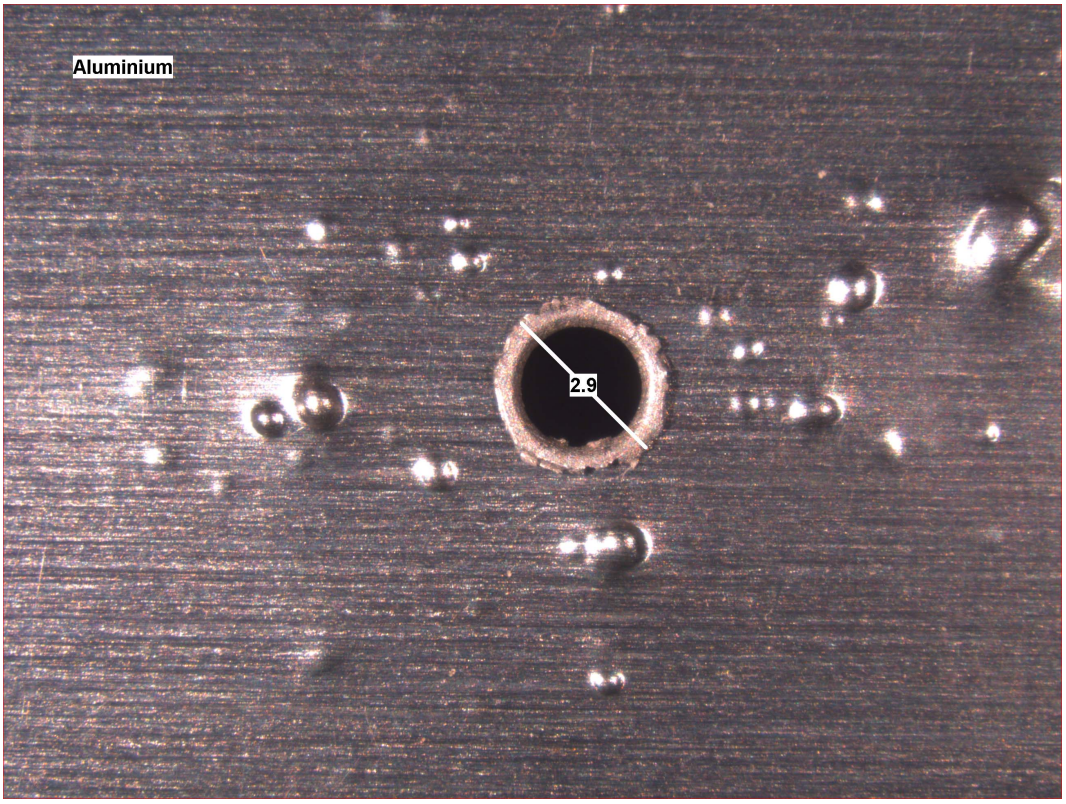

Figure 5.15: Photograph of the aluminium target post impact. The dimensions of the impact crater in the image are in millimeters (mm).

Disruption Analysis: Aluminium

The aluminium experiment was designed in a slightly different way to the other "semi-infinite" material experiments. The aluminium was configured as a minature Whipple shield to reduce its impact ejecta. The Whipple shield had a 0.28 mm thick bumper plate, a 20.0 mm standoff and an 8.0 mm thick backstop.

The aluminium Whipple shield had an impact crater with a 2.9 mm diameter and a raised lip surrounding it, a common occurrence in Whipple shield bumper plate impacts. The aluminium had no evidence of axial or radial regional fractures. Figure 5.15 is a photograph of the aluminium impact crater, with measurement annotations. In addition to the impact crater, there are convex dents surrounding the crater. These were caused by the ejecta from the 8.0 mm aluminium backstop behind the bumper plate. It is this violent ejecta that was avoided by using the Whipple shield configuration.

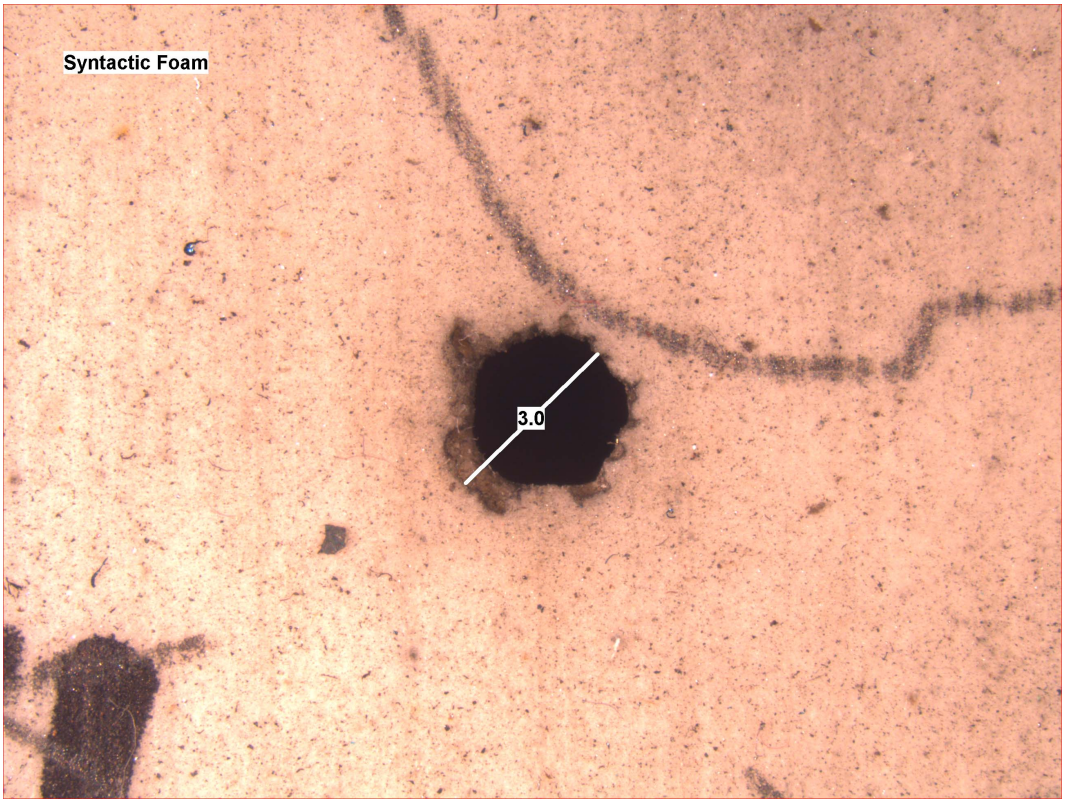

Figure 5.16: Photograph of the syntactic foam target post impact. The dimensions of the impact crater in the image are in millimeters (mm). Note the lack of fracturing.

The overall local disruption on the aluminium target spanned a circular area with a diameter of 2.9 mm. The relatively small impact crater and the absence of regional fractures was desirable, and hence, aluminium was selected as a potential candidate for the terminal IDG material.

Disruption Analysis: Syntactic Foam

The syntactic foam target had an impact crater with a 3.0 mm diameter and no evidence of a raised lip surrounding it. However, the impact crater's rim had a slightly irregular shape in certain parts, which suggests significant fragmentation may have occured during the impact. If fragmentation did occur, it will be confirmed during the ejecta analysis described below. The local disruption analysis showed no evidence of axial or radial regional fractures. Figure 5.16 is a photograph of the syntactic foam impact crater.

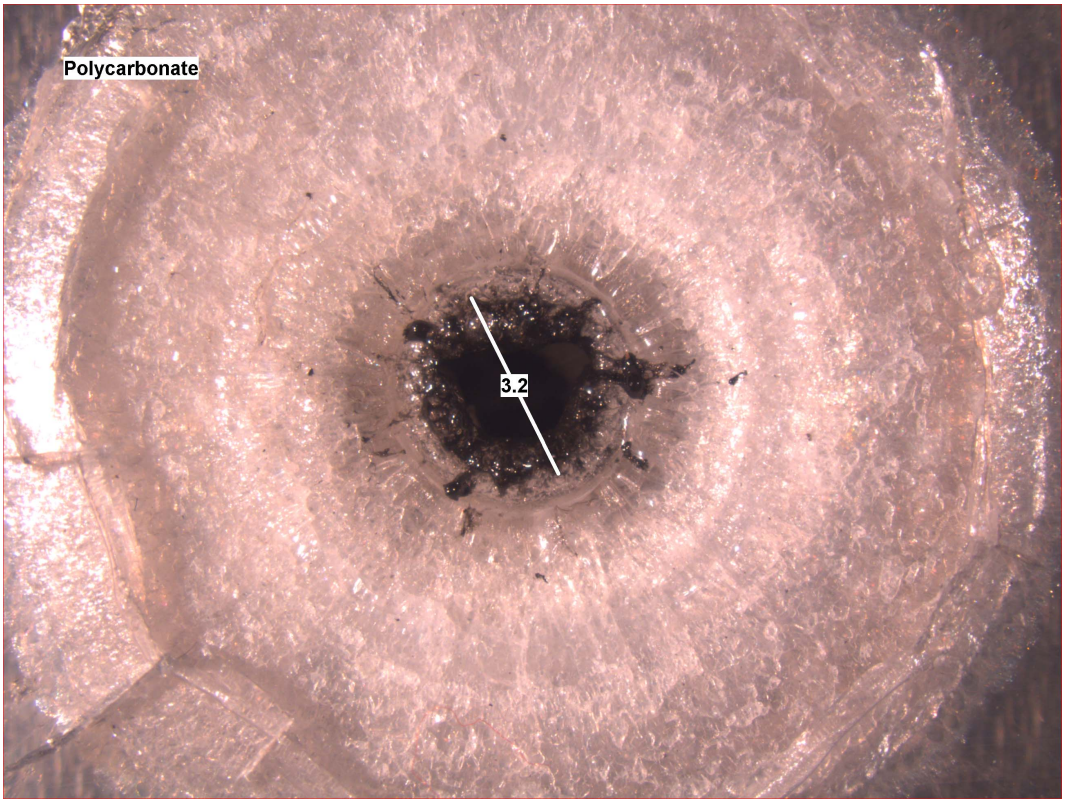

Figure 5.17: Photograph of the polycarbonate target post impact. The dimensions of the impact crater in the image are in millimeters (mm). Note the significant shattering surrounding the impact crater.

The overall local disruption on the syntactic foam spanned a circular area with a diameter of 3.0 mm. The relatively small impact crater and the absence of regional fractures was desirable, therefore, syntactic foam also was selected as a potential candidate for the terminal IDG material.

Disruption Analysis: Polycarbonate

The polycarbonate target had an impact crater with a 3.2 mm diameter. The crater rim had an irregular shape and had exhibited severe melting. Surrounding the crater was a circular region of deformed material exhibiting further melt and shattering. The diameter of this deformation was 18.5 mm. In addition to the impact crater and the surrounding deformation, the polycarbonate had approximately 13 axial fractures and 2 radial fractures with different diameters. The longest axial fractures were 10.2 mm.

Figure 5.17 is a photograph of the polycarbonate impact crater, the surrounding deformation and its regional fractures.

The overall local disruption on the polycarbonate spanned a circular area with a diameter of 18.7 mm. Although the diameter of the impact crater was acceptable, the size of the surrounding deformation and the regional fractures were unacceptable. Hence, polycarbonate was ruled out as a candidate for the terminal IDG material.

Disruption Analysis: Polyurethane

The polyurethane target had an impact crater with a 5.5 mm diameter, with no evidence of a raised lip surrounding it. However, the rim of the impact crater had a very irregular shape, which suggests significant fragmentation may have occurred during the impact. If fragmentation did occur, it will be confirmed during the ejecta analysis. In addition to the impact crater, the polyurethane, had 10 (subtle and possibly subsurface) axial fractures. The longest axial fractures were 5.3 mm. There was no evidence of radial regional fractures. Figure 5.18 is a photograph of the polyurethane impact crater and its regional fractures.

The overall local disruption on the polyurethane spanned a circular area with a diameter in the region of 16.1 mm. Although the diameter of the impact crater was deemed acceptable, the number and length of the regional fractures were unacceptable. Hence, polyurethane was not selected as a candidate for the terminal IDG material.

Disruption Analysis: Silicone Elastomer

The silicone elastomer target had an impact crater with a 2.1 mm diameter and there was no evidence of a raised lip surrounding it. In addition to the impact crater, there were signs of local disruption on the surface of the silicone elastomer, however, the bulk of the disruption occurred several millimeters below the surface. There were more than 18 axial fractures, and no evidence of radial fractures. The longest axial fractures were 4.2 mm. Figure 5.19 is a subsurface focused photograph of the impact crater and its regional fractures.

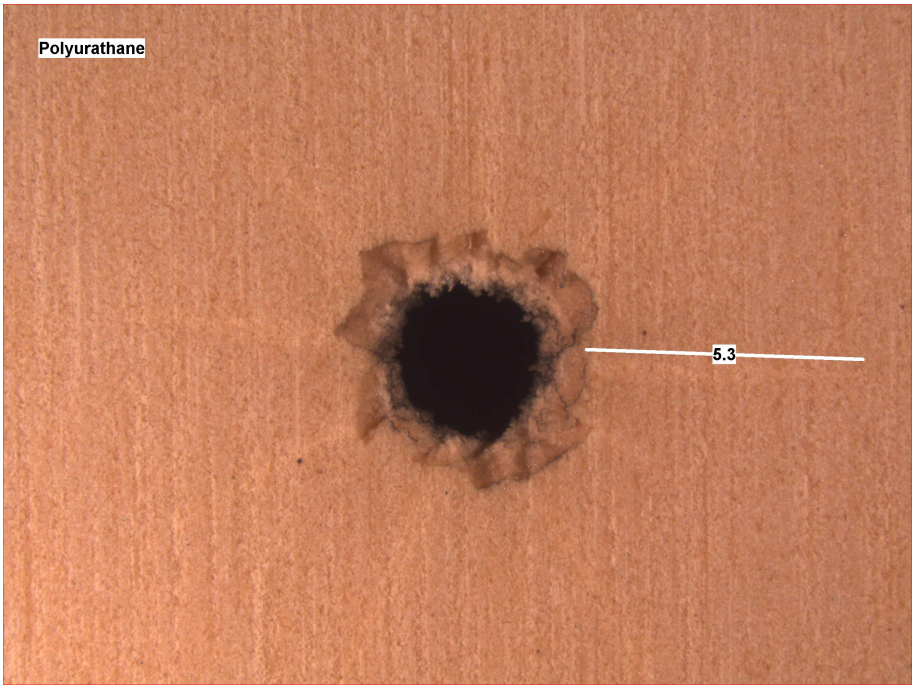

Figure 5.18: Photograph of the polyurethane target post impact. The dimensions of the radial fractures in the image are in millimeters (mm).

The overall local disruption on the silicone elastomer spanned a circular area with a diameter in the region of 10.5 mm. The relatively small impact crater was desirable, however, the length of the regional fractures was deemed unacceptable. Hence, silicone elastomer was ruled out as a potential candidate for the terminal IDG material.

Disruption Analysis: Summary

After analysing the local disruption of nine materials, aluminium and syntactic foam were selected as potential terminal IDG candidates, based on their limited local disruption, post-impact. Generally, the polymers reacted badly (i.e. they suffered from high levels of deformation) to the impacts. This is likely because they become more brittle under high strain rates. The syntactic foam, however, reacted well to the impacts, possibly due to its composite nature, which retards crack propagation, thus reducing cracks and fragmentation. The materials were then further tested to determine the differences in their impact ejecta properties, which would affect their suitability for the detector (see below).

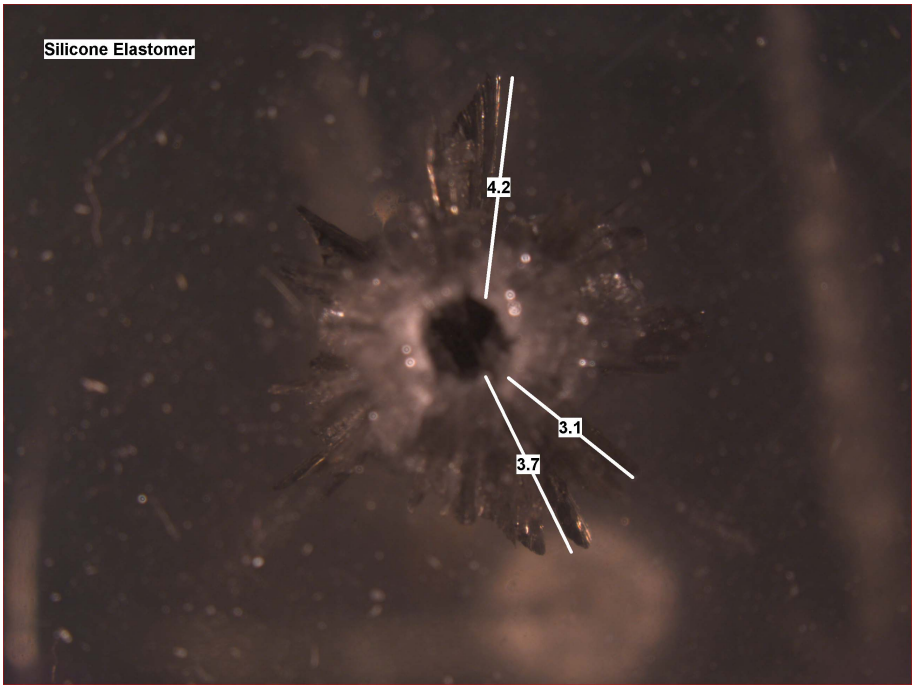

Figure 5.19: Photograph of the silicone elastomer target post impact. The dimensions of the radial fractures in the image are in millimeters (mm).

5.3.1.2 Ejecta Analysis

Although analyses of impact ejecta for each material were carried out, this section concentrates on the aluminium and syntactic foam. Additional analysis of the impact ejecta from other materials with noteworthy impact ejecta characteristics is summarised in Table 5.3. Note, as the ejecta are irregularly shaped, length is defined as the maximum dimension of an individual fragment.

The size of impact ejecta, for each of the nine materials, was assessed by selecting the largest pieces of ejecta embedded in the catchment pad after each experiment, and measuring their cross section (Figure 5.20) using a Leica optical microscope. The penetrating potential was assessed by counting the number of catchment pad sheets that were penetrated by individual ejecta.

Table 5.3: Ejecta data from the terminal IDG material selection experiments, showing the shot number, material, ejecta length and depth of penetration.

Shot No.	Target Material	Ejecta Length (µm)	Depth of Penetration (No. of sheets)
IDG 01	Nylon	624	0
IDG 02	Acetal	1188	1
IDG 03	PVC	2865	1
IDG 04	PTFE	1687	2
IDG 05	Aluminium	N/A	3
IDG 06	Syntactic foam	32	0
IDG 07	Polycarbonate	3866	3
IDG 08	Polyurathane	228	0
IDG 09	Silicone Elastomer	401	1

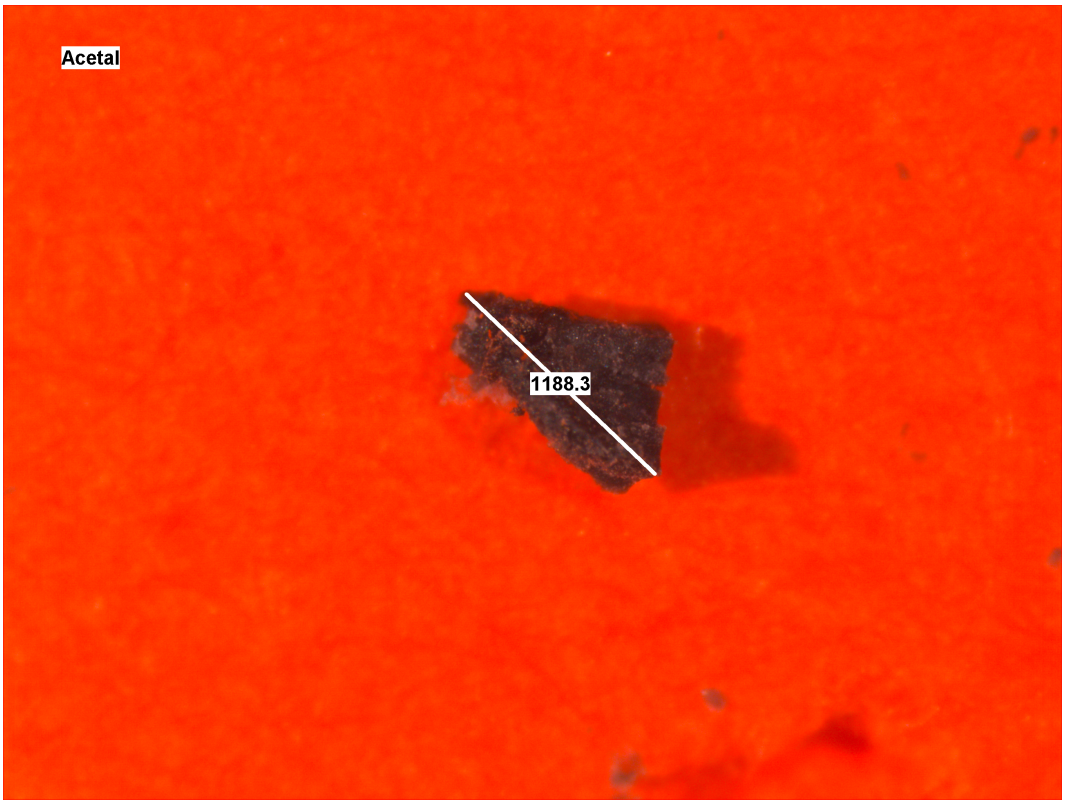

Figure 5.20: An individual piece of acetal ejecta (removed from the catchment pad) being measured. The dimensions are in micrometers (µm).

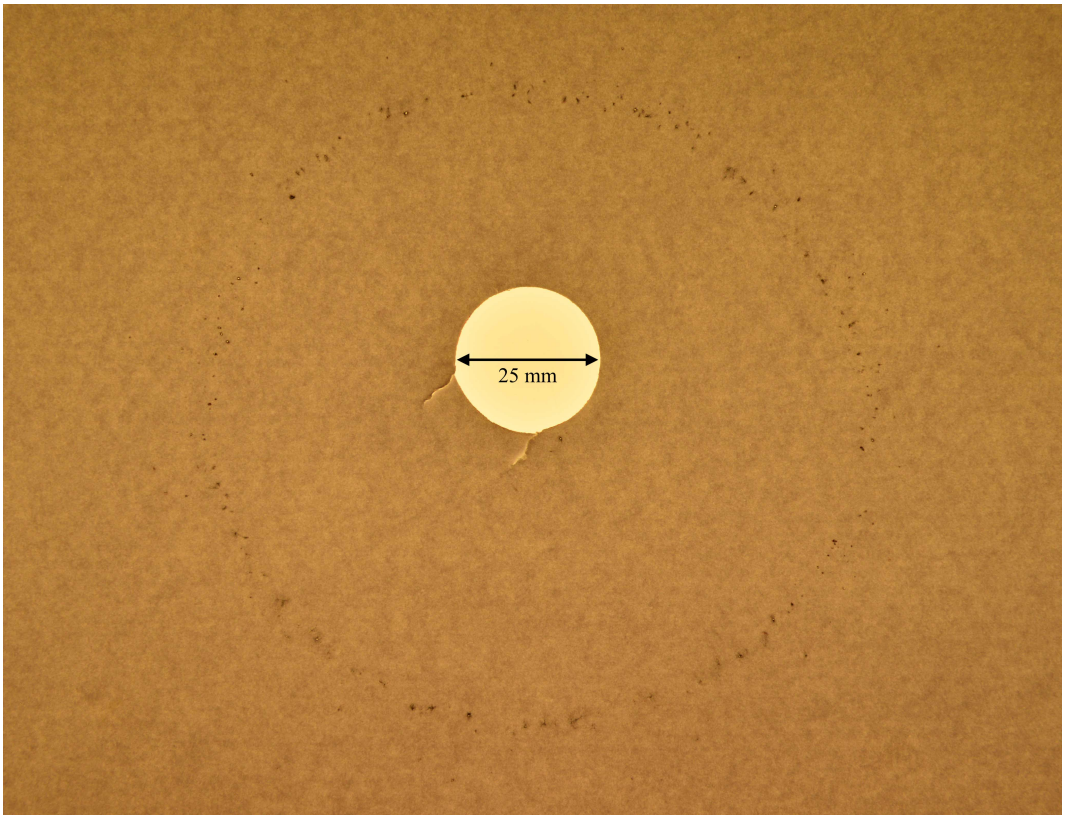

Figure 5.21: Photograph of the concentric ring of ejecta on the second sheet of the catchment pad from the aluminium target.

Ejecta Analysis: Aluminium

Analysis of the catchment pad with the naked eye, revealed a large number of ejecta and craters forming a concentric ring with a diameter of approximately 114 mm. Figure 5.21 is a photograph of the concentric ring on the second sheet of the catchment pad.

Observed under the microscope, however, indivdual ejecta were undetectable. Instead, small traces of a metallic residue were present, which made length measurements of indivdual ejecta unattainable. The patches of metallic residue were measurable, and the largest had a cross-sectional length of approximately 1.5 mm.

Impact craters on the first sheet of the pad suggested that penetrations did occur. Furthermore, when the second, third and fourth sheets of the catchment pad were analysed, successive traces of the metalic residue were detected. However, the only evidence of impact cratering was on the first and second sheets (Figure 5.22). The

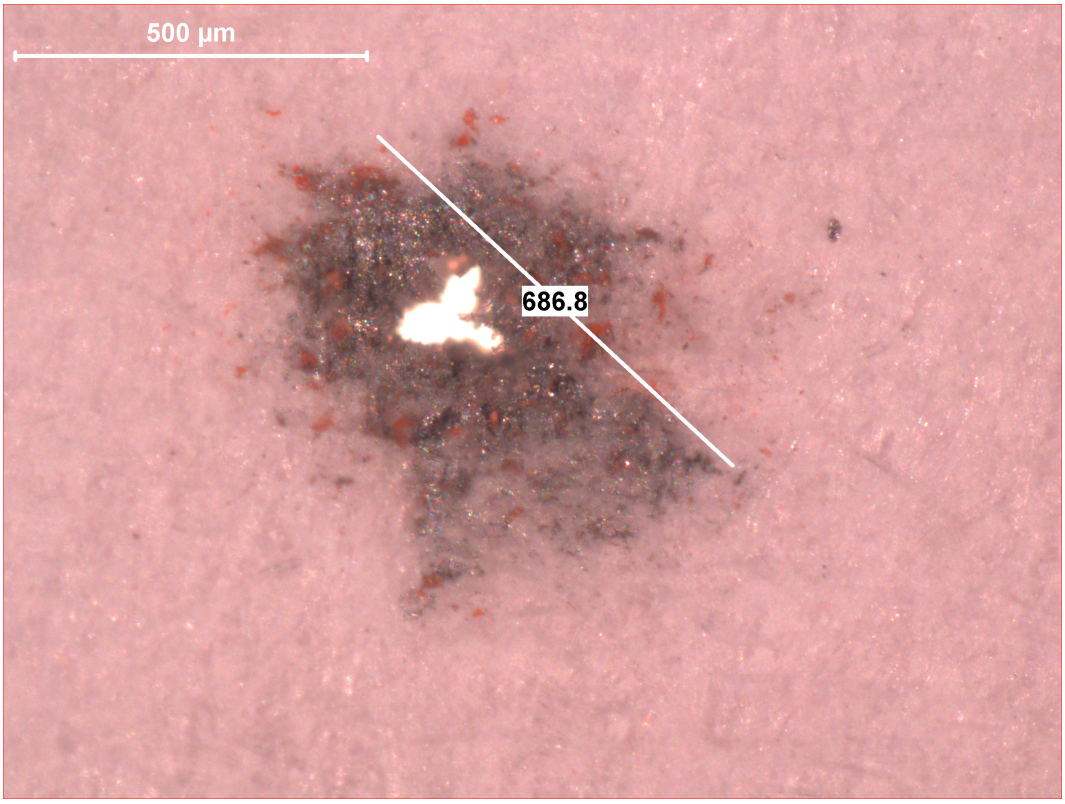

Figure 5.22: Photograph of the metallic residue deposited on the second sheet of the catchment pad with perforation crater. The dimensions are in micrometers (µm).

observations could be explained by hydrodynamic flow, i.e. relatively large droplets of molten aluminium penetrating the first and second sheets of the catchment pad and then dispersing and saturating the subsequent sheets (as a liquid or vapour), depositing metallic residue. Figure 5.23 is a photograph of the metalic residue on the fourth sheet of the pad.

Under normal circumstances, the absence of individual ejecta would be a positive characteristic for the terminal IDG material, but the cross-sectional length of metallic residue deposited on the catchment pad, approximately 1.5 mm on the fourth sheet, was deemed unacceptable as large ejecta could accelerate deterioration of the Kapton substrates on the primary and secondary IDGs. The aluminium ejecta penetrated three sheets on the catchment pad, indicating high penetration potential, and therefore, was also deemed unacceptable. Furthermore, a large quantity of impact ejecta was observed on the catchment pad. Although the amount of ejecta does not directly affect

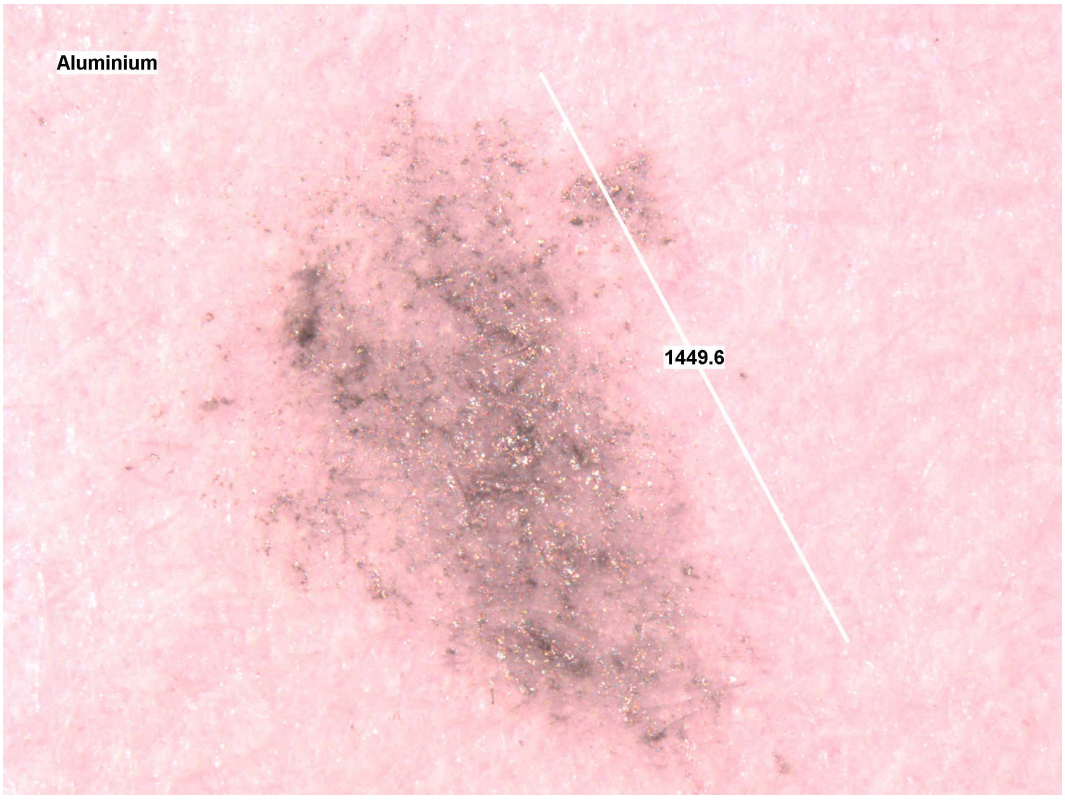

Figure 5.23: Photograph of the metallic residue deposited on the fourth sheet of the catchment pad. The dimensions are in micrometers (µm).

the scientific application, it can jeopardise the mission lifetime if a large area of the primary and secondary IDG were to become damaged. Hence, aluminium was ruled out of contention as a candidate material for the terminal IDG.

Ejecta Analysis: Syntactic Foam

Analysis of the syntactic foam catchment pad exposed a dark region surrounding the central hole, but indiviual ejecta were undetectable with the naked eye. Figure 5.24 is a photograph of the front sheet of the catchment pad.

To better understand the dark region surrounding the central hole, the catchment pad was examined under the Leica microscope. Individual traces of ejecta were identified, the largest with a cross-sectional length of 31.9 µm (Figure 5.25). There was no evidence of impact craters or catchment pad penetration.

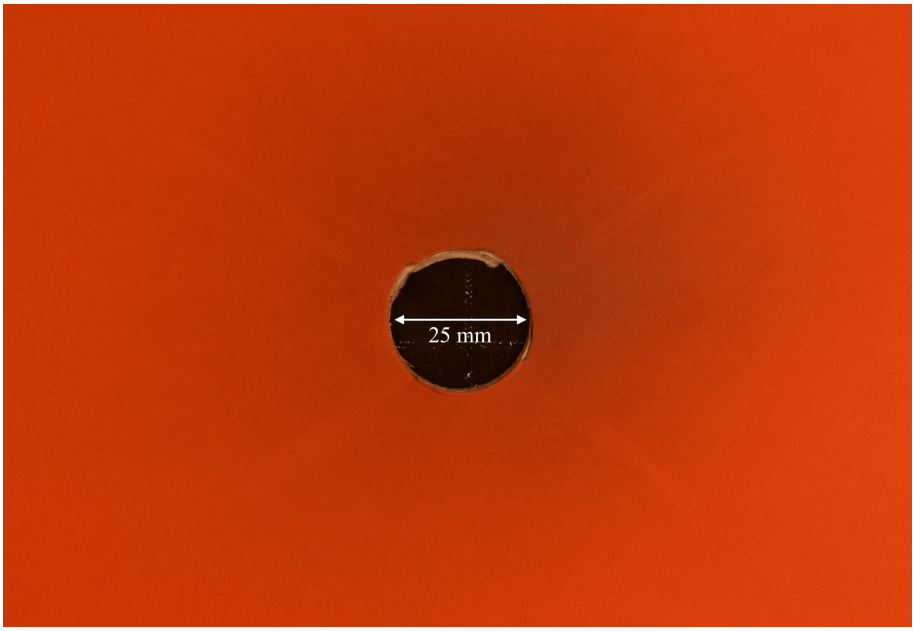

Figure 5.24: Photograph of the first sheet (target facing) of the catchment pad from the syntactic foam experiment.

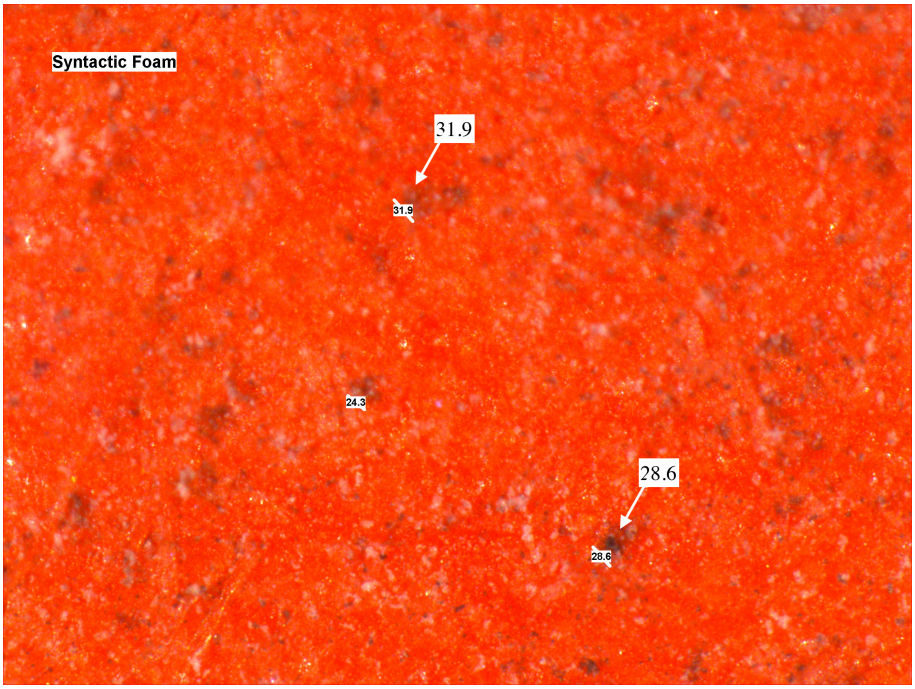

Figure 5.25: Photograph of the syntactic foam ejecta residue deposited on the first sheet of the catchment pad. The dimensions are in micrometers (µm).

The (microscopic) cross-sectional length of individual impact ejecta was acceptable. Additionally, there was no penetration of syntactic foam ejecta through the catchment pad sheets, which was clearly a major advantage. Hence, the syntactic foam maintained its status as the best candidate for the terminal IDG.

Ejecta Analysis: Other Materials

The silicone elastomer was not shortlisted as a potential terminal IDG material, due to its large regional fracturing. The small amount of impact ejecta, however, was extremely desirable and worth mentioning, as it could prove to be a useful material in other applications that require mitigation of impact ejecta. Figure 5.26 is a photograph of the first sheet (target facing) of the silicone elastomer catchment pad. The largest individual ejecta had a cross-sectional length of $\sim$400 µm. It is the low number of impact ejecta, however, that is most significant, although it is worth noting that some ejecta did penetrate the first sheet of the catchment pad.

In contrast to the silicone elastomer, the PTFE had a large quantity of impact ejecta. During the local disruption analysis, concerns were raised over the potential for large fragmentation during PTFE impacts. Indeed, analysis revealed that fragments, possibly millimetres in size, may have impacted the catchment pad. However, there is a degree of uncertainty in these measurements since the largest ejecta did not embed in the catchment pad and was therefore unmeasurable. Figure 5.27 is a photograph of the catchment pad from the PTFE experiment.

To summarise, the overall analysis strongly suggested that syntactic foam significantly outperformed the other materials in the local disruption and impact ejecta experiments. It had a compact impact crater without any regional fracturing and it produced microscopic impact ejecta that failed to penetrate the first layer of the catchment pad. Hence, syntactic foam was chosen to be the material used in the terminal IDGs. This was the first time syntactic foam has been used for this purpose, so it was necessary to review its space qualification characteristics.

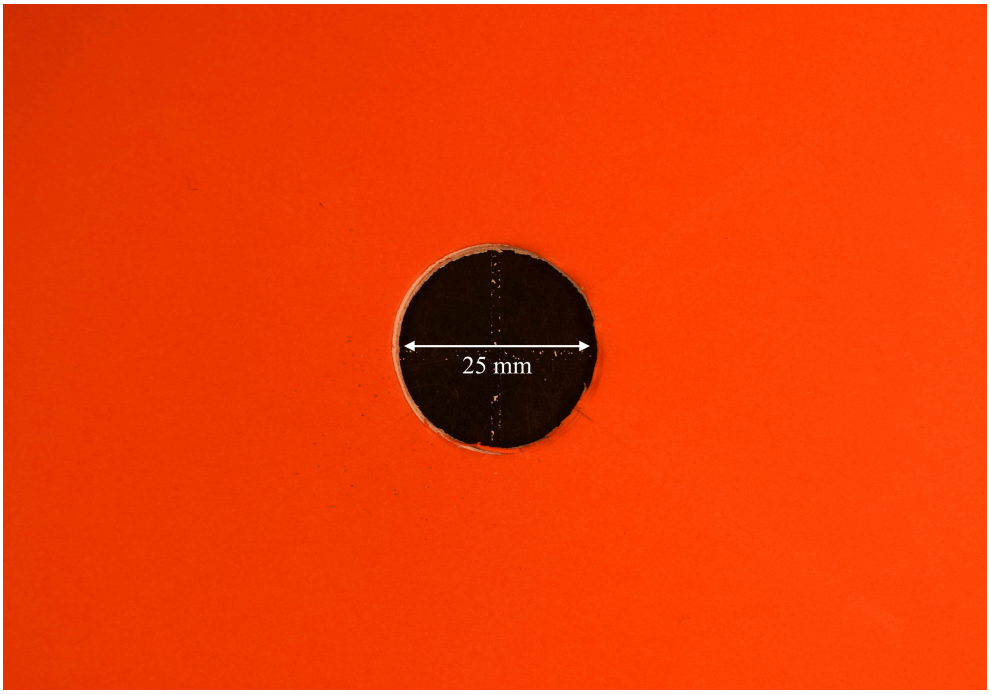

Figure 5.26: Photograph of the first sheet (target facing) of the catchment pad from the silicone elastomer experiment. Note the lack of ejecta in the catchment pad.

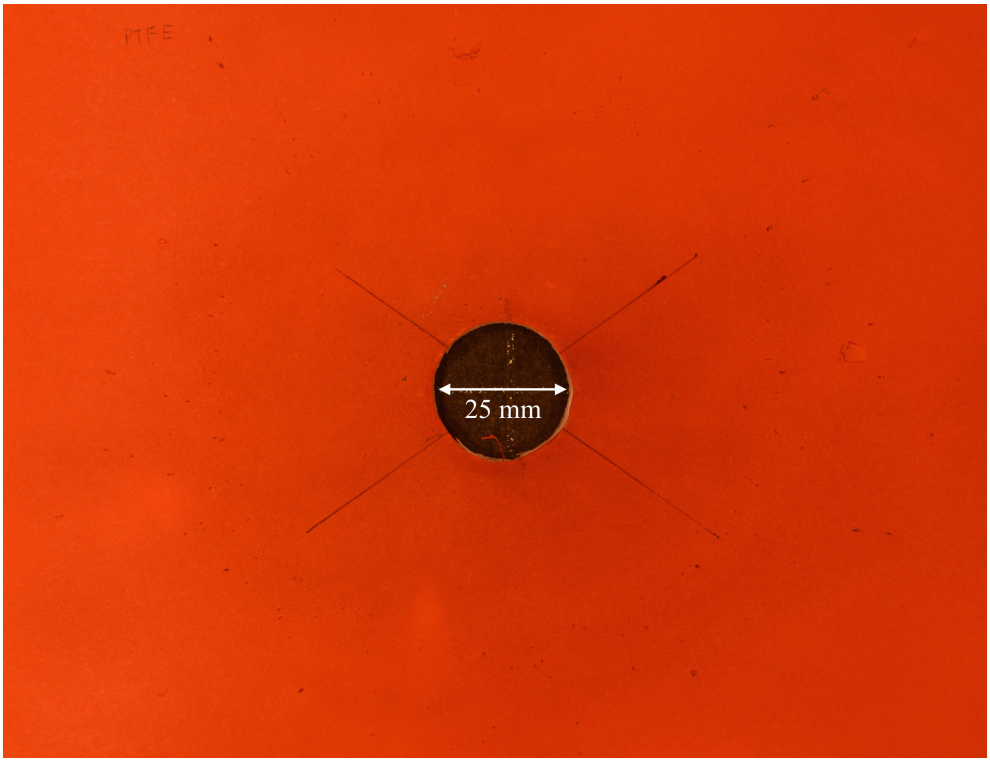

Figure 5.27: Photograph of the first sheet (target facing) of the catchment pad from the PTFE experiment. Note the number of ejecta in the catchment pad.

5.3.2 Syntactic Foam Space Qualification

Since spacecraft in LEO are subject to extreme temperature fluctuations, high vacuum and intense radiation, materials for use in space must meet certain requirements before they are qualified. These include; (1) the capability to function in high vacuum, (2) very low outgassing to prevent contamination, (3) resistant to ultraviolet radiation, (4) resistant to charged particle radiation, (5) resistant to atomic oxygen erosion, (6) resistant to large temperature fluctuations and (7) the ability to survive mission lifetime (Willis and Hsieh, 2000).

The syntactic foam satisfied the scientific requirements for the terminal IDG, however, it was unknown whether it would be eligible for use in space. Hence, a small block of syntactic foam was subject to a basic space qualification process in the UKC Impact Laboratory. During the space qualification process, the outgassing of the syntactic foam was assessed in addition to its reaction to high temperatures and low vacuum.

The syntactic foam block had dimensions of $90.7 \times 82.8 \times 22.3$ mm and a mass of 63.53 g at ambient temperature prior to the qualification process. It was then placed into a desiccator to remove any moisture. This was an important step as moisture could have affected its mass and be misconstrued as outgassing in a later stage of the space qualification process. After 139 hours, the syntactic foam was removed from the desiccator and weighed. Its new mass was 63.52 g, which indicated that 0.01 g of moisture had been removed from its overall mass. The amount of water mass lost is significantly less than 0.1 %, hence the water content is considered insignificant.

The syntactic foam was then baked at 80.0 °C in a vacuum oven at a pressure less than 10.0 mbar (Figure 5.28). After 166 hours, it was removed from the vacuum oven and weighed. Its new mass was 63.48 g indicating that 0.04 g, or 0.06 % recovered mass loss (RML), of material had been released from the syntactic foam. The general requirement for outgassing in space qualified materials, based upon the ESA micro-VCM test (ECSS-Q-70), is an RML <1.0 %. Therefore, the syntactic foam could be

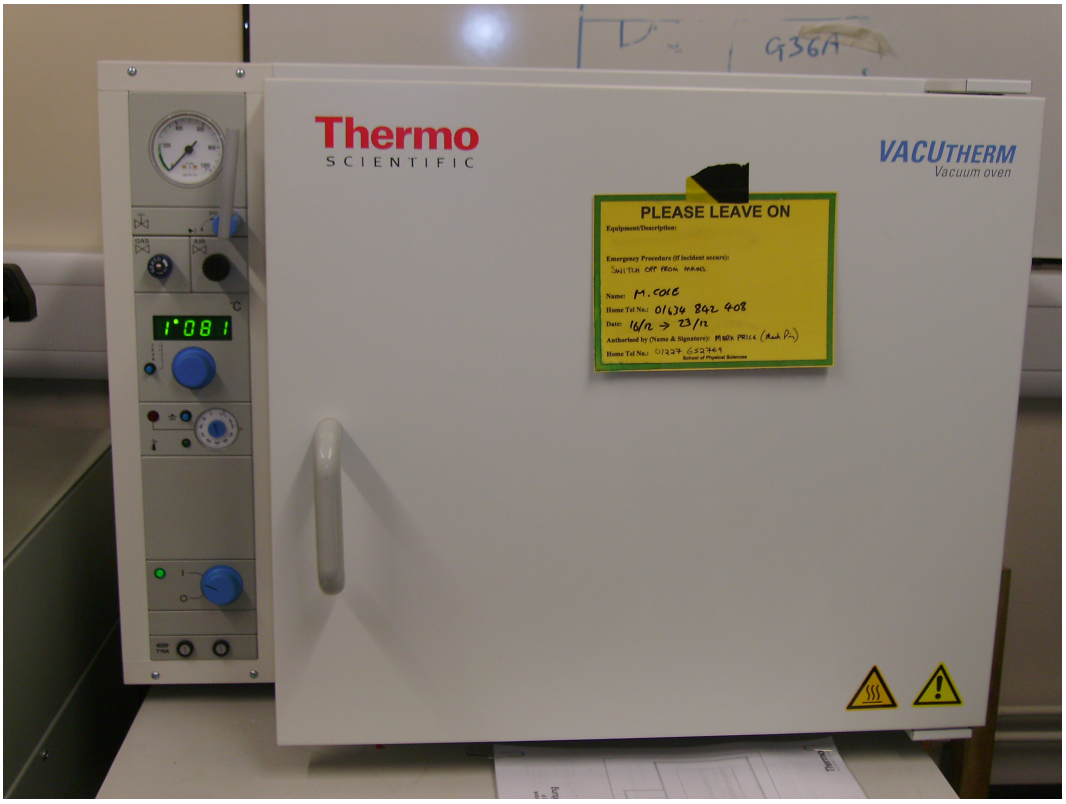

Figure 5.28: Photograph of the vacuum oven used during the space qualification process.

considered space qualified, in terms of its stability in a vacuum. Furthermore, the foam appeared unaffected by the heat. Criteria (3), (4), (5) and (7) could not be tested using the facilities available at the University of Kent and were left for future work. Criteria (3) could be tested by exposing the syntactic foam to ultra-violet radiation for extended periods, whilst monitoring its structural integrity. Criteria (4) and (5) could be tested in dedicated facilities designed to mimic the space environment (charged particle radiation and atomic oxygen) and check surface damage. Criteria (7) is fulfilled by ensuring the fluence of particles/radiation is comparable to that expected during the mission life time.

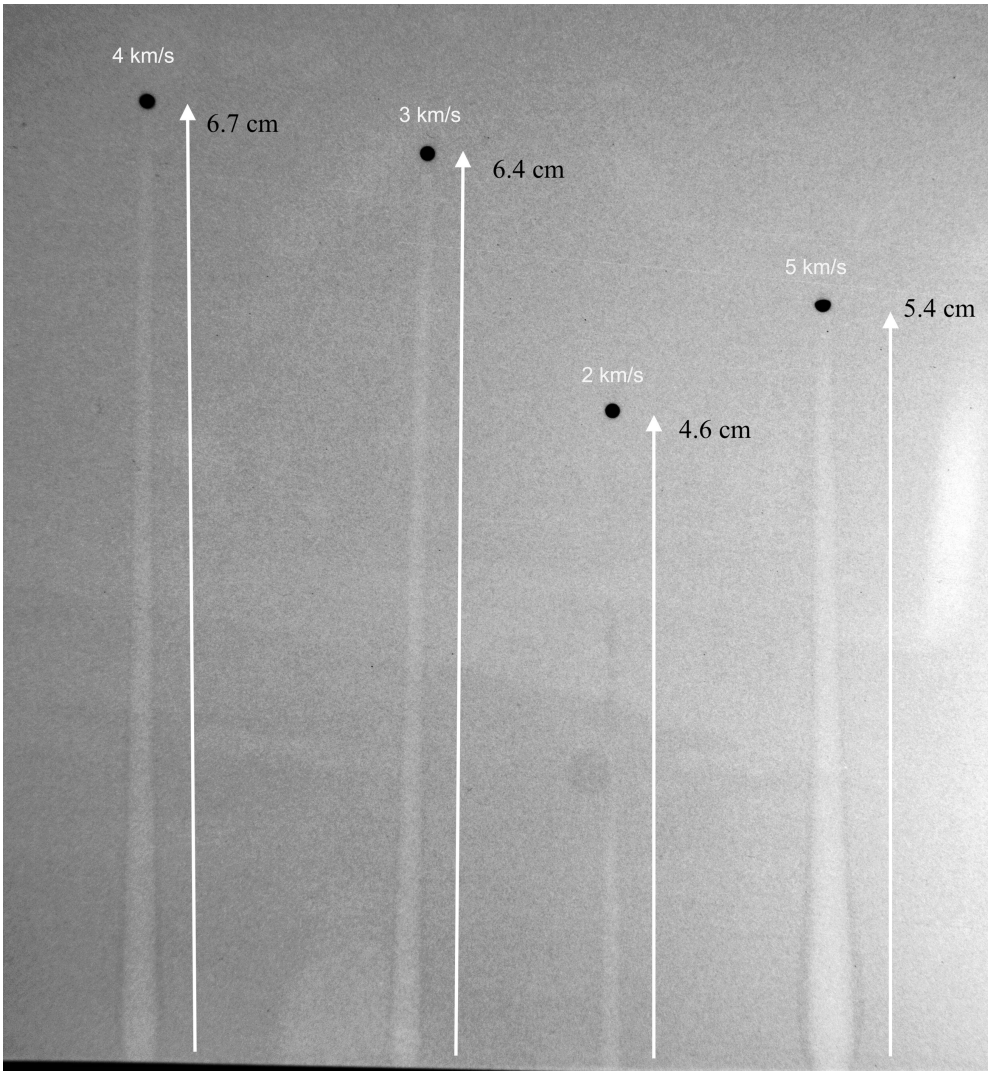

Figure 5.29: X-ray of the syntactic foam after the depth impact experiments showing entry trails of the projectiles. The terminal particles are the black spheres.

5.3.3 Terminal IDG Dimensions

The primary function of the terminal IDG is to act as a passive sink for OD/ID particles so that all of an impactor's kinetic energy is transferred to the syntactic foam. If particles were to penetrate the syntactic foam, kinetic energy would be lost, compromising the accuracy of data acquired by the terminal IDG.

A set of four experiments were conducted to investigate the depth of projectiles penetrations into syntactic foam. A block of the foam was impacted with spherical

Table 5.4: Data from the Terminal IDG dimension experiments, showing the shot number, impact velocity and impact depth.

Shot No.	Velocity ($\mathrm{km\,s^{-1}}$)	Impact Depth (cm)
IDG-D 01	2.01	4.6
IDG-D 02	3.25	6.4
IDG-D 03	4.05	6.7
IDG-D 04	5.08	5.4

stainless steel projectiles, with a 1.0 mm diameter, at a range of different velocities and then X-rayed for analysis. Table 5.4 presents the findings of the experiments, including the velocity and impact depth of the projectiles.

The impact depth increased with respect to velocity for projectiles in the $\sim$2 $\mathrm{km\,s^{-1}}$ to $\sim$4 $\mathrm{km\,s^{-1}}$ range. The projectile with 5.08 $\mathrm{km\,s^{-1}}$ velocity, however, had a significantly shorter impact depth. X-ray analysis, presented in Figure 5.29, suggests that a combination of energy loss through projectile deformation and increased entry trail width was responsible for the lower impact depth at a velocity of 5.08 $\mathrm{km\,s^{-1}}$.

Equation 5.1 shows how to calculate the volume of a frustrum, and can be used to approximate the volume of each entry trail with the intention of uncovering a correlation between trail volume and impact velocity.

$$V = \frac{\pi}{3} h(R^2 + Rr + r^2) \tag{5.1}$$

Where V ($\mathrm{mm^3}$) is the volume, h (mm) is the length and R (mm) and r (mm) are the radii at the base and top of the entry trail, respectively. Table 5.5 shows the impact velocity and corresponding volume of each entry trail. There was no apparent correlation between the entry trail volume and impact velocity.

The dimensions of the syntactic foam used in the terminal IDG during this research were 30.8 $\times$ 31.2 $\times$ 7.1 cm. A terminal IDG thickness of 7.1 cm was chosen due to the

Table 5.5: Volume of entry trails in syntactic foam for impacts at $2\,\mathrm{km\,s^{-1}}$, $3\,\mathrm{km\,s^{-1}}$, $4\,\mathrm{km\,s^{-1}}$ and $5\,\mathrm{km\,s^{-1}}$.

Velocity ($\mathrm{km\,s^{-1}}$)	Entry Trail Volume ($\mathrm{mm^3}$)
2.01	65.7
3.25	68.1
4.05	195.0
5.08	121.4

results of the depth experiments. The longest depth was from the $4.0\,\mathrm{km\,s^{-1}}$ impact, which had a depth of 6.7 cm, creating a 0.4 cm tolerance. The width and height of the syntactic foam used in the terminal IDG was dictated by the supplier's standard dimensions.

5.4 Prototype: ODIN-2

The fourth prototype, ODIN-2, was a full configuration including the three IDGs in combination. The primary and secondary IDGs had plastic frames with outer dimensions of 600 mm × 600 mm and inner dimensions of 510 mm × 510 mm. A Kapton substrate, 25 µm thick, was mounted parallel to each of the plastic frames on the primary and secondary IDGs and secured with adhesive tape. Rubber buffers were inserted between the Kapton and the frames to prevent acoustic edge reflection. Four PVDF sensors were orthogonally adhered to the aft surface of each Kapton substrate. The sensors were positioned 64 mm from the edge of each frame and 382 mm from each other, creating a $\sim 146 \times 10^3\,\mathrm{mm^2}$ sensitive region on the primary and secondary IDGs. The secondary IDG had a 188 mm standoff from the primary IDG, providing a large enough distance to calculate time of flight measurements.

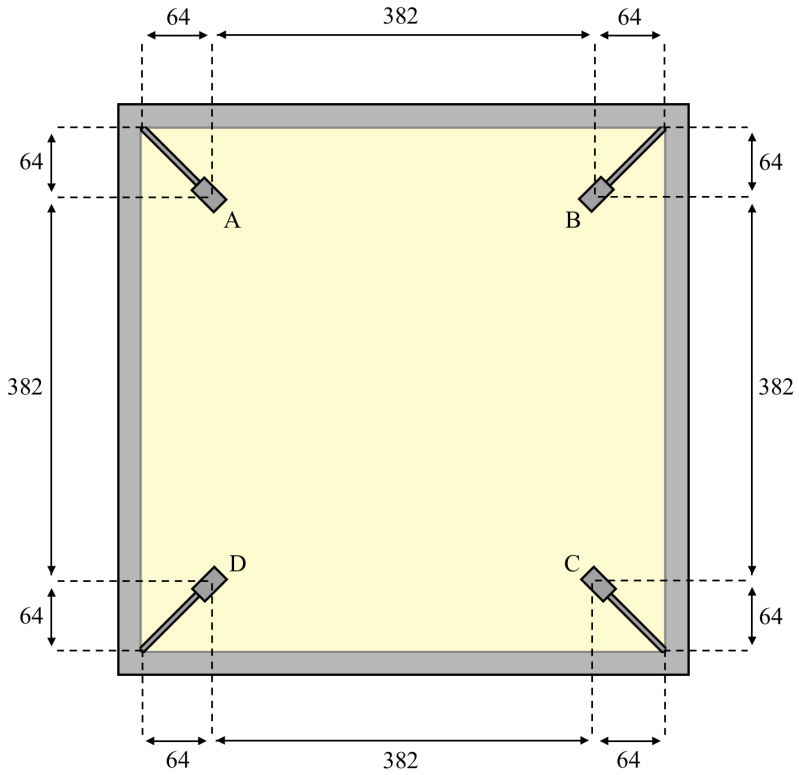

Figure 5.30: A schematic of the primary and secondary IDG on ODIN-2 showing the four PVDF sensors, A, B, C and D. All dimensions are in millimeters (mm).

The syntactic foam block from the ODIN-SF prototype was reused as the terminal IDG and had a 200 mm standoff from the secondary IDG, again, providing a large enough distance to calculate time of flight measurements if required. A schematic of the primary and secondary IDGs used on ODIN-2, showing the position of each PVDF sensor, can be seen in Figure 5.30. A schematic and photograph of the full ODIN-2 configuration can be seen in Figures 5.31 and 5.32, respectively.

ODIN-2 was tested in the laboratory and performed with great success during a set of full system proof-of-concept experiments. ODIN-2 (1117.1 g frame) was eventually discontinued so that a prototype with an alternative light-weight (344.0 g) aluminium frame could be developed, representing a 69 % weight reduction. A photograph of ODIN-2 can be seen in Figure 5.32.

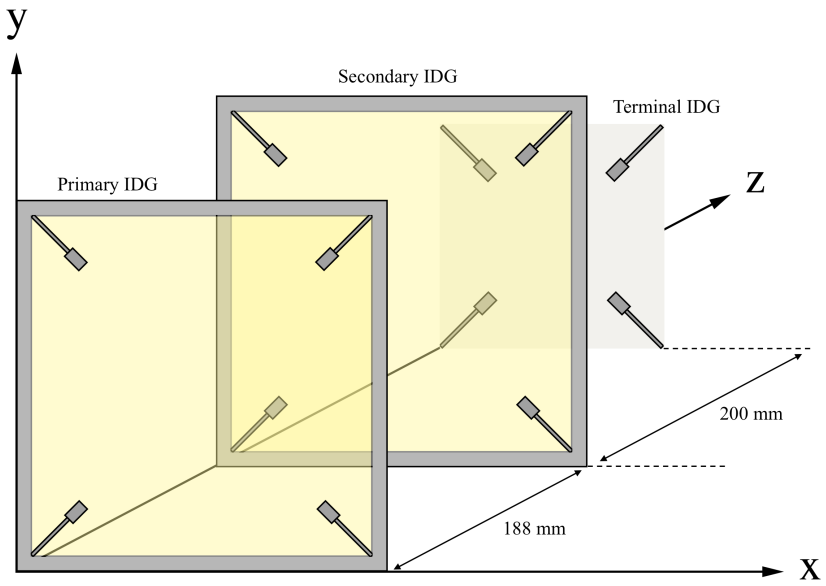

Figure 5.31: A full schematic of the ODIN-2 configuration, showing the primary IDG, secondary IDG and terminal IDG.

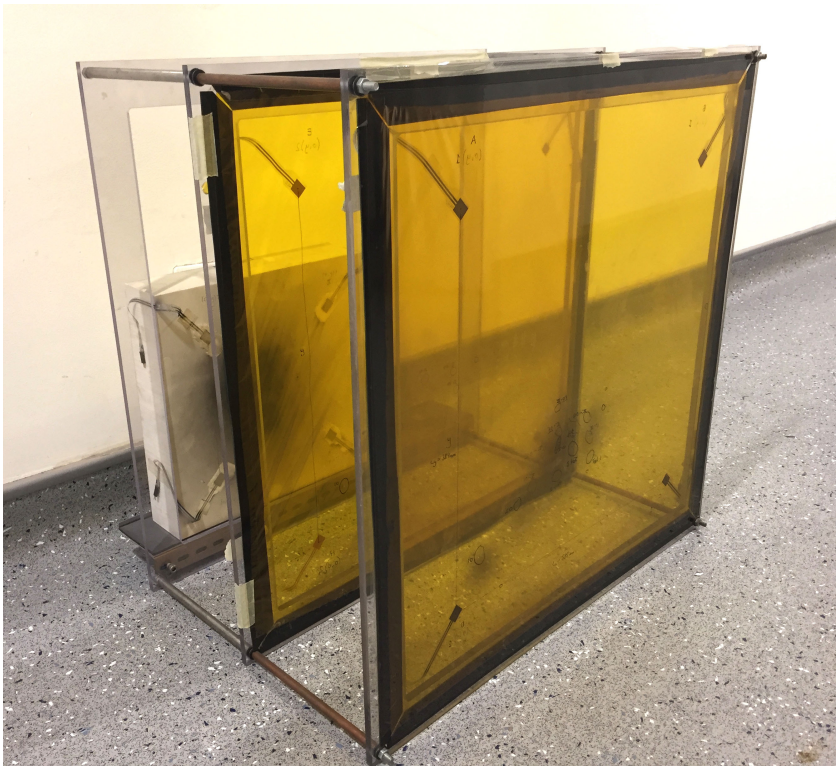

Figure 5.32: A photograph showing the full configuration of ODIN-2. The PVDF sensors and black rubber buffer can be seen.

5.5 Prototype: ODIN-3

The fifth, and final, prototype, ODIN-3, was also a full configuration of ODIN, which included the primary, secondary and terminal IDGs. The primary and secondary IDGs had folded aluminium frames, which significantly reduced weight, while greatly increasing structural integrity. The outer dimensions of the frame were 566 mm × 566 mm and the inner dimensions were 514 mm × 514 mm. A Kapton substrate, 25 µm thick, was mounted parallel to each of the plastic frames on the primary and secondary IDG. The Kapton substrates were secured with adhesive tape that folded over the frame, similar to the ODIN-Beta. Four PVDF sensors were orthogonally adhered to the aft surface of each Kapton substrate. The sensors were positioned 64 mm from the edge of each frame and 386 mm from each other, creating a $\sim 149 \times 10^3$ mm^2 sensitive region on the primary and secondary IDG. The secondary IDG had a 145 mm standoff from the primary IDG. The ODIN-SF was used as the terminal IDG and had a 145 mm standoff from the secondary IDG. The standoff distances on the ODIN-3 prototype were reduced in order to achieve a more compact detector, while remaining large enough to make accurate time of flight measurements. A schematic of the primary IDG and secondary IDG used on the ODIN-3, showing the position of each PVDF sensor can be seen in Figure 5.33.

ODIN-3 was discontinued after three shot experiments as a result of poor acoustic data. The acoustic signals appeared to show signs of a prolonged gas blast, spanning between ∼500 µs and ∼850 µs, which is approximately six times longer than gas blasts recorded during previous experiments. It is more likely, however, that the gas blast was strong enough to "rock" the lightweight aluminium frame of ODIN-3, causing the prolonged signal interference that was observed throughout the acoustic data (Figure 5.34). Alternatively, the acoustic interference could be due to faulty PVDF sensors. However, this is unlikely as three of the four sensors (B, C and D) recorded similar acoustic data (Figure 5.34). It is also unlikely that the remaining sensor (A) was faulty as the initial acoustic data, between 500 µs and 550 µs, was similar to Sensor B,C and

D. Due to time constraints, and a sufficient amount of data recorded during previous experiments, the acoustic interference recorded by ODIN-3 was not investigated further.

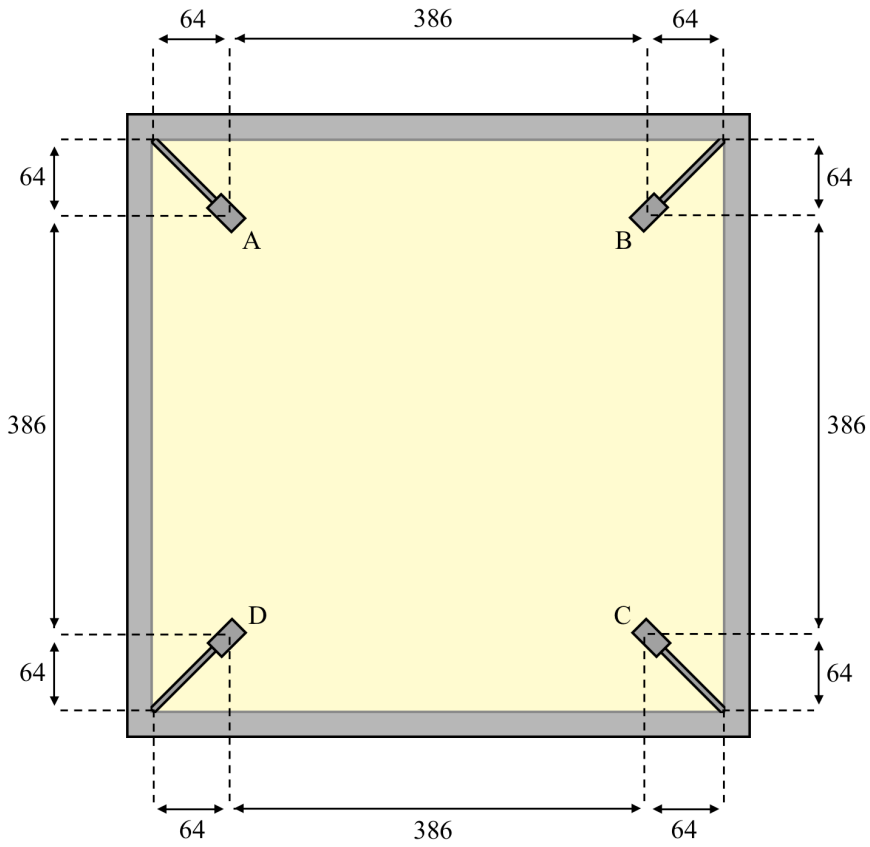

Figure 5.33: A schematic of the primary and secondary IDG on ODIN-3 showing the four PVDF sensors, A, B, C and D. All dimensions are in millimeters (mm).

5.6 Recommended Design

The recommended design of ODIN would include a three stage IDG configuration. It is suggested that the first two IDGs employ 25 µm thick Kapton substrates adhered to aluminium frames, and a terminal IDG constructed of syntactic foam. The standoff distance between the IDGs would depend on instrument constraints defined by the specific mission. However, it is recommended that standoff distances are to be no less than 100 mm to maintain time of flight accuracy.

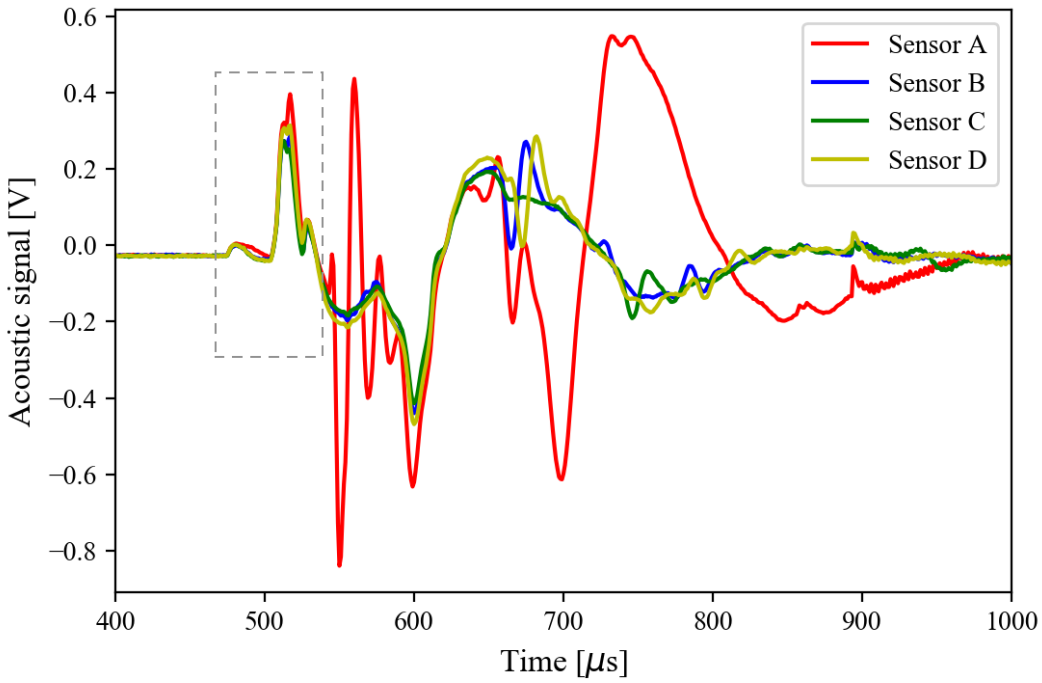

Figure 5.34: Example of the acoustic signals recorded, during an impact, by the ODIN-3 prototype. The gas blast is represented by the grey box.

It is recommended that four PVDF sensors are deployed orthogonally on each IDG, permitting the use of algorithmic methods to accurately calculate impact locations, whilst providing a redundancy in the event of sensor failure (convert to algebraic calculations). The sensors should be positioned at least 64 mm from the frames if no reflection damping techniques, such as rubber buffers between Kapton and frame, are deployed.

Flux predictions performed by Liou et al. (2015) using ORDEM 3.0 (2016) indicate that the flux of OD/ID in the ram direction of flight is approximately $600 - 2000$ /m^2/yr for particles where $d \geq 0.1$ mm but only $0.5 - 5$ /m^2/yr for particles where $d \geq 1.0$ mm at an altitude between 400 km and 900 km. Hence, to achieve meaningfull statistical sampling of the OD/ID population up to 2.0 mm within a mission lifetime of a few years, the distance between the sensors (sensitive area of detector) is recommended to be 500 mm. This enables the possibility of combining four detectors to create an overall active detection area of 1 m^2.

The effect of external vibrations on the acoustic data recorded by ODIN was highlighted in Section 5.5. In space, the detector would be subject to routine vibrations caused by spacecraft maintenance and operations. To prevent these external vibrations from interfering with signals of interested, it is suggested that an additional IDG is positioned behind the terminal IDG. This would provide an identical set of acoustic measurements that are not subject to impacts, but still exposed to external vibrations, acting as a background for the acoustic data.

Chapter 6

Impact Cartesian Coordinate Subsystem

The Impact Cartesian Coordinate (ICC) subsystem was designed to calculate the coordinates of impacts on the primary and secondary IDGs. Accurate impact coordinates on the first two detection gates are required to precisely calculate the distance and time between impacts on subsequent IDGs, and thus, the speed and trajectory of a particles passing through the detector. This Chapter starts by explaining how the ICC uses acoustic signals to measure impact coordinates, and is followed by a description of the proof-of-concept experiments. Finally, the results and analysis of the proof-of-concept experiments are presented.

6.1 ICC Operation

The ICC uses an algorithm in conjunction with the acoustic data recorded by the four PVDF sensors on the primary IDG, and the four PVDF sensors on the secondary IDG to calculate the impact coordinates of OD/ID on the primary and secondary IDGs. Although the process is the same, the ICC measures the impact coordinates on each

IDG independently. A three step process is used by the ICC to measure the impact coordinates on an IDG. The three steps are as follows:

1. Determine the signal arrival time at each sensor on the IDG.
2. Calculate the time delay between each signal's arrival time.
3. Consult a pre-calculated lookup-table to find the impact coordinates.

6.1.1 Signal Arrival Time

The first step in the process involves finding an accurate arrival time, t (µs), of the acoustic wave at each of the four PVDF sensors (A, B, C and D) on the primary IDG. The signal arrival time at each sensor is denoted as t_A, t_B, t_C and t_D (µs). Locating the precise arrival time of an acoustic signal can be difficult as natural oscillations and noise can mask the exact starting point. In this application, the signal arrival time at each sensor is used to find a temporal difference in the signals' arrival times. This permits the arrival time of a unique feature, such as the peak amplitude which is present on all signals, to be used rather than the actual start of the signal.

A Python script was written to identify the exact time at which the peak amplitude in a signal occurs. The ICC uses that peak amplitude for its arrival time calculations.

The acoustic signals recorded by the PVDF sensors are plotted against time and overlaid on the same graph, the data from each sensor is distinguished by a different colour. The overlay can make it hard to identify the unique features of individual signals, see Figure 6.1 (Left). The individual signals have been translated in the y-axis so that their unique features can be identified, see Figure 6.1 (Right). It is worth noting that the Python script does not perform this translation during its calculations and is only presented in this way here to make it easier for the reader to interpret. Furthermore, the signal magnitude is not used by the ICC, which means translating the signals in this way would not affect the results.

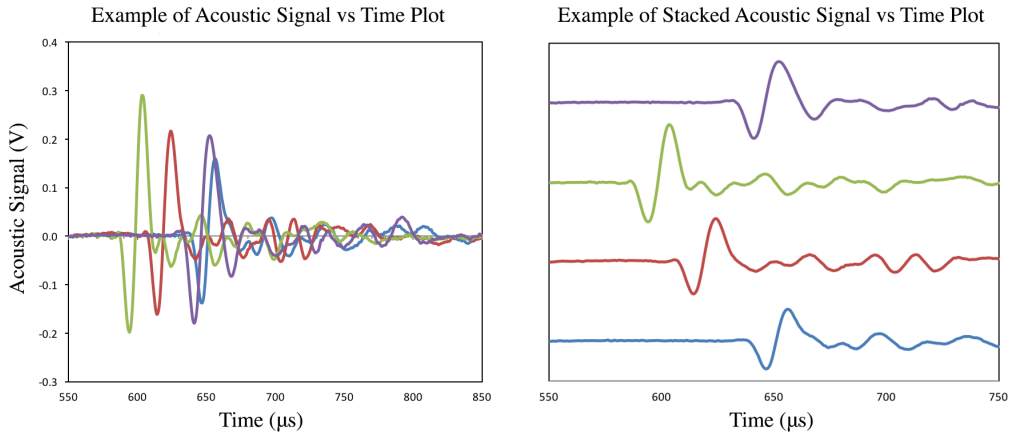

Figure 6.1: (Left) Example of real PVDF acoustic signals plotted against time. (Right) Example of the same signals stacked with respect to time so that features can be identified between each signal. Each coloured line corresponds to a different PVDF sensor.

The Python script is used to identify, and calculate, the relative arrival time of each signal by measuring the time of maximum amplitude. Once the relative signal arrival times are calculated, the ICC continues with step two.

6.1.2 Time Delay

The second step in the process involves finding the time delay, Δt (µs), between t_A, t_B, t_C and t_D. This is done computationally and is a very quick process. The start time, t_s (µs) is the time when the first signal (irrespective of the PVDF sensor that detected it) is recorded, and is subtracted from all of the other signal arrival times. i.e.

$$\Delta t_A = t_A - t_s \tag{6.1}$$

$$\Delta t_B = t_B - t_s \tag{6.2}$$

$$\Delta t_C = t_C - t_s \tag{6.3}$$

$$\Delta t_D = t_D - t_s \tag{6.4}$$

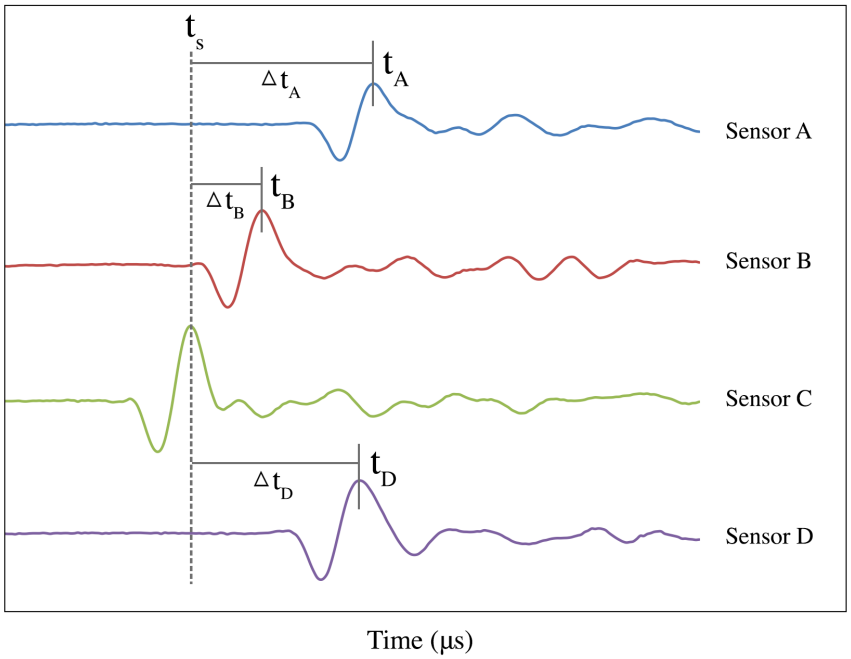

Figure 6.2: Diagram showing the time delay between the signals recorded by each of the PVDF sensors after an impact.

This process returns a unique time delay, Δt (µs), for each sensor, where the subscripts A, B, C and D represent each of the PVDF sensors. The time delay is zero for the sensor that is closest to the impact, and the distance from the remaining sensors to the impact location increases with respect to the time delay.

6.1.3 Lookup-Table

The third, and final, step in the process compares the recorded time delays with a pre-calculated lookup-table. The lookup-table is a simple indexing array that is used to minimise computational runtime. The lookup-table used by the ICC contains pre-calculated arrival time differences of acoustic signals at each sensor caused by impacts at every possible coordinate, with a resolution of 1 mm per coordinate, within the sensitive area on the primary and secondary IDGs. There are four lookup-tables that represent each quadrant on the IDGs.

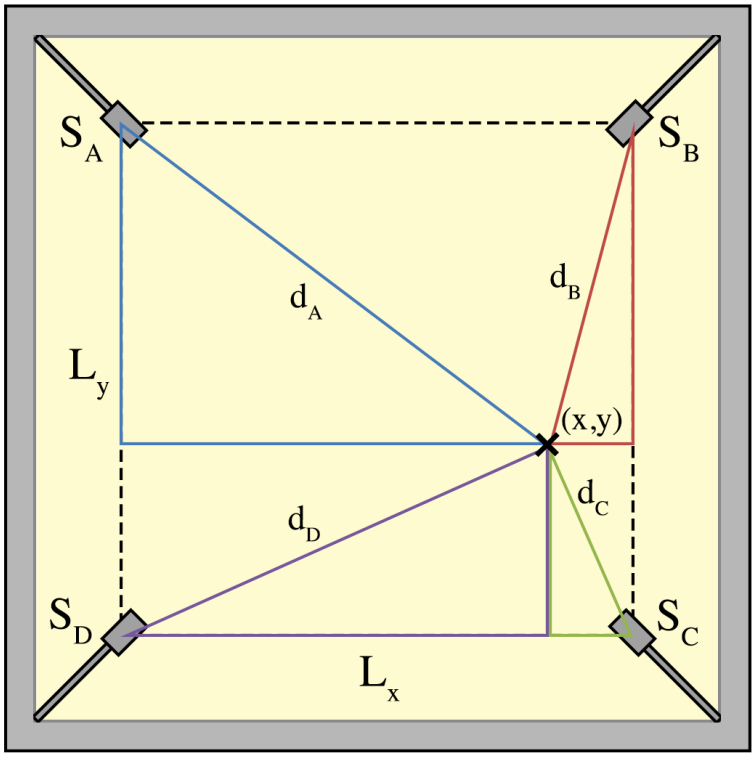

Figure 6.3: Diagram showing the different Pythagorean triangles that are used to measure the distance to each sensor.

The distance from an impact coordinate to all four sensors is calculated using the Pythagorean theorem, as seen in Figure 6.3. The equations below show the distance, d (mm) travelled by an acoustic signal from an impact at location (x, y) to each sensor. The subscripts A, B, C and D represent the corresponding distance to each sensor. The z-coordinate can be ignored during these calculations as it gives the location of the xy-plane that represents the IDG.

$$d_A = \sqrt{x^2 + (L_y - y)^2} \tag{6.5}$$

$$d_B = \sqrt{(L_x - x)^2 + (L_y - y)^2} \tag{6.6}$$

$$d_C = \sqrt{(L_x - x)^2 + y^2} \tag{6.7}$$

$$d_D = \sqrt{x^2 + y^2} \tag{6.8}$$

Where L_x (mm) and L_y (mm) represent the distance between the PVDF sensors (measured from the centre of each sensor) on the x-axis and the y-axis, respectively. The x-coordinate and y-coordinate of the impact are represented by x and y, respectively.

The speed of acoustic signals in the Kapton substrate is assumed to be constant, with a value of $1.59\,\mathrm{mm\,\mu s^{-1}}$, which has been calculated using known impact coordinates from calibration experiments previously conducted at UKC (unpublished data). It is possible that the speed differs during compression caused by shock waves, however, the shock front will be very small ($\sim$ µm) and thus, the overall effect is deemed negligible for this application. The distance, d (mm) to each sensor and the speed of the acoustic signal, c ($\mathrm{mm\,\mu s^{-1}}$) is used to calculate the travel time, T (µs) taken for the acoustic signal to reach each sensor from an impact.

$$T_A = \frac{d_A}{c} \tag{6.9}$$

$$T_B = \frac{d_B}{c} \tag{6.10}$$

$$T_C = \frac{d_C}{c} \tag{6.11}$$

$$T_D = \frac{d_D}{c} \tag{6.12}$$

Each IDG is divided into four quadrants Q_A, Q_B, Q_C and Q_D, as seen in Figure 6.4. The subscripts define each quadrant according to its nearest sensor. The sensor that receives the acoustic signal first indicates which quadrant the impact occurred in, and which lookup table to use, and determines the initial travel time, T_i (µs) to the closest sensor.

The time delay at each sensor, Δt (µs) is calculated by subtracting the initial travel time, T_i (µs) from the travel time, T (µs) to each sensor, A, B, C and D.

$$\Delta t_A = T_A - T_i \tag{6.13}$$

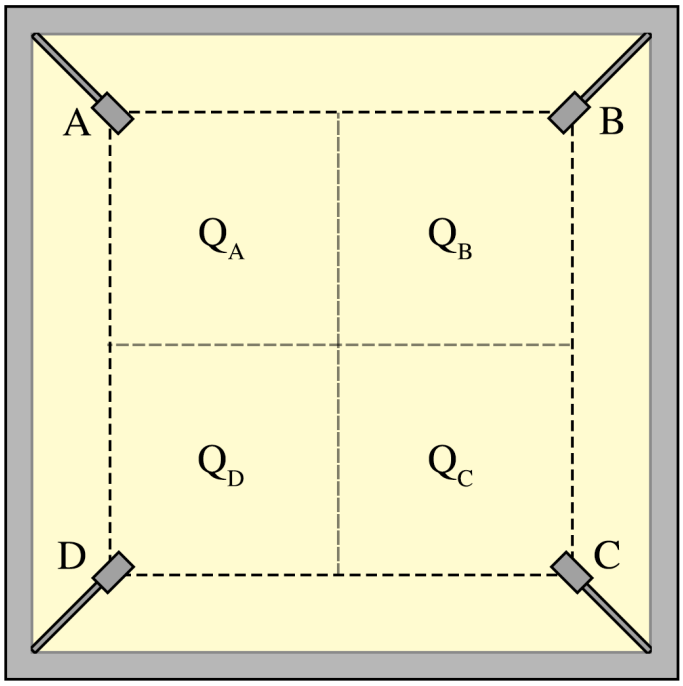

Figure 6.4: Diagram showing the different quadrants and their corresponding PVDF sensors.

$$\Delta t_B = T_B - T_i \tag{6.14}$$

$$\Delta t_C = T_C - T_i \tag{6.15}$$

$$\Delta t_D = T_D - T_i \tag{6.16}$$

The arrival time of the signals at each of the remaining sensors is dependent on the signal speed in the Kapton. Hence, the time delay is proportional to the distance of each sensor relative to the impact coordinate.

The temporal difference between the acoustic signal arrival time and its corresponding impact coordinate are inserted into the lookup-table; this process is repeated for every possible impact coordinate. The time delay recorded in the second step can then be used in conjunction with the time delay in the lookup table to locate the impact coordinate on the primary and secondary IDGs. $z = 0$ for impacts that occur on the primary IDG.

6.2 ICC Proof-of-Concept Experiments

Three sets of experiments were designed to simulate OD/ID impacts with prototypes of ODIN so that the performance of the ICC could be assessed under test conditions. The process was as follows:

1. Simulate OD/ID impacts with a prototype of the detector.
2. Measure the true coordinates of the impact on the primary and secondary IDG.
3. Run the ICC algorithm to calculate the corresponding impact coordinates.
4. Compare the true coordinates with the coordinates calculated by the ICC.

6.2.1 Simulating OD/ID Impacts

OD/ID impacts were simulated using the LGG facility at the University of Kent. Prototypes of ODIN were placed under a vacuum in the impact chamber of the LGG, and projectiles were accelerated towards different locations on the primary IDG at velocities comparable with OD/ID (i.e. hypervelocity). The acoustic responses to the subsequent impacts were recorded by the PVDF sensors and saved to a computer. The acoustic data was then processed by the ICC algorithm. The ODIN-Beta and ODIN-2 prototypes were used for these ICC proof-of-concept experiments.

Spherical stainless steel projectiles were used throughout the ICC proof-of-concept experiments as they have a high success rate in the LGG and would not deform on impact with the primary IDG. Helium gas at 90.0 bar was used when accelerating the projectiles to $\sim$3.0 km s^{-1} and hydrogen gas at 45.0 bar was used when accelerating the projectiles to $\sim$5.0 km s^{-1}. The projectiles had an incident impact angle of 0.0° for the majority of experiments, however, some had an incident angle of 15.0° and 30.0°. Three sets of experiments were conducted during the ICC proof-of-concept procedure. Full details of each set of experiments are presented below.

6.2.2 ICC-1 Experiments

The first set of experiments, ICC-1, included seven impacts with the primary IDG of the ODIN-Beta prototype. Spherical stainless steel projectiles with diameters ranging from 0.3 mm - 2.0 mm were accelerated to $\sim$5.0 km s^{-1} with an incident impact angle of 0.0°. Full details of the experiments can be found in Table 6.1.

Table 6.1: Parameters from the ICC-1 experiments, including the diameter and velocity ($\pm$1.0 %) of the projectiles. All of the projectiles had an incident angle of 0°.

Experiment	Diameter (mm)	Velocity (km s^{-1})
ICC-1.01	1.0	4.90
ICC-1.02	2.0	5.00
ICC-1.03	0.8	5.04
ICC-1.04	0.5	5.05
ICC-1.05	0.4	5.08
ICC-1.06	1.5	5.04
ICC-1.07	0.3	4.47

6.2.3 ICC-2 Experiments

The second set of experiments, ICC-2, included six impacts with the primary IDG on the ODIN-2 prototype. Spherical stainless steel projectiles with diameters ranging from 0.1 mm - 1.0 mm and were accelerated to $\sim$5.0 kms^{-1} with an incident impact angle of 0.0°. Full details of the experiments can be found in Table 6.2.

Table 6.2: Parameters from the ICC-2 experiments, including the diameter and velocity ($\pm$1.0 %) of the projectiles. All of the projectiles had an incident angle of 0°.

Experiment	Diameter (mm)	Velocity (kms^{-1})
ICC-2.01	0.3	5.25
ICC-2.02	0.8	4.93
ICC-2.03	0.5	5.31
ICC-2.04	1.0	4.93
ICC-2.05	0.4	5.17
ICC-2.06	0.1	5.07

6.2.4 ICC-3 Experiments

The third set of experiments, ICC-3, included eight impacts with the primary and secondary IDGs on the ODIN-2 prototype. Spherical stainless steel projectiles with diameters ranging from 0.3 mm - 1.5 mm were accelerated to speeds of either $\sim$3.0 kms^{-1} or $\sim$5.0 kms^{-1} with an incident impact angle of 0.0°, 15.0° or 30.0°. Full details of the experiments can be found in Table 6.3.

Table 6.3: Parameters from the ICC-3 shot programme, including the diameter, velocity ($\pm$1.0 %) and incident angle of the projectiles.

Experiment	Diameter (mm)	Velocity (kms^{-1})	Incident Angle (°)
ICC-3.01	1.0	4.61	0.0
ICC-3.02	1.5	3.16	0.0
ICC-3.03	1.0	2.97	0.0
ICC-3.04	0.8	2.93	0.0
ICC-3.05	0.5	3.09	0.0
ICC-3.06	0.3	3.04	0.0
ICC-3.07	0.8	4.99	30.0
ICC-3.08	0.8	4.88	15.0

6.2.5 Measured Impact Coordinates

The second step in the proof-of-concept process was to physically measure the true coordinates of the impacts on the primary and (where possible) secondary IDG of each prototype. Axes connecting the centre of each PVDF sensor were drawn onto the Kapton substrates to aid the coordinate measurements. The x-coordinate and y-coordinate of each impact were carefully measured from the x-axis and y-axis using a ruler, where each individual coordinate was represented by a 1.0 mm increment from the axis. Figure 6.5 shows the y-coordinate of an impact being measured in the laboratory.

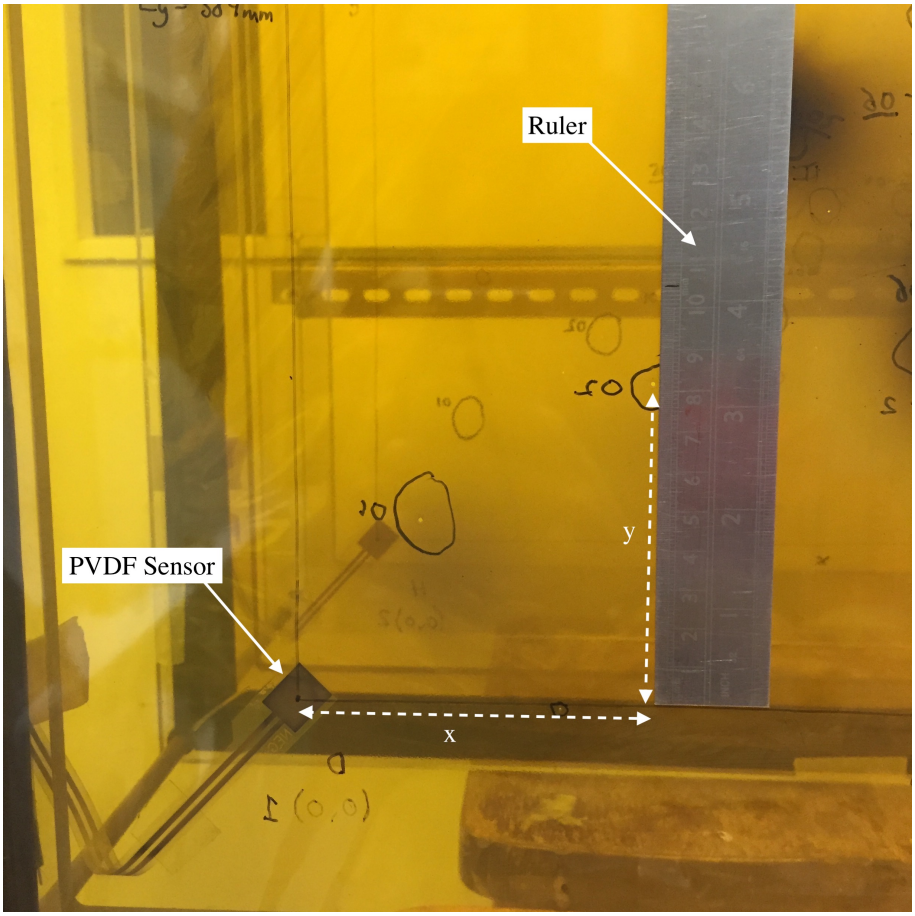

Figure 6.5: Photograph showing the coordinate measurement of an impact hole.

6.2.6 ICC Calculated Impact Coordinates

The third step in the proof-of-concept process was to run the ICC algorithm and allow it to calculate the coordinates of the same impacts using the acoustic signal data recorded by the PVDF sensors.

The ICC algorithm is the same for each of the prototypes, however, the lookup-table changes depending on the dimensions of the prototype. The ODIN-Beta prototype had an active area of 388.0 mm × 388.0 mm and the ODIN-2 prototype had an active area of 382.0 mm × 382.0 mm.

6.3 ICC Results

The results of the ICC experiments are presented here, with the comparison between the calculated and measured impact coordinates. This process provided a means to measure the robustness of the algorithm and assess the accuracy of the ICC.

6.3.1 ICC-1 Results

Table 6.4 presents the true impact coordinates that were measured in the laboratory, and the corresponding coordinates that were calculated by the ICC algorithm during the ICC-1 experiments.

Table 6.4: Data from the ICC-1 experiments, including the true coordinates (±1.0 mm), the coordinates calculated by the ICC and the deviation between them.

Experiment	True Coordinate (x, y, z)	ICC Coordinate (x, y, z)	Coordinate Deviation (mm)
ICC-1.01	(238, 179, 0)	(243, 178, 0)	5.1
ICC-1.02	(236, 222, 0)	(238, 221, 0)	2.2
ICC-1.03	(240, 259, 0)	(242, 259, 0)	2.0
ICC-1.04	(176, 182, 0)	(179, 183, 0)	3.2
ICC-1.05	(192, 223, 0)	(192, 226, 0)	3.0
ICC-1.06	(183, 121, 0)	(186, 124, 0)	4.2
ICC-1.07	(221, 109, 0)	(221, 109, 0)	0.0

The best result that was recorded during the ICC-1 experiments was ICC-1.07, where the ICC algorithm calculated the exact impact coordinates as those measured in the laboratory. The largest deviation was 5.1 mm, where the ICC algorithm diverged from the true coordinate by 5.0 mm in the x-axis and 1.0 mm in the y-axis. The average deviation between the true impact coordinates, and the coordinates that were calculated by the ICC algorithm during the ICC-1 experiments, was 2.8 mm.

For data visualisation purposes, the true impact coordinates were then plotted on the same figure as the impact coordinates that were calculated by the ICC algorithm.

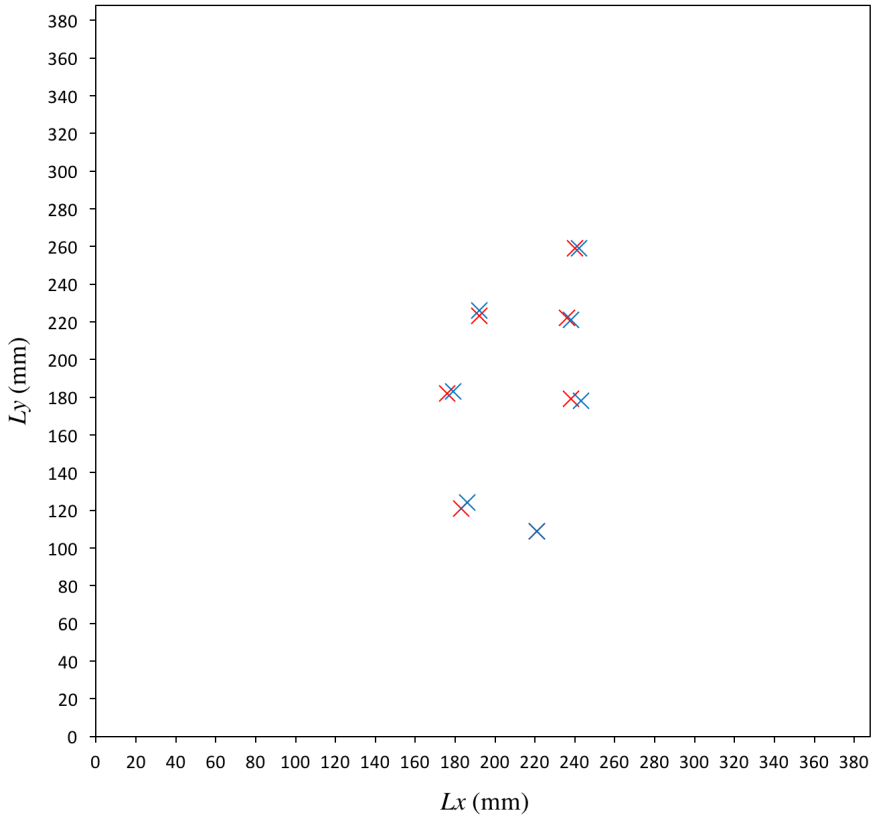

Figure 6.6: Graphical comparison between the measured impact coordinates (red) and the coordinates that were measured by the ICC algorithm (blue) in the ICC-1 experiments. L_x and L_y represent the distance between the PVDF sensors.

Figure 6.6 is a graphical representation of the ICC performance during the ICC-1 experiments. The x-axis and y-axis range was 0 – 388 and represents the distance between the PVDF sensors, in millimeters.

6.3.2 ICC-2 Results

Table 6.5 presents the true impact coordinates that were measured in the lab and the corresponding coordinates that were calculated by the ICC algorithm during the ICC-2 experiments.

The smallest deviation that was recorded during the ICC-2 experiments was 1.0 mm, where the ICC algorithm deviated from the true coordinates by 1.0 mm in either the

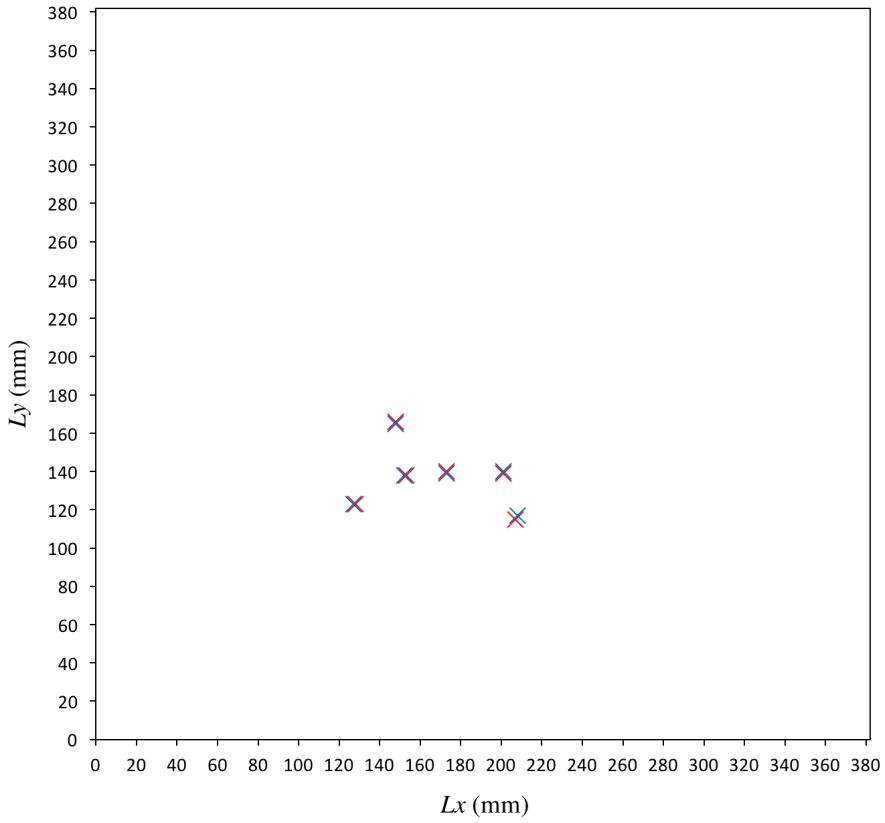

Figure 6.7: Graphical comparison between the measured impact coordinates (red) and the coordinates that were measured by the ICC algorithm (blue) in the ICC-2 experiments. L_x and L_y represent the distance between the PVDF sensors.

x-axis or y-axis, which is similar to the error in measuring the position of the impact hole (± 1.0 mm in ruler measurements discussed in Section 6.4). The largest deviation was recorded during ICC-2.02 and was 2.2 mm, where the ICC algorithm deviated from the true impact coordinates of the impact by 1.0 mm in the x-axis and 2.0 mm in the y-axis. The average deviation between true impact coordinates that were measured in the laboratory, and the coordinates that were calculated by the ICC algorithm during the ICC-2 experiments, was 1.2 mm. This is a significant improvement ($\sim$57 % more accurate) on the results that were recorded on the ODIN-Beta prototype in the ICC-1 experiments. The improvement is likely due to the higher quality frame used by the ODIN-2 prototype, which does not warp. Additionally, the rubber buffer between the Kapton and the frame created an acoustic impedence match, greatly reducing reflections.

Table 6.5: Data from the ICC-2 experiments, including the true coordinates (±1.0 mm), the coordinates calculated by the ICC and the deviation between them.

Experiment	True Coordinate (x, y, z)	ICS Coordinate (x, y, z)	Coordinate Deviation (mm)
ICC-2.01	(128, 123, 0)	(127, 123, 0)	1.0
ICC-2.02	(207, 115, 0)	(208, 117, 0)	2.2
ICC-2.03	(201, 139, 0)	(201, 140, 0)	1.0
ICC-2.04	(153, 138, 0)	(152, 138, 0)	1.0
ICC-2.05	(173, 140, 0)	(173, 139, 0)	1.0
ICC-2.06	(148, 166, 0)	(148, 165, 0)	1.0

The true impact coordinates measured in the laboratory were then plotted on the same graph as the impact coordinates that were calculated by the ICC algorithm. Figure 6.7 is a graphical representation of the ICC performance during the ICC-2 experiments. The x-axis and y-axis range between 0 – 382 and represents the distance between the PVDF sensors, in millimeters.

6.3.3 ICC-3 Results

Table 6.6 presents the true impact coordinates, on the primary IDG, that were measured in the laboratory and the corresponding coordinates that were calculated by the ICC algorithm during the ICC-3 experiments.

The smallest deviation that was recorded on the primary IDG during the ICC-3 experiments was 1.0 mm, where the ICC algorithm deviated from the true impact coordinates by 1.0 mm in the y-axis. The largest deviation was 2.0 mm, where the ICC algorithm deviated from the true impact coordinates of the impact by 2.0 mm in the y-axis. The average deviation between the true impact coordinates that were measured in the laboratory, and the coordinates that were calculated by the ICC algorithm during the ICC-3 experiments, was 1.5 mm. This is consistent with the deviations recorded on the primary IDG on the ODIN-2 prototype in the ICC-2 experiments.

Table 6.6: Primary IDG data from the ICC-3 experiments, including the true coordinates (±1.0 mm), the coordinates calculated by the ICC and the deviation between them.

Experiment	True Coordinate (x, y, z)	ICS Coordinate (x, y, z)	Coordinate Deviation (mm)
ICC-3.01	(227, 125, 0)	(227, 126, 0)	1.0
ICC-3.02	(166, 120, 0)	(166, 118, 0)	2.0
ICC-3.03	(256, 128, 0)	(257, 129, 0)	1.4
ICC-3.04	(276, 129, 0)	(275, 128, 0)	1.4
ICC-3.05	(117, 139, 0)	(115, 139, 0)	2.0
ICC-3.06	(158, 092, 0)	(158, 091, 0)	1.0
ICC-3.07	(067, 267, 0)	(065, 267, 0)	2.0
ICC-3.08	(164, 261, 0)	(164, 262, 0)	1.0

The true impact coordinates that were measured on the primary IDG in the laboratory were then plotted on the same graph as the impact coordinates that were calculated by the ICC algorithm. Figure 6.8 is a graphical representation of the ICC performance in the ICC-3 experiments. The x-axis and y-axis range between 0 – 382 and represents the distance between the PVDF sensors, in millimeters.

Table 6.7 presents the true impact coordinates, on the secondary IDG, that were measured in the laboratory and the corresponding coordinates that were calculated by the ICC algorithm during the ICC-3 experiments. It was important to demonstrate the accuracy of the ICC's ability to calculate the coordinates of impacts on the secondary IDG as they are subsequently used by the UVT and IGV subsystems. Prior to these experiments, it was unclear whether a particle's trajectory is altered, or whether the particle is disrupted, as it passes through the primary IDG. These are both factors that could affect the uncertainty of the ICC calculations on the secondary IDG.

The smallest deviation that was recorded on the secondary IDG during the ICC-3 experiments was 1.0 mm, where the ICC algorithm deviated from the true coordinates by 1.0 mm in either the x-axis or y-axis. The largest deviation was 3.2 mm, where the ICC algorithm deviated from the true impact coordinates by 1.0 mm in the x-axis or y-axis and 3.0 mm in the x-axis or y-axis. The average deviation between the

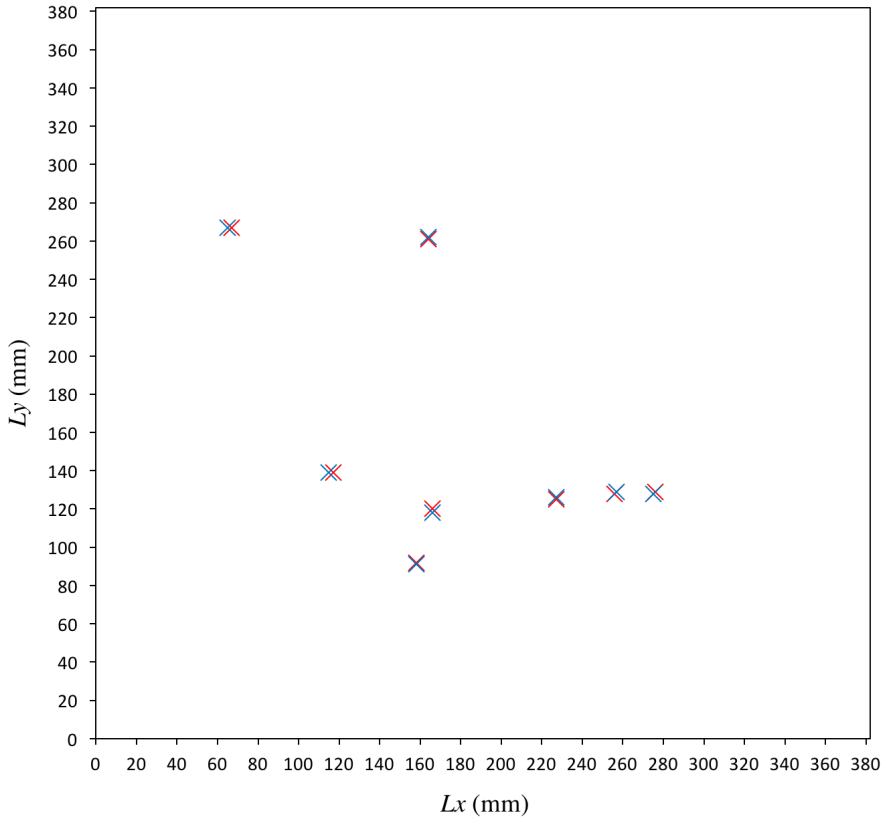

Figure 6.8: Graphical comparison between the measured impact coordinates (red) and the coordinates that were measured by the ICC algorithm (blue) on the primary IDG during the ICC-3 experiments. L_x and L_y represent the distance between the PVDF sensors.

Table 6.7: Secondary IDG data from the ICC-3 experiments, including the true coordinates (±1.0 mm), the coordinates calculated by the ICC and the deviation between them.

Experiment	True Coordinate (x, y, z)	ICS Coordinate (x, y, z)	Coordinate Deviation (mm)
ICC-3.01	(239, 129, 188)	(240, 132, 188)	3.2
ICC-3.02	(177, 122, 188)	(174, 121, 188)	3.2
ICC-3.03	(265, 132, 188)	(266, 132, 188)	1.0
ICC-3.04	(284, 132, 188)	(284, 133, 188)	1.0
ICC-3.05	(127, 144, 188)	(125, 143, 188)	2.2
ICC-3.06	(165, 096, 188)	(164, 095, 188)	1.4
ICC-3.07	(183, 264, 188)	(183, 265, 188)	1.0
ICC-3.08	(220, 265, 188)	(221, 268, 188)	3.2

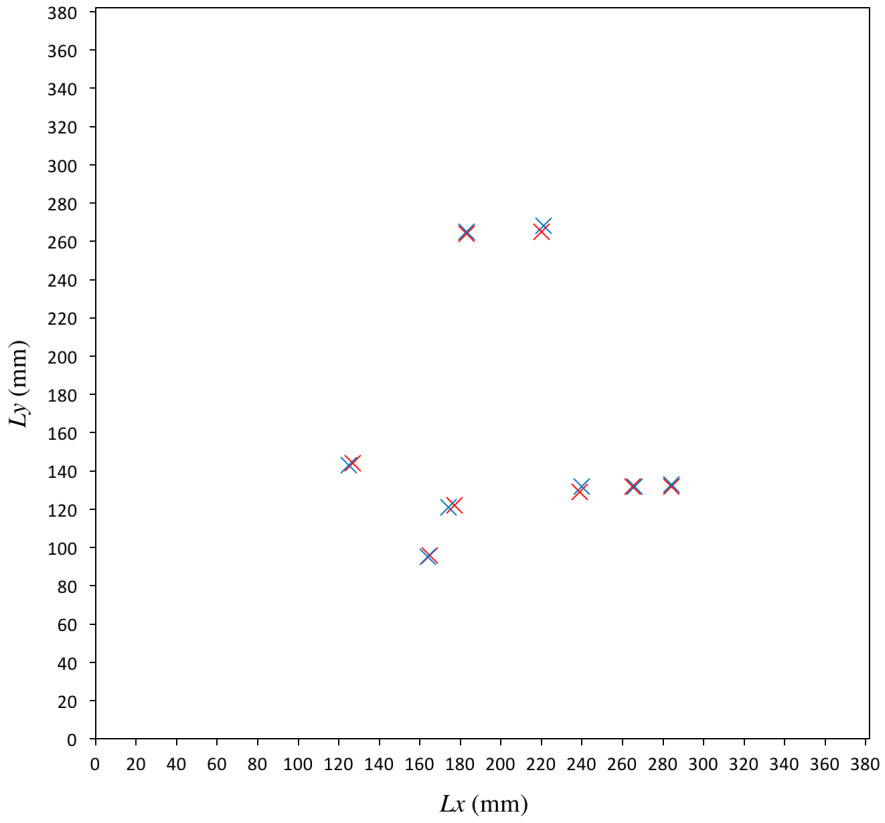

Figure 6.9: Graphical comparison between the measured impact coordinates (red) and the coordinates that were measured by the ICC algorithm (blue) on the secondary IDG during the ICC-3 experiments. L_x and L_y represent the distance between the PVDF sensors.

true impact coordinates that were measured in the laboratory, and the coordinates that were calculated by the ICC algorithm during the ICC-3 experiments, was 2.1 mm. This relatively low deviation demonstrates that there is no significant disruption of the particles as they pass through the primary IDG.

The impact coordinates that were measured on the secondary IDG in the laboratory were then plotted on the same graph as the impact coordinates that were calculated by the ICC algorithm (Figure 6.9).

6.4 Discussion

The first scientific objective of this research was to design and construct a detector that was capable of measuring the flux of OD/ID. The flux was calculated by counting the number of impacts that were recorded by the ICC and their time of impact, demonstrating the ICCs ability to measure the change in flux with respect to time. There was no significant uncertainty while measuring the flux, as each impact was profiled by four well defined acoustic signals (Figure 6.1) that only occur when a particle impacts the Kapton substrate on the primary IDG.

The flux measurements performed by the ICC relies on acoustic signals to record impacts. In order to differentiate one impact from another, there must be sufficient time between the impacts and their signals. If they occur in short succession, their acoustic signals can interfere with one another. The required time between impacts increases as they approach the corners of the primary IDG, due to the increasing distance that the signals must traverse before reaching the PVDF sensors. Hence, the flux-resolution of the ICC is dependent on the size of the detection area.

The diagonal distance between the PVDF sensors on the ODIN-2 prototype is $\sim$540 mm. This means the maximum time it could take an acoustic wave to traverse the primary IDG is $\sim$340 µs, assuming a constant wave-speed of 1.59 µm µs^{-1}. Hence, the flux-resolution of the ICC on ODIN-2 is appoximately 2940 impacts per second. This is high compared to the flux of particles encountered in LEO, which is approximately one particle ($d > 100$ µm) per square meter per day for high flux orbits, such as 800 km and 1500 km (Liou et al., 2002). The flux of ID, however, can be much higher during certain periods, such as meteor showers, or in other regions of the solar system. A dust jet emanating from the active side of Halley's nucleus caused DUCMA to experience flux as high as 4000 impacts per second (Simpson et al., 1986). In order to measure flux this high, a smaller detector, such as ODIN-Alpha that can measure approximately 7140 impacts per second, would be required.

In addition to the flux calculations, the ICC calculated the coordinates of impacts that occurred on the IDGs. This was important as impact locations are necessary for the calculations performed by the other subsystems. In general, the ICC calculated the coordinates of each projectile to a high degree of accuracy. The average deviation between the true coordinates of impacts on the primary IDG measured in the laboratory and those calculated by the ICC algorithm for the ICC-1, ICC-2 and ICC-3 experiments were $\pm 2.8\,\text{mm}$, $\pm 1.2\,\text{mm}$ and $\pm 1.5\,\text{mm}$, respectively. By comparison, current state-of-the-art detectors, such as the Space Debris Sensor (SDS) onboard the ISS, have an average deviation of $\pm 8\,\text{mm}$ (Hamilton et al., 2017). This level of uncertainty demonstrates the advantage of using the algorithmic method deployed by the ICC on ODIN, and how this method can improve the accuracy of the next generation of OD/ID detectors. It is noted that the detection area of the SDS is much larger than ODIN, at $1\,\text{m}^2$, which could possibly lead to higher uncertainties as the acoustic waves travel longer distances. However, the SDS acheives its large detection area by combining four smaller detectors positioned in a grid, so it is unlikely that the large detection area affects uncertainty in this case.

A number of systematic errors were encountered while performing the proof-of-concept experiments, and while analysing the data from the ICC, that are worth mentioning. First, there is a natural variation in the acoustic signal speed in Kapton. A speed of $1.59\,\text{mm}\,\mu\text{s}^{-1}$ was calculated from previous experiments, using known impact coordinates and time delays. This value, however, was averaged over many experiments and exhibited fluctuations depending on the signals direction of travel. It is unclear whether these variations were due to defects in the Kapton's manufacturing or other unknown obstructions, such as Kapton degradation from previous impact holes. Another consideration is the formation of a shock wave at the point of impact. At the typical impact speeds expected, shock pressures in the Kapton could exceed 10 GPa leading to the formation of shock wave. However, due to the small particle sizes and the thickness of the Kapton, this shockwave will decay to a stress wave within approximately $1\,\mu\text{s}$.

Additionally, random errors in a signal's arrival time can lead to uncertainties in the coordinates that are calculated by the ICC. Specifically, a deviation of 1.0 µs in the time delay calculations can lead to a 1.59 mm uncertainty in the coordinates. To account for this, the ICC is designed to calculate the coordinates for time delays with ±5.0 µs and average the results to get a single coordinate. Finally, random errors can occur during the measurement of the true impact coordinates, which are measured with a ruler and has an accuracy of ±1.0 mm. Additionally, some impact holes are larger than 1.0 mm, complicating measurements as the hole's centre is not always clear. These errors were reduced by taking averages from multiple coordinate measurements.

Systematic errors were also identified during the ICC data analysis that could potentially lead to uncertainties in the coordinates. These include deviations in the positioning of the PVDF sensors and the axis that links the detectors, which both have an uncertainty of ±1.0 mm. In an attempt to reduce these errors, a template was used while positioning the PVDF sensors during the construction of each prototype. Additionally, due diligence was taken while drawing the axis between the sensors to reduce systematic errors associated with the true coordinate measurements.

To conclude, the ICC subsystem demonstrated that it is capable of successfully measuring the flux of OD/ID particles with respect to time, and accurately measuring the coordinates of impacts on the IDGs. Taking all of the possible errors into account, an average impact deviation of 1.8 mm across all three sets of experiments was achieved, which is an improvement on current state-of-the-art.

Chapter 7

Unit Vector Trajectory Subsystem

The Unit Vector Trajectory (UVT) subsystem uses the impact coordinates on the primary and secondary IDGs to calculate the trajectory of OD/ID as a three dimensional unit vector, which can easily be converted into angles, and thus a trajectory. An understanding of OD/ID trajectories can be used in risk assessments (Christiansen and Kerr, 1993) and provides information regarding the origin of ID, when combined with the precise orbital details and orientation of the host spacecraft (Hörz, 1986). A four-step process is performed by the UVT to calculate the trajectory of OD/ID passing through the detector. The four steps are as follows:

1. Determine the impact coordinates on the primary and secondary IDGs.
2. Calculate the vector between the corresponding impact coordinates on the primary and secondary IDGs.
3. Calculate the magnitude of the vector.
4. Calculate the unit vector.

7.1 Impact Coordinates

The first step in the process involves finding accurate three dimensional impact coordinates on the primary and secondary IDGs. This process is performed by the ICC and was discussed in Chapter 6. The primary IDG is located at $z = 0\,\text{mm}$ and the secondary IDG is located at $z = 188\,\text{mm}$ and $z = 145\,\text{mm}$ on the ODIN-2 and ODIN-3 prototypes, respectively. The impact coordinates on the IDG planes are represented by the x and y coordinates. Figure 7.1 shows how the primary and secondary IDGs fit into the three dimensional cartesian coordinate system.

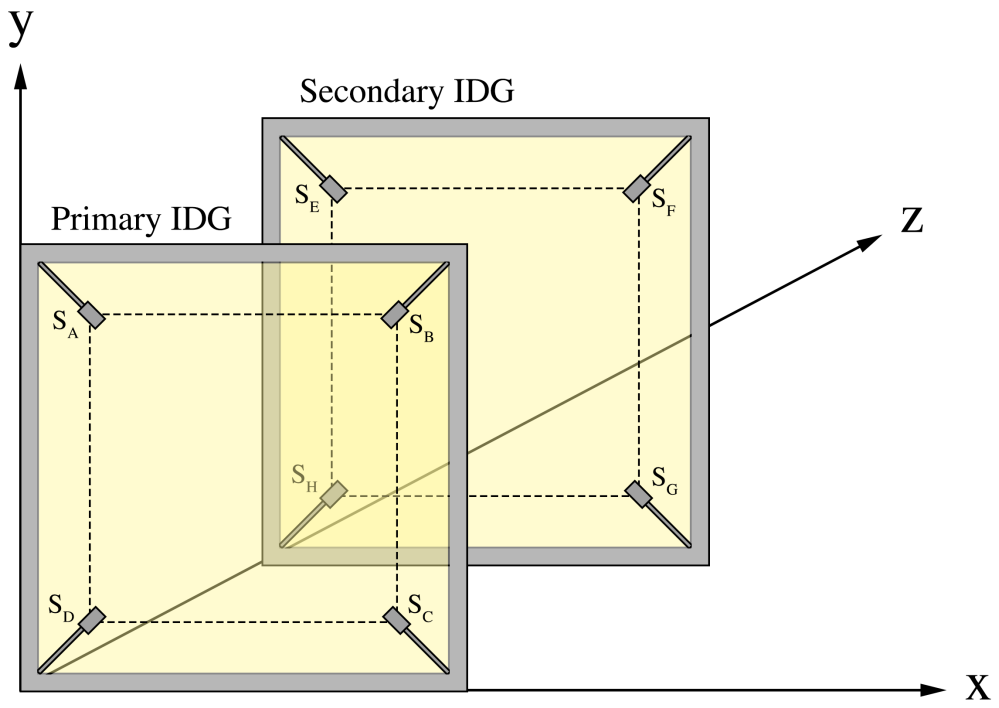

Figure 7.1: Schematic of the primary and secondary IDGs in the three dimensional Cartesian coordinate system.

7.2 Trajectory Vector

The second step in the process involves calculating the vector between the corresponding impacts on the primary and secondary IDGs, known as the primary and secondary impacts, respectively. The ICC and UVT use a Cartesian coordinate system, which means the path between the primary and secondary impacts can be represented by a vector, $\overrightarrow{\boldsymbol{v}}$, with components $\hat{\boldsymbol{\imath}}$, $\hat{\boldsymbol{\jmath}}$ and $\hat{\boldsymbol{k}}$.

$$\overrightarrow{\boldsymbol{v}} = \Delta x\hat{\boldsymbol{\imath}} + \Delta y\hat{\boldsymbol{\jmath}} + \Delta z\hat{\boldsymbol{k}} \tag{7.1}$$

Where Δx, Δy and Δz represent the magnitude in the $\hat{\boldsymbol{\imath}}$, $\hat{\boldsymbol{\jmath}}$ and $\hat{\boldsymbol{k}}$ directions respectively. To find the value of Δx, Δy and Δz, the primary impact coordinates, (x_p, y_p, z_p), are subtracted from the secondary impact coordinates, (x_s, y_s, z_s).

$$\Delta x = x_s - x_p \tag{7.2}$$

$$\Delta y = y_s - y_p \tag{7.3}$$

$$\Delta z = z_s - z_p \tag{7.4}$$

7.3 Trajectory Vector Magnitude

The third step in the process involves calculating the magnitude, $|\overrightarrow{\boldsymbol{v}}|$, of the vector, which represents the distance between the primary and secondary impacts. The UVT uses the magnitude to calculate the unit vector, $\hat{\boldsymbol{v}}$, of the vector. Equation 7.5 is used in a Python script to calculate the magnitude of the vector, $|\overrightarrow{\boldsymbol{v}}|$.

$$|\overrightarrow{\boldsymbol{v}}| = \sqrt{\Delta x^2 + \Delta y^2 + \Delta z^2} \tag{7.5}$$

In addition to the unit vector calculations, the magnitude of the trajectory vectors are used (Chapter 8) to find the velocity of OD/ID particles.

7.4 Unit Vector

The fourth and final step in the process involves finding the unit vector of the trajectory. To calculate a unit vector, the x, y and z components of the vector are divided by the magnitude of the vector.

$$\hat{\boldsymbol{v}} = \frac{\overrightarrow{\boldsymbol{v}}}{|\overrightarrow{\boldsymbol{v}}|} = \frac{\Delta x\hat{\boldsymbol{i}} + \Delta y\hat{\boldsymbol{j}} + \Delta z\hat{\boldsymbol{k}}}{\sqrt{\Delta x^2 + \Delta y^2 + \Delta z^2}} \tag{7.6}$$

Unit vectors can be used to find the flight trajectory angle (°) in the x and y axis using Equation 7.7 and Equation 7.8 below. Where θ and ϕ represent the angles in the x and y axis respectively (Figure 7.2).

$$\theta = tan^{-1}\Big(\frac{\Delta x}{\Delta z}\Big) \tag{7.7}$$

$$\phi = tan^{-1}\Big(\frac{\Delta y}{\Delta z}\Big) \tag{7.8}$$

Figure 7.2 is a graphical representation of θ and ϕ, where z represents the direction of travel for a projectile with an impact angle normal to the primary IDG.

7.5 UVT Proof of Concept

A set of experiments were carried out to simulate OD/ID impacts with the ODIN-2 prototype so that the performance of the UVT could be assessed under test conditions. The process was as follows:

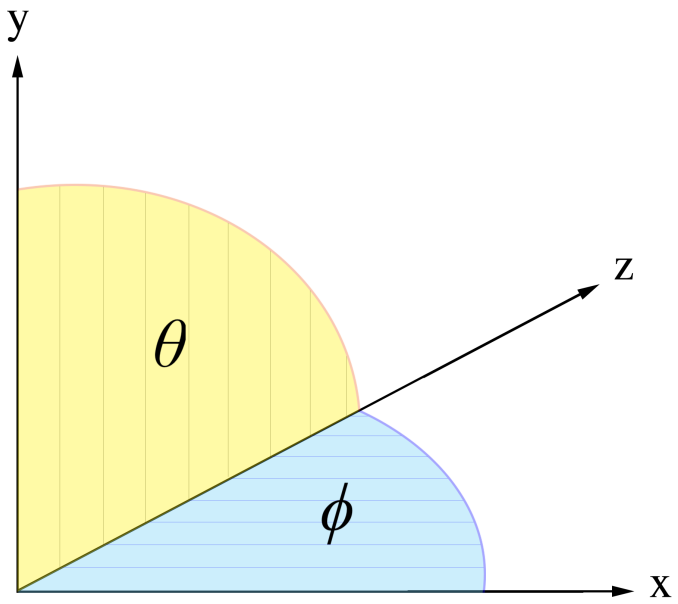

Figure 7.2: Schematic showing theta θ and phi ϕ in the three dimensional Cartesian coordinate system.

1. Simulate OD/ID impacts with the ODIN-2 prototype.
2. Run the ICC algorithm to calculate the impact coordinates on the primary and secondary IDGs.
3. Run the UVT algorithm to calculate the trajectory unit vector of each projectile.
4. Compare the calculated trajectories with the actual trajectories.

7.5.1 Simulating OD/ID Impacts

The ODIN-2 prototype was placed under a vacuum (50 mbar) in the impact chamber of the LGG. Projectiles were then accelerated towards the prototype at different angles of incidence. The acoustic responses to the subsequent impacts were recorded by the PVDF sensors and saved to a computer. The acoustic data were then processed by the ICC algorithm so that the impact coordinates could be calculated, and then the UVT algorithm was run to calculate the different angles of incidence.

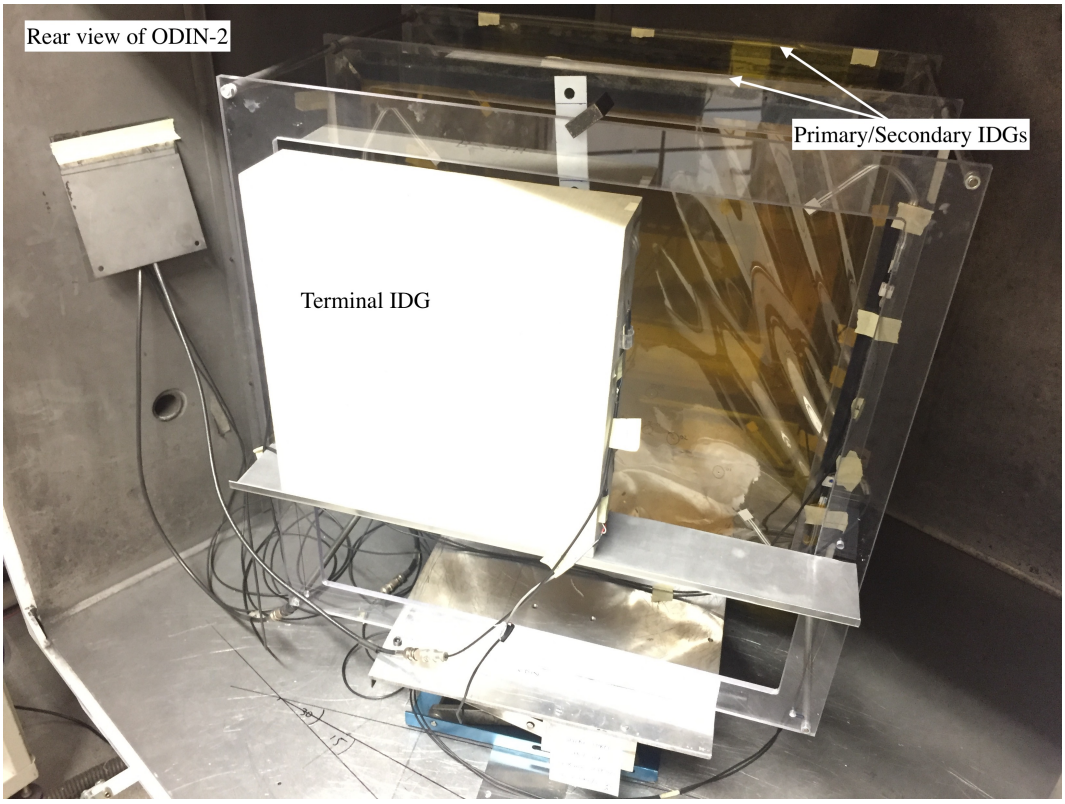

Figure 7.3: Photograph of the ODIN-2 prototype in the target chamber at an angle of 30° from the normal.

Spherical stainless steel projectiles were used throughout the UVT proof-of-concept experiments. Helium gas at 90.0 bar was used when accelerating the projectiles to $\sim$3.0 kms^{-1} and hydrogen gas at 45.0 bar was when accelerating the projectiles to $\sim$5.0 kms^{-1}. The projectiles used in the UVT proof-of-concept experiments all had diameters of 0.8 mm. To create different impact angles, ODIN-2 was positioned in the impact chamber at 0.0°, 15.0° and 30.0° to the projectile's line-of-flight (Figure 7.3).

7.5.2 UVT-1 Experiments

The UVT-1 experiments included three impacts with the ODIN-2 prototype. Only three experiments were conducted during the UVT proof-of-concept because the UVT is an algorithmic subsystem that processes coordinates that are recorded by the ICC, which has demonstrated its reliability and accuracy (Chapter 6).

Table 7.1: Data from the UVT-1 experiments, including the diameter, velocity (±1.0 %) and incident angle of the projectiles (±1.0°).

Experiment	Diameter (mm)	Velocity (kms^{-1})	Incident Angle (°)
UVT-1.01	0.8	2.93	0.0
UVT-1.02	0.8	4.99	30.0
UVT-1.03	0.8	5.00	15.0

For the ODIN-2 prototype, the average deviation between the true impact coordinate and those calculated by the ICC was 1.4 mm. Hence, the UVT proof-of-concept was only used to test the UVT algorithm and expose any bugs. Full details of the UVT-1 experiments can be found in Table 7.1.

7.6 UVT Results

After each experiment, the ICC algorithm calculated the impact coordinates on the primary and secondary IDGs. The UVT algorithm was then used to calculate the trajectory of each projectile as a unit vector, which was then converted into an angle relative to the normal, and compared with the actual experimental trajectory of each projectile. This process provided a means to assess the accuracy of the UVT.

The unit vector of each projectile was converted into an angle from the normal so that it could be compared with the experimental trajectory of each projectile. Table 7.2 presents a comparison between the experimental trajectory of each projectile, in the x-axis, and the trajectory that was calculated by the UVT. The uncertainty between the experimental and calculated trajectories is also included.

Table 7.2: Results from the UVT-1 experiments, including the experimental impact angle and the angle of incidence that was calculated by the UVT algorithm.

Experiment	Incident Angle (°)	UVT Incident Angle (°)	Uncertainty (±°)
UVT-1.01	0.0	0.3	0.3
UVT-1.02	30.0	29.7	0.3
UVT-1.03	15.0	14.5	0.5

The lowest uncertainty that was recorded during the UVT-1 experiments was 0.3° and the highest uncertainty was 0.5°. The average uncertainty was 0.37°.

7.7 Discussion

The second scientific objective of this research was to design and construct a detector capable of measuring the trajectory of OD/ID. The trajectories of OD/ID particles were calculated using impact Cartesean coordinates across the primary and secondary IDGs and demonstrated the ability of the UVT subsystem.

The maximum angle of trajectory that the UVT can calculate depends on the distance between the PVDF sensors, and the standoff between the primary and secondary IDGs. The PVDF sensors on the ODIN-2 prototype have a separation of 382 mm and a standoff of 188 mm, which translates to a maximum trajectory of 63.8° from the normal. The average uncertainty across the three experiments was 0.37°, which translates to an average percentage uncertainty of 0.58 % between the true trajectory and that calculated by the UVT. Assuming an uncertainty of ±2.0 mm in the ICC calculations, an approximate maximum error of 1.2° could be expected.

During the UVT proof-of-concept experiments, a possible random error was identified while positioning the prototype in the impact chamber. Although due diligence was taken to position ODIN-2 at precisely 0.0°, 15.0° and 30.0°, it must be noted that small errors (∼1.0°) may have been present.

Additionally, a number of systematic errors were identified during the proof-of-concept experiments. An error of ∼2.7° was recorded throughout the trajectory results, which was not due to algorithmic or mathematical errors. An investigation showed that the PVDF sensors on the secondary IDG were positioned, −8.0 mm on the x-axis, and −2.0 mm on the y-axis, relative to the PVDF sensors on the primary IDG. The discrepancy was corrected by subtracting 8.0 mm and 2.0 mm from the x and y

coordinates, respectively, on the secondary IDG. This illustrates the importance of knowing the relative positions of all the PVDF sensors as accurately as possible.

The HRD onboard the Cassini spacecraft and the SDS are two examples of detectors capable of measuring the trajectory of OD/ID particles. According to Hamilton et al. (2017), the SDS has an average uncertainty of $\pm 3.0^{\circ}$, with some uncertainties as high as $\sim 17.0^{\circ}$. The accuracy of the UVT on ODIN is $\pm 0.37^{\circ}$, an order of magnitude better than the SDS and a significant advancement, which demonstrates the benefit of using the UVT on ODIN to calculate the trajectory of OD/ID. This improvement is likely due to the algorithmic nature of the ICC coordinate calculations that feed into the UVT. Additionally, the resistive grid that is adhered to the Kapton on the SDS could be affecting the acoustic signals which, in turn, affect the accuracy of the coordinates and trajectories recorded by the SDS. Finally, it is acknowledged that the projectiles used in the proof-of-concept experiments are ideal, spherical, non-porous projectiles and in-flight accuracy may be reduced for less uniform particles.

Chapter 8

Impact Gate Velocity Subsystem

The Impact Gate Velocity (IGV) subsystem is the subsystem onboard ODIN that measures the speed of OD/ID particles. It uses the coordinates and time-of-impact of particles perforating the primary and secondary IDGs. A three step process is used by the IGV to calculate the speed of OD/ID dust. The three steps are as follows:

1. Calculate the time-of-flight between the primary and secondary IDGs.
2. Determine the distance between corresponding primary and secondary impacts.
3. Calculate the speed of OD/ID dust using the distance and time-of-flight between the primary and secondary IDGs.

8.1 Time-of-Flight

The first step in the process involves finding the time-of-flight between the primary and secondary IDGs. This is calculated by subtracting the impact time on the primary IDG from the corresponding impact time on the secondary IDG. In order to calculate the time-of-impact, the distance (d_A, d_B, d_C and d_D) between the impact and each of the PVDF sensors must be calculated. This is done using the impact coordinates

calculated by the ICC. The mathematics of calculating the distance between the impact and each sensor was presented in Equations 6.5 – 6.8 in Chapter 6.

The travel time (T_A, T_B, T_C and T_D) for an acoustic signal to traverse the distance between the impact location and each sensor can be calculated using the speed of sound in Kapton. The mathematics for calculating the signal's travel time to each sensor was presentedin Equations 6.9 – 6.12 in Chapter 6.

The time-of-impact is calculated by subtracting the signal travel time from the signal arrival time.

$$t_{I(A)} = t_A - T_A \tag{8.1}$$

$$t_{I(B)} = t_B - T_B \tag{8.2}$$

$$t_{I(C)} = t_C - T_C \tag{8.3}$$

$$t_{I(D)} = t_D - T_D \tag{8.4}$$

Where t_I (µs) is the time-of-impact and t (µs) is the signal arrival time recorded by each sensor. The subscripts A, B, C and D, represent the different sensors. In an ideal situation, $t_{I(A)} = t_{I(B)} = t_{I(C)} = t_{I(D)}$, however, in practice this is not always the case. To increase the accuracy of the time-of-flight calculations, the impact times are averaged, see Equation 8.5.

$$t_I = \frac{t_{I(A)} + t_{I(B)} + t_{I(C)} + t_{I(D)}}{4} \tag{8.5}$$

This process is then repeated to find the time-of-impact on the secondary IDG. The difference between the two impact times is then used to determine the time-of-flight between the primary and secondary IDGs. Equation 8.6 shows the time-of-flight calculation.

$$t_{P-S} = t_{I(S)} - t_{I(P)} \tag{8.6}$$

Where t_{P-S} (µs) is the time-of-flight between the primary and secondary IDGs and t_I (µs) is the average time-of-impact on each IDG, where the subscripts P and S represent the primary IDG and secondary IDG, respectively.

8.2 Flight Distance

The second step in the process involves calculating the distance between the impact on the primary IDG and the corresponding impact on the secondary IDG. It is a relatively quick process, as the IGV can use the magnitude of the trajectory vector, calculated by the UVT subsystem, detailed in Chapter 7. The magnitude of the trajectory vector gives the distance between the primary and secondary impacts.

$$d_{p-s} = |\overrightarrow{\boldsymbol{v}}| = \sqrt{\Delta x^2 + \Delta y^2 + \Delta z^2} \tag{8.7}$$

Where $|\overrightarrow{\boldsymbol{v}}|$ is the magnitude of the flight vector, d_{p-s} (mm) is the distance between the primary and secondary impacts and Δx, Δy and Δz represent the difference between the primary and secondary impact coordinates.

8.3 Speed

The third, and final, step in the process involves calculating the speed of OD/ID particles passing through the detector. The speed of the particles is calculated by dividing the flight distance by the time-of-flight.

$$s_d = \frac{d_{p-s}}{t_{p-s}} \tag{8.8}$$

Where s_d ($\mathrm{km\,s^{-1}}$) is the speed of the debris, d_{p-s} (mm) is the distance of flight and t_{p-s} (µs) is the time-of-flight between the primary and secondary IDG.

8.4 IGV Proof-of-Concept

A set of experiments were designed to simulate OD/ID impacts with the ODIN-2 prototype so that the performance of the IGV could be assessed under test conditions. The process was as follows:

1. Simulate OD/ID impacts with the ODIN-2 prototype.
2. Run the ICC algorithm to calculate the impact coordinates of each projectile.
3. Run the IGV algorithm to calculate the speed of each projectile.
4. Compare the speed that was calculated by the IGV with the true speed measured using the LGG's time-of-flight (ToF) system (accurate to $\sim$1.0 %).

8.4.1 Simulating OD/ID Impacts

The ODIN-2 prototype was placed under a vacuum in the impact chamber of the LGG. Projectiles were then accelerated towards ODIN-2 at different velocities, comparable with OD/ID, and the acoustic response to each of the subsequent impacts was recorded by the PVDF sensors. The acoustic data were then processed by the ICC algorithm so that the impact coordinates could be calculated. The IGV algorithm was then run to calculate the velocity of each projectile.

Spherical stainless steel projectiles, diameters ranging between 0.3 mm and 1.5 mm, were used throughout the IGV proof-of-concept experiments, and accelerated to velocities between $\sim$3.0 kms^{-1} and $\sim$5.0 kms^{-1}. To create different impact angles, ODIN-2 was placed in the impact chamber at 0.0°, 15.0° and 30.0° to the projectile's line-of-flight.

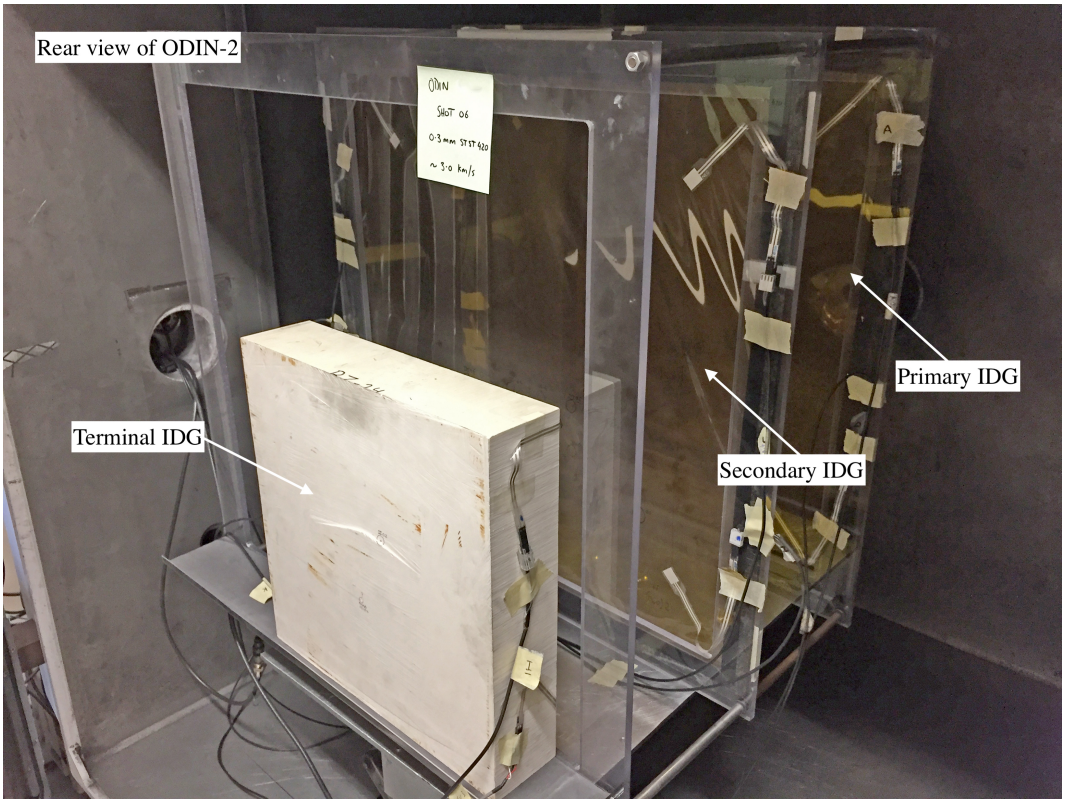

Figure 8.1: Photograph of the ODIN-2 prototype in the target chamber during one of the IGV-1 experiments.

8.4.2 IGV-1 Experiments

The IGV-1 experiments included eight impacts with the ODIN-2 prototype. Only one set of experiments were conducted during the IGV proof-of-concept phase because the IGV is an algorithmic subsystem, like the UVT, and processes data that are recorded by the ICC. Hence, the experiments were only used to check the mathematics and logic of the IGV algorithm, and expose any unforeseen errors or uncertainties. Full details of the IGV-1 experiments can be found in Table 8.1.

Table 8.1: Details of the IGV-1 experiments, including the diameter, velocity (measured by the LGG's ToF system to ±1.0 %) and incident angle of the projectiles (±1.0°).

Experiment	Diameter (mm)	True Velocity (kms^{-1})	Incident Angle (°)
IGV-1.01	1.0	4.61	0.0
IGV-1.02	1.5	3.16	0.0
IGV-1.03	1.0	2.97	0.0
IGV-1.04	0.8	2.93	0.0
IGV-1.05	0.5	3.09	0.0
IGV-1.06	0.3	3.04	0.0
IGV-1.07	0.8	4.99	30.0
IGV-1.08	0.8	4.88	15.0

8.5 IGV Results

After each experiment, the ICC algorithm calculated the impact coordinates on the primary and secondary IDGs. The IGV algorithm then calculated the speed of each projectile as it passed through the detector, and compared it with the true speed of each projectile, as measured by the LGG's ToF system.

Table 8.2 presents a comparison between the speed of projectiles that were calculated by the IGV and the true speed of the projectiles, during each experiment, and also includes the percentage uncertainty of the results.

Table 8.2: Results of the IGV-1 experiments, including the true speed of projectiles (±0.1 %), the speed that was calculated by the IGV and the percentage uncertainty of the results.

Experiment	Actual Velocity (kms^{-1})	IGVS Velocity (kms^{-1})	Uncertainty (%)
IGV-1.01	4.61	4.32	6.4
IGV-1.02	3.16	3.08	2.6
IGV-1.03	2.97	2.85	4.1
IGV-1.04	2.93	2.75	6.1
IGV-1.05	3.09	2.97	3.8
IGV-1.06	3.04	2.94	3.3
IGV-1.07	4.99	4.92	1.5
IGV-1.08	4.88	4.68	4.1

The lowest percentage uncertainty that was recorded during the IGV-1 experiments was 1.5 % and the highest percentage uncertainty was 6.4 %. The average percentage uncertainty that was recorded during the IGV-1 experiments was 4.0 %. The true velocities that were calculated by the LGG's ToF system are accurate to within 1.0 %.

8.6 Discussion

The third scientific goal of this research was to design and construct a detector that was capable of measuring the velocity of OD/ID. It did this by using the time-of-flight, and distance, between corresponding impacts on the primary and secondary IDGs. The proof-of-concept experiments clearly demonstrated the ability of the IGV subsystem to accurately measure velocity.

A number of systematic errors were identified during the proof-of-concept experiments and data analysis. The difference between the pre-impact light gate (true) velocity (calculated by the LGG's ToF system) and the velocity that was calculated by the IGV, may be the result of particles slowing down during their passage through the primary IDG. Typically, experimental data exhibits plus/minus uncertainties. However, all of the velocities calculated by the IGV are, on average, 4.0 % slower than the pre impact light gate velocities, which indicates that the projectiles were being slowed down by the primary IDG, if only slightly.

Additionally, small uncertainties in the standoff between the primary and secondary IDGs can have a relatively large effect on the velocities calculated by the IGV. In fact, a 2.0 mm uncertainty in the standoff, can lead to a $\sim$1 % deviation between the true velocity, and that calculated by the IGV. This illustrates the importance of precise detector construction.

The average percentage uncertainty, across the eight IGV proof-of-concept experiments, was 4.0 %, which translates to an error of approximately 150 $\mathrm{m\,s^{-1}}$ and appeared to be unaffected by impact angle, velocity or impactor size. According to Hamilton

et al. (2017), the SDS has an average uncertainty of 18 %, with the majority of velocities being correct to within $\pm 1.0\,\mathrm{km\,s^{-1}}$. This demonstrates the advantage of using an algorithmic analysis technique, such as that used by the IGV on ODIN, to calculate the velocity of OD/ID particles. The upper limit of the IGV velocity calculations is difficult to calculate, however, assuming an accuracy of $\pm 2\,\mu\mathrm{s}$ in the impact-time measurements and precise standoff distances, the IGV could expect to have an upper limit of $\sim 50\,\mathrm{km\,s^{-1}}$.

Chapter 9

Peak-Trough Diameter Subsystem

The Peak-Trough Diameter (PTD) subsystem is the subsystem onboard ODIN that measures the size of OD/ID. It uses the peak-trough (PT) amplitude of acoustic signals acquired by the PVDF sensors on the primary IDG. A five-step process is used by the PTD to calculate the diameter of OD/ID dust. The five steps are as follows:

1. Determine the distance from the impact coordinate to each sensor.
2. Calculate the acoustic PT amplitude recorded by each sensor.
3. Calculate the normalised acoustic PT amplitude recorded by each sensor.
4. Average the four normalised acoustic PT amplitudes.
5. Calculate the diameter of OD/ID from a calibration plot.

9.1 Impact-Sensor Distance

The first step in the process involves finding the distance from the impact on the primary IDG to each of the four PVDF sensors. This process uses the impact coordinates, which

are calculated by the ICC. The distance between the impact and each sensor is then calculated using the Pythagorean equations (6.5 – 6.8) described in Chapter 6.

9.2 Peak-Trough (PT) Amplitude

The second step in the process involves calculating the PT amplitude of the acoustic signals recorded by each sensor. PT amplitude is the difference between the peak (highest amplitude value) and the trough (lowest amplitude value). Figure 9.1 is a graphical example of the PT amplitude of a typical acoustic signal recorded by a PVDF sensor on the Kapton substrate.

A Python script was used to analyse the data and record the voltage at the maximum peak and minimum trough for the acoustic signals recorded by each sensor and then calculated the difference between these two values. The output is a single PT amplitude value for each of the PVDF sensors.

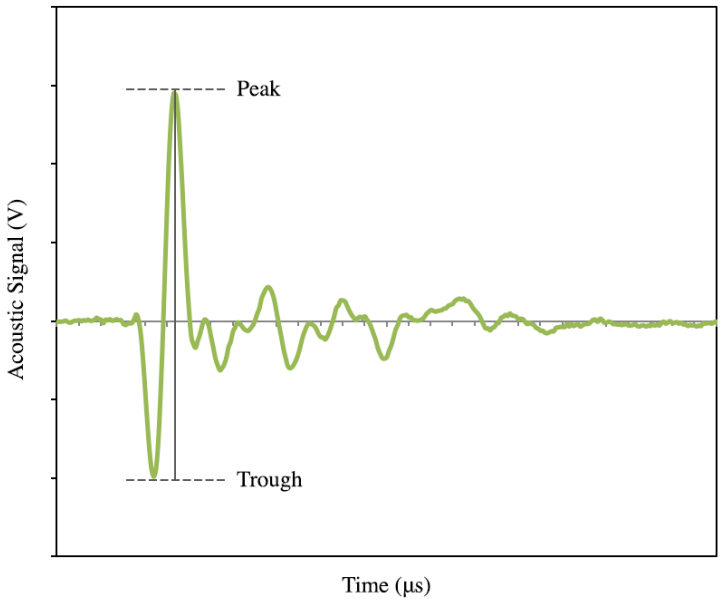

Figure 9.1: A graphical example of PT amplitude of an acoustic signal recorded by a PVDF sensor on the primary IDG.

9.3 Normalising Peak-Trough Amplitude

There are two variables that affect the PT amplitude; (1) the size of OD/ID impacting the IDG, and (2) the distance from the impact to the sensor. It is worth mentioning that impact speed can also affect the PT amplitude. Amplitude increases with OD/ID diameter, and decreases with distance from the impact site. The speed of OD/ID is calculated by the IGV and can therefore be removed from the equation. Hence, the third step in the process involves normalising the PT amplitude values that were calculated in step two.

For an acoustic signal radiating from a point, the energy transmitted by the wave is proportional to the amplitude of the wave squared, multiplied by the circumference of the wavefront.

$$E \propto A^2 \, 2\pi \, d \tag{9.1}$$

Where A (V) is the amplitude recorded by a PVDF sensor at a distance, d (mm), from the sensor. The amplitude of an impact at a distance, d (mm), from a sensor can be normalised by equating it to the amplitude of an impact at a nominal distance - in this case 250 mm. The normalised distance does not have to be 250 mm, but was the distance chosen in this study as it is half the nominal distance (500 mm) between the sensors. Therefore, Equation 9.1 can be modified to:

$$A_{250}^2 \, 2\pi \, 250 = A^2 \, 2\pi \, d \tag{9.2}$$

Where A_{250} (V) is the amplitude of the wave at a distance of 250 mm from the impact site to the sensor. Hence, a simple rearrangement can be performed to convert the amplitude at a distance, d (mm), from an impact site to a normalised amplitude, A_{250} (V), at a distance of 250 mm.

$$A_{250} = A \sqrt{\frac{d}{250}} \tag{9.3}$$

A Python script substitutes the PT amplitude, A (V), and distance, D (mm), recorded in step one and two into Equation 9.3. This process is repeated for data from each of the four PVDF sensors on the primary IDG, outputting four normalised PT amplitude values.

9.4 Normalised Peak-Trough Averaging

The fourth step in the process involves averaging the four normalised PT amplitude values that were calculated in step three. In theory, any one of the normalised PT values should permit extrapolation of OD/ID diameters, as the normalised PT amplitude should be identical for each sensor. However, averaging the four values increases the accuracy by reducing random errors.

$$A_{NPT} = \frac{A_{NA} + A_{NB} + A_{NC} + A_{ND}}{4} \tag{9.4}$$

Where A_{NPT} (V) is the average normalised PT amplitude and A_{NA}, A_{NB}, A_{NC} and A_{ND} are the normalised PT amplitudes recorded by each sensor.

9.5 Diameter Calibration

The fifth step in the process determines the diameter of OD/ID dust particles passing through the primary IDG. If a correlation exists between the diameter of OD/ID and the PT amplitude that is recorded by the PVDF sensors, it can be used to approximate the diameter of the dust particles, assuming the PT amplitude is known. Specifically, the diameter could be calculated using pre-determined plots of diameter against PT amplitude created from calibration experiments. Figure 9.2 shows an example of what a calibration plot might look like.

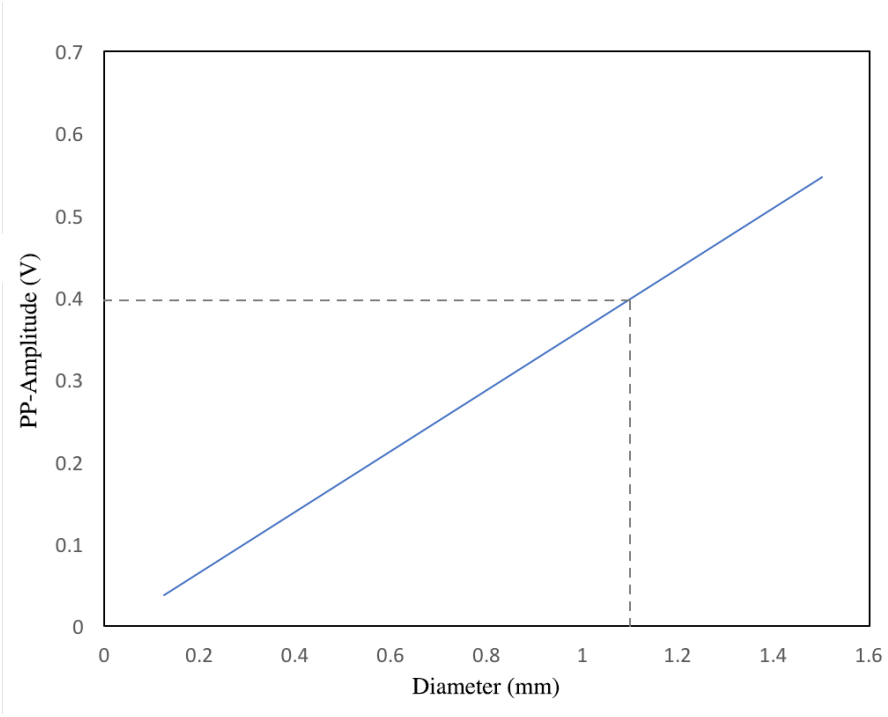

Figure 9.2: A graphical example of a PT amplitude against debris diameter calibration plot. Note: not real data.

9.6 PTD Proof-of-Concept

Three sets of experiments were designed to simulate OD/ID impacts with the ODIN-Beta and ODIN-2 prototypes so that a correlation between the diameter and PT amplitude could be established, leading to the creation of calibration plots. The calibration plots were then used to assess the performance of the PTD under test conditions. The process was as follows:

1. Experimentally simulate OD/ID impacts with prototypes of the detector.
2. Create calibration plots for PT amplitude against projectile diameter.
3. Compare calibrated diameters with the true diameter of the projectiles measured in the lab.

9.6.1 Simulating OD/ID Impacts

As with the previous proof-of-concept experiments, OD/ID impacts were simulated using the LGG. The acoustic data were then processed by the ICC algorithm so that the impact coordinates could be calculated. The PTD algorithm was then run to calculate the PT amplitude for each impact. The ODIN-Beta and ODIN-2 prototypes were used during the PTD proof-of-concept experiments.

Spherical stainless steel projectiles, with diameters ranging between 0.1 mm and 2.0 mm, were accelerated to $\sim$3.0 kms^{-1} and $\sim$5.0 kms^{-1}. Details of the three sets of experiments conducted for the PTD proof-of-concept procedure are presented below.

9.6.2 PTD-1 Experiments

The first set of experiments, PTD-1, included seven impacts with the ODIN-beta prototype. Spherical stainless steel projectiles with diameters ranging from 0.3 mm to 2.0 mm were accelerated to $\sim$5.0 kms^{-1} with an incident impact angle of 0.0°. Full details of these experiments can be found in Table 9.1.

Table 9.1: Data from the PTD-1 experiments, including the diameter and velocity ($\pm$1.0 %). An impact angle of 0.0° ($\pm$1.0°) was used during each experiment.

Experiment	Diameter (mm)	Velocity (kms^{-1})
PTD-1.01	0.3	4.47
PTD-1.02	0.4	5.08
PTD-1.03	0.5	5.05
PTD-1.04	0.8	5.04
PTD-1.05	1.0	4.90
PTD-1.06	1.5	5.04
PTD-1.07	2.0	5.00

9.6.3 PTD-2 Experiments

The second set of experiments, PTD-2, included nine impacts with the primary IDG of the ODIN-2 prototype. Spherical stainless steel projectiles with diameters ranging from 0.1 mm to 1.0 mm were accelerated to ∼5.0 kms^{-1} with incident impact angles of 0.0°, 15.0° and 30.0°. It was important to include experiments with a variety of impact angles to investigate the affect this had on the PT amplitude. Full details of these experiments can be found in Table 9.2.

Table 9.2: Data from the PTD-2 experiments, including the diameter, velocity (±1.0 %) and incident angle (±1.0°) of each projectile.

Experiment	Diameter (mm)	Velocity (kms^{-1})	Incident Angle (°)
PTD-2.01	0.1	5.07	0.0
PTD-2.02	0.3	5.25	0.0
PTD-2.03	0.4	5.17	0.0
PTD-2.04	0.5	5.31	0.0
PTD-2.05	0.8	4.93	0.0
PTD-2.06	1.0	4.93	0.0
PTD-2.07	1.0	4.61	0.0
PTD-2.08	0.8	4.99	30.0
PTD-2.09	0.8	5.00	15.0

9.6.4 PTD-3 Experiments

The third set of experiments, PTD-3, included five impacts with the primary IDG of the ODIN-2 prototype. Spherical stainless steel projectiles with diameters ranging from 0.3 mm - 1.5 mm were accelerated to speeds of ∼3.0 kms^{-1} with an incident impact angle of 0.0°. It was important to repeat the experiments conducted on the ODIN-2 prototype with different impact velocities to investigate the affect this had on the PT amplitude. Full details of these experiments can be found in Table 9.3.

Table 9.3: Data from the PTD-3 experiments, including the diameter and velocity (±1.0 %). An impact angle of 0.0° (±1.0°) was used during each experiment.

Experiment	Diameter (mm)	Velocity (kms^{-1})
PTD-3.1	0.3	3.04
PTD-3.2	0.5	3.09
PTD-3.3	0.8	2.93
PTD-3.4	1.0	2.97
PTD-3.5	1.5	3.16

9.7 PTD Results

During each set of experiments, the PTD recorded the PT amplitude of each impact, which was then plotted against the true projectile diameter. A trend line was added to each plot, which was used as the calibration plot. The diameter of each projectile was then approximated by the PTD using the calibration plots and compared with the true diameter of the projectile. This process provided a means to assess the accuracy of the PTD.

9.7.1 PTD-1 Results

The data obtained during the PTD-1 experiments are presented in Figure 9.3. The data are plotted in blue and the black linear trend line represents the best-fit calibration plot. It should be noted that a polymeric curve could also be fitted to this data, however, the data set we have obtained covers the expected range of particle diameters that will be detected by ODIN and there is little accuracy to be gained by using a non-linear fit. Figure 9.3 suggests that there is a strong positive correlation between the diameter of a projectile and its PT amplitude.

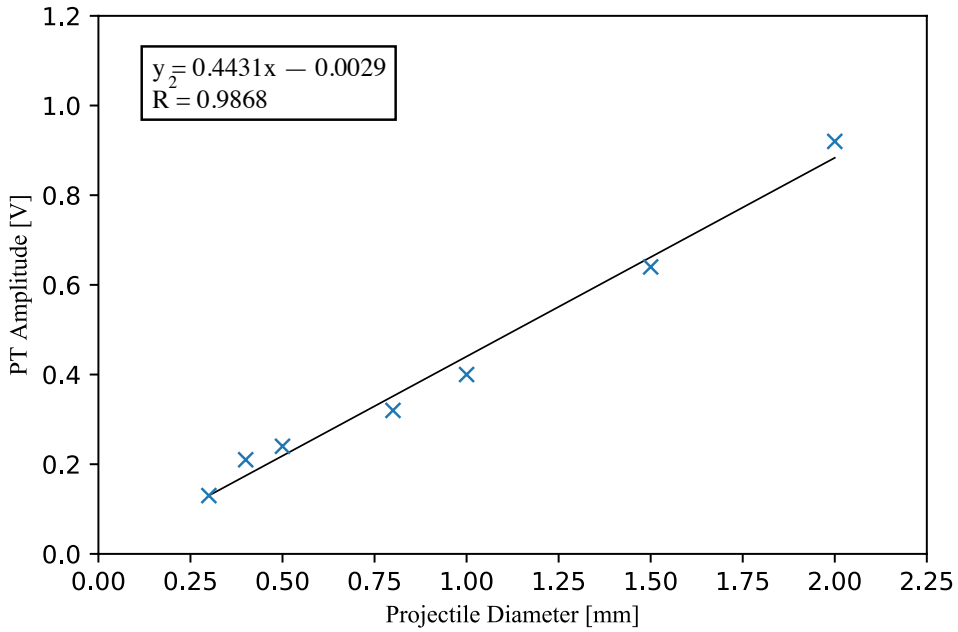

Figure 9.3: PTD-1 calibration plot of projectile diameter against PT amplitude with trend line (black). The average impact velocity was 4.94 km s^{-1} with a standard deviation of 0.22 km s^{-1}.

The equation for the PTD-1 best-fit line was rearranged to give Equation 9.5, which enables the diameter of the projectile to be calculated using the PT amplitude.

$$d_p = \frac{A + 0.0029}{0.4431} \tag{9.5}$$

Where d_p (mm) is the diameter of the projectile and A (V) is the PT amplitude. The PTD algorithm then used Equation 9.5 to calculate the diameter of the projectiles using the PT amplitude. A comparison between the true diameter of projectiles and the diameters calculated by the PTD are presented in Table 9.4. The uncertainties are calculated as a percentage.

The results presented in Table 9.4 show that all of the PTD diameters that were calculated by the PTD during the PTD-1 experiments reside within a ∼20.0 % deviation of the calibration plot, where the average deviation was 7.9 %.

Table 9.4: Results from the PTD-1 experiments, including the true diameter of each projectile, the diameter calculated by the PTD and the deviation.

Experiment	True Diameter (mm)	PTD Diameter (mm)	Deviation (%)
PTD-1.1	0.30	0.30	<0.1
PTD-1.2	0.40	0.48	20.1
PTD-1.3	0.50	0.55	9.6
PTD-1.4	0.80	0.73	8.9
PTD-1.5	1.00	0.91	9.1
PTD-1.6	1.50	1.45	3.3
PTD-1.7	2.00	2.08	4.1

9.7.2 PTD-2 Results

The data obtained during the PTD-2 experiments are presented in Figure 9.4. The data plotted in blue, orange and green, represents the impacts with an incident angle of 0°, 15° and 30° respectively. The black trend line represents the calibration plot for the data with impact angles of 0°.

Figure 9.4 shows that the projectiles with an incident angle of 0° have a strong positive correlation between their diameter and PT amplitude in the $5\,\mathrm{km\,s^{-1}}$ speed regime. The experiments (PTD-2.8 and PTD-2.9) with higher impact angles, however, did not fit this correlation. This is demonstrated by the particles with diameter of 0.8 mm, whose PT amplitude increased with respect to impact angle. This is discussed in Section 9.8.

The equation for the PTD-2 best-fit line was rearranged to give Equation 9.6, which enables the diameter of the projectile to be calculated using the PT amplitude.

$$d_p = \frac{A - 0.0089}{0.3433} \tag{9.6}$$

Where d_p (mm) is the diameter of the projectile and A (V) is the PT amplitude. The PTD algorithm then used Equation 9.6 to calculate the diameter of the projectiles using the PT amplitude. A comparison between the true diameter of projectiles and the diameters calculated by the PTD are presented in Table 9.5.

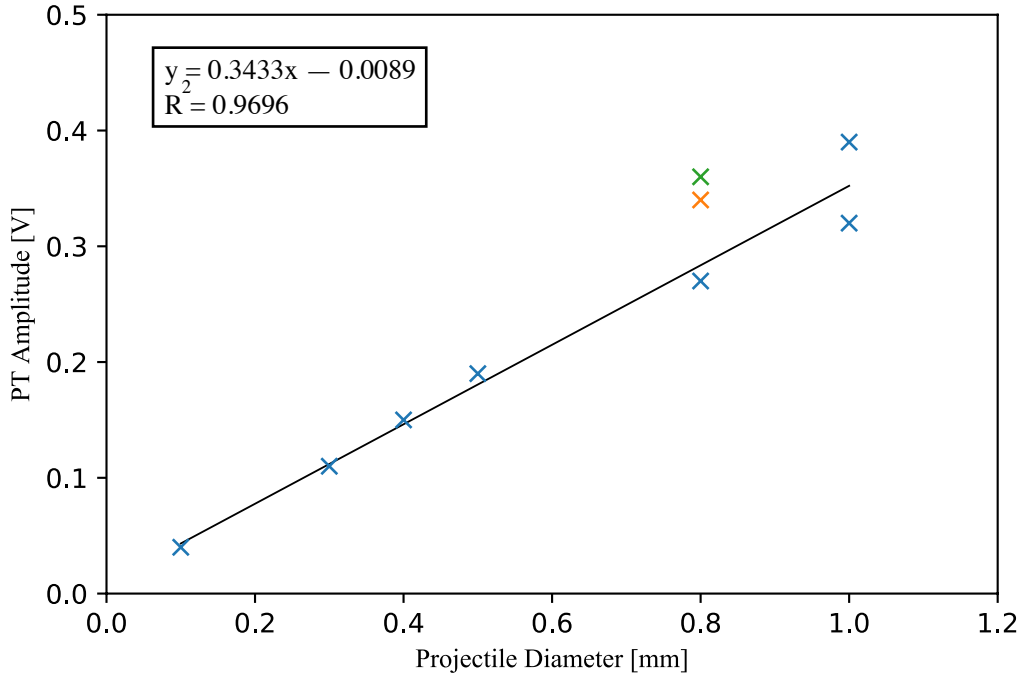

Figure 9.4: PTD-2 calibration plot of projectile diameter against PT amplitude. The trend line (black) only includes data from the 0° impacts. The blue, orange and green data points represent the impacts with an incident angle of 0°, 15° and 30°, respectively. The average impact velocity was 5.03 km s^{-1} with a standard deviation of 0.21 km s^{-1}.

Table 9.5: Results from the PTD-2 experiments, including the true diameter of each projectile, the diameter calculated by the PTD and the deviation.

Experiment	True Diameter (mm)	PTD Diameter (mm)	Deviation (%)	Impact Angle (°)
PTD-2.1	0.1	0.09	9.4	0.0
PTD-2.2	0.3	0.29	1.8	0.0
PTD-2.3	0.4	0.41	2.8	0.0
PTD-2.4	0.5	0.53	5.5	0.0
PTD-2.5	0.8	0.76	4.9	0.0
PTD-2.6	1.0	0.91	9.4	0.0
PTD-2.7	1.0	1.11	11.0	0.0
PTD-2.8	0.8	1.02	27.8	30.0
PTD-2.9	0.8	0.96	20.6	15.0

The average deviation in the diameters calculated during the PTD-2 experiments was 10.4 %. However, this result includes the results from experiment PTD-2.8 and PTD-2.9 which were angled impacts. If those results are removed, the average deviation for the PTD-2 experiments drops to 6.4 %. However, angled impacts are much

more likely in space, and a correction factor of 0.8 and 0.75 can be applied to the PT amplitude for the 15.0° and 30.0° impacts, respectively. However, to better quantify the correlation factor between impact angle and PT amplitude, additional experiments could be performed as mentioned in Section 11.1.

9.7.3 PTD-3 Results

The data obtained during the PTD-3 experiments are presented in Figure 9.5. The data are plotted in blue and the black trend line represents the best-fit to the data. As with the previous sets of experiments, Figure 9.5 suggests that there is a strong positive correlation between the diameter of the projectile and PT amplitude in the $3\,\mathrm{km\,s^{-1}}$ speed regime.

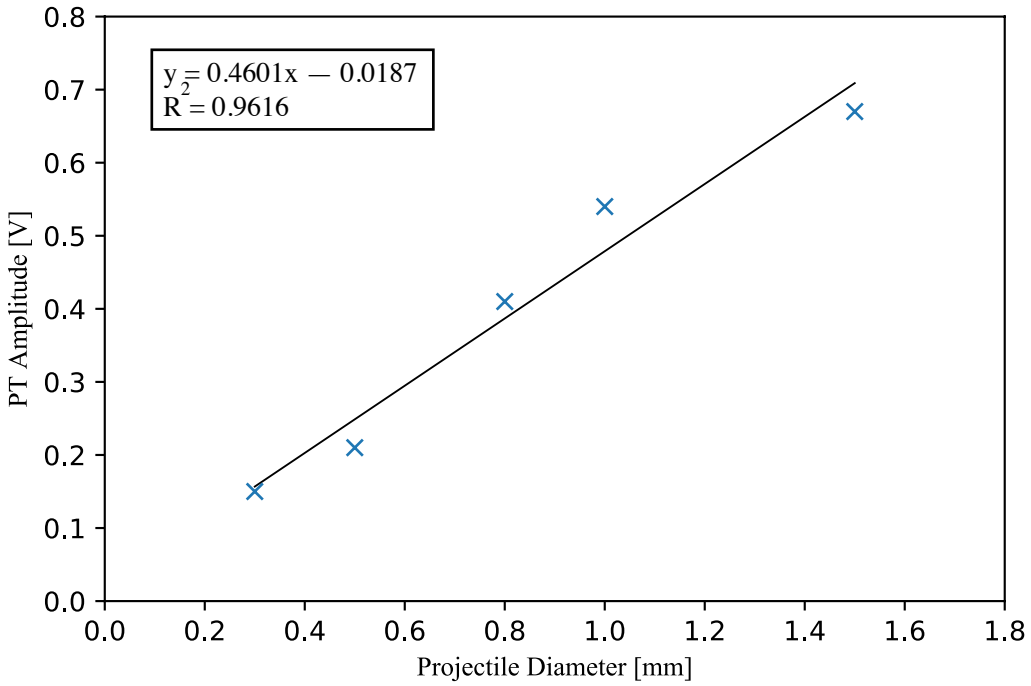

Figure 9.5: PTD-3 calibration plot of projectile diameter against PT amplitude with trend line (black). The average impact velocity was $3.04\,\mathrm{km\,s^{-1}}$ with a standard deviation of $0.09\,\mathrm{km\,s^{-1}}$.

After re-arranging Equation 9.7, which is derived from the best-fit line on the PTD-3 calibration graph, the PTD algorithm calculated the diameter of projectiles using the PT amplitude.

$$d_p = \frac{A - 0.0187}{0.4601} \tag{9.7}$$

Where d_p (mm) is the diameter of the projectile and A (V) is the PT amplitude. A comparison between the true diameter of projectiles and the diameters calculated by the PTD is presented in Table 9.6.

Table 9.6: Results from the PTD-3 experiments, including the true diameter of each projectile, the diameter calculated by the PTD and the deviation.

Experiment	True Diameter (mm)	PTD Diameter (mm)	Deviation (%)
PTD-3.1	0.3	0.29	4.9
PTD-3.2	0.5	0.42	16.8
PTD-3.3	0.8	0.85	6.3
PTD-3.4	1.0	1.13	13.3
PTD-3.5	1.5	1.42	5.6

The average deviation in the diameters calculated during the PTD-3 experiments was 9.4 %. There are no obvious outliers in this data set, which makes it difficult to explain the small increase in uncertainty when compared with the PTD-1 and PTD-2 experiments.

9.8 Discussion

The fourth scientific objective of this research was to design and construct a detector capable of measuring the size of OD/ID particles. The proof-of-concept experiments were used to create calibration plots, which can be used to calculate the diameter of projectiles, using their PT amplitude. Two noteworthy observations were made during the PTD data analysis phase.

The first, was that the impact angle has an effect on the magnitude of the PT amplitude for particles of similar diameter. It is known that impacts with more oblique angles create larger impact holes and, in turn, larger PT amplitudes. Hence, a possible explanation, is that the PT amplitude increases as a function of hole size. Alternatively, the effective ($\sim \frac{1}{\cos\theta}$) increase in the Kapton's thickness, due to the impact geometry, increases the particles' transit time through the Kapton and the PT amplitude might increase as a function of particle transit time.

The second observation was that the impact velocity has an effect on the magnitude of the PT amplitude for particles of similar diameter. The data demonstrates that the PT amplitude decreases as the impact velocity increases. Typically, the size of impact holes increase with respect to impact velocity. This means that impacts with higher velocities would have larger impact holes and, in turn, larger PT amplitudes, which is the opposite of what is observed. An alternative explanation, is that the lower velocity impacts result in a longer particle transit time through the Kapton and, in turn, a larger PT amplitude. Interestingly, this corresponds with the previous suggestion that PT amplitude is related to the transit time through the Kapton.

The results strongly suggest that the PT amplitude is directly proportional to the transit time of the projectile through the Kapton film. This theory is strengthened by the data and previously mentioned observations regarding the change in PT amplitude with respect to impact angle and velocity. In turn, the transit time of a projectile, at a fixed velocity, is directly proportional to the diameter of the projectile, which explains the linear nature of the PT amplitude plots.

The nature of the calibration plots, and the necessity for different speed regimes, will always result in possible deviations, however slight, in the OD/ID diamaters that are calculated by the PTD. This is due to the variations in the PT amplitude caused by diverse impact speeds and angles. The average deviations recorded during the PTD-1, PTD-2 and PTD-3 experiments were $\pm 7.9\,\%$, $\pm 6.4\,\%$ and $\pm 9.4\,\%$, respectively, which is reasonable. Additionally, the proof-of-concept experiments confirmed that the PTD is

sensitive to particles with a diameter $\leq$0.1 mm, which is the smallest individual particle that can be accelerated in the LGG. It is important to note that the constraints of the LGG prevent experimentation and calibration above $\sim$8.5 $\mathrm{km\,s^{-1}}$, making it difficult to create plots for all of the neccessary speed regimes. To account for this, a PT amplitude scaling factor could be developed for different impact velocities, which would eliminate the need for speed regimes and could be applied to all data after the PTD algorithm performs its calculations. Furthermore, hydrocode modelling using code such as Ansys' AUTODYN could be utilized to calculate the scaling factor for velocities greater than 8.5 $\mathrm{km\,s^{-1}}$.

It is acknowledged that the projectiles used during the PTD proof-of-concept experiments were ideal, spherical, non-porous particles. In flight, ODIN will encounter non-ideal particles with irregular shapes and densities and it is probable that the acoustic responces of the Kapton will change with time, which adds a degree of uncertainty to the calibration plots and final accuracy of the PTD.

The NASA Space Debris Sensor (SDS) onboard the ISS is capable of calculating the diameter of OD/ID particles using a similar method to that of the PTD on ODIN, where the amplitude of an acoustic signal is used to calculate the diameter of a particle. The SDS can calculate the diameter of particles with a deviation ranging between 50 % and 200 % (Hamilton et al., 2017). Comparing these results with the deviations measured by ODIN (<10 %) demonstrate the significant advancements made during this research, compared with similar OD/ID detectors currently in use. It is acknowledged that the SDS has an alternative method of measuring the diameter of particles using resistive grids. However, there is no reference to the accuracy of this method in the literature.

To conclude, the PTD subsystem demonstrated that it is capable of measuring the diameter of OD/ID particles. Considering all of the possible factors that can influence the PT amplitude and, in turn, the accuracy of the PTD, a deviation of less than 10 %, across all three sets of experiments, is considered a significant result, although more research needs to be done to constrain the effects of transit time through the Kapton.

Chapter 10

Peak-Trough Energy Subsystem

The Peak-Trough Energy (PTE) subsystem is the subsystem onboard ODIN that measures the kinetic energy of OD/ID dust. It uses the PT amplitude of acoustic signals acquired by the PVDF sensors on the terminal IDG. The PTE uses the same five step process that was implemented by the PTD to calculate the kinetic energy of OD/ID. The five steps are as follows:

1. Determine the distance between the impact coordinate and each sensor.
2. Calculate the PT amplitude recorded by each sensor on the Terminal IDG.
3. Calculate the normalised PT amplitude recorded by each sensor.
4. Average the four normalised PT amplitudes.
5. Calculate the kinetic energy of debris from a calibration plot.

10.1 Impact-Sensor Distance

The first step in the process is similar to that performed by the PTD and involves finding the distance from the impact coordinates to each of the four PVDF sensors. However,

the PTE performs this process on the terminal IDG. The process of calculating the distance between impacts and sensors was discussed in Chapter 6, and again in Chapter 9. Equations 6.5 – 6.8 were used to calculate the distance to each sensor, d_I, d_J, d_K and d_L. The subscripts I, J, K, and L represent the four PVDF sensors on the terminal IDG.

10.2 Peak-Trough Amplitude

The second step in the process involves calculating the PT amplitude of the acoustic signal recorded by each PVDF sensor on the terminal IDG. The process of calculating the PT amplitude is very similar to the one utilised by the PTD, which was discussed in Chapter 9.

It should be noted that whilst the process is the same, the acoustic signals recorded on the terminal IDG are different to those recorded on the primary IDG. Figure 10.1 shows an example of an acoustic signal recorded by one of the PVDF sensors on the primary IDG, which is made of Kapton, and Figure 10.2 shows an example of an acoustic signal recorded by one of the PVDF sensors on the terminal IDG, which is made of syntactic foam. There is a clear difference in the frequency of the acoustic signals recorded on the primary and terminal IDGs. This prompted a series of Fourier transform (FT) analyses, in an attempt to characterise OD/ID using the frequency of acoustic signals, and is described in Section 10.7.4.

10.3 Normalising Peak-Trough Amplitude

The process of normalising the PT amplitude is similar to the one utilised by the PTD and is not repeated in this section as it was discussed in Chapter 9.

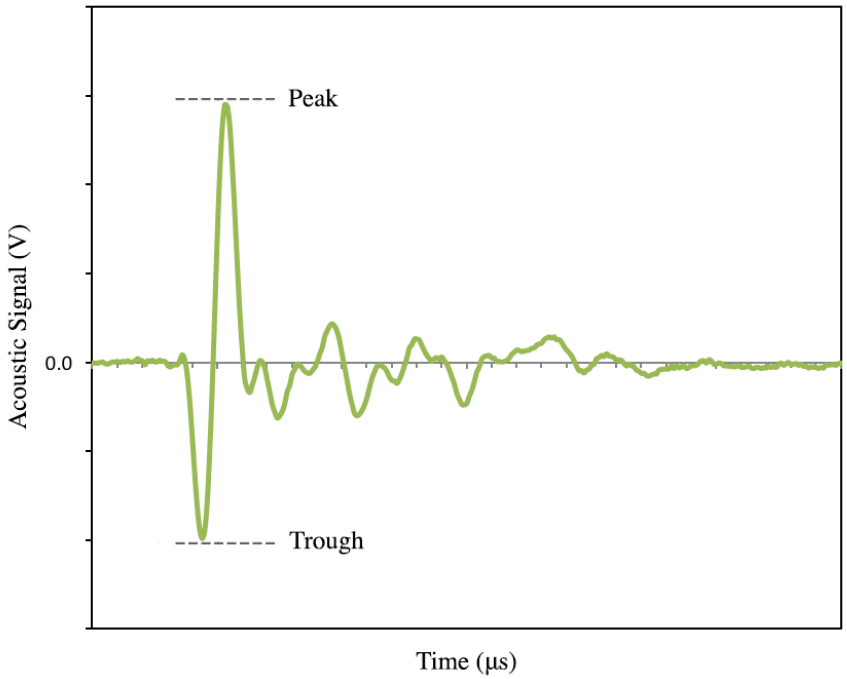

Figure 10.1: The PT amplitude of an acoustic signal recorded by a PVDF sensor on the primary IDG (Kapton).

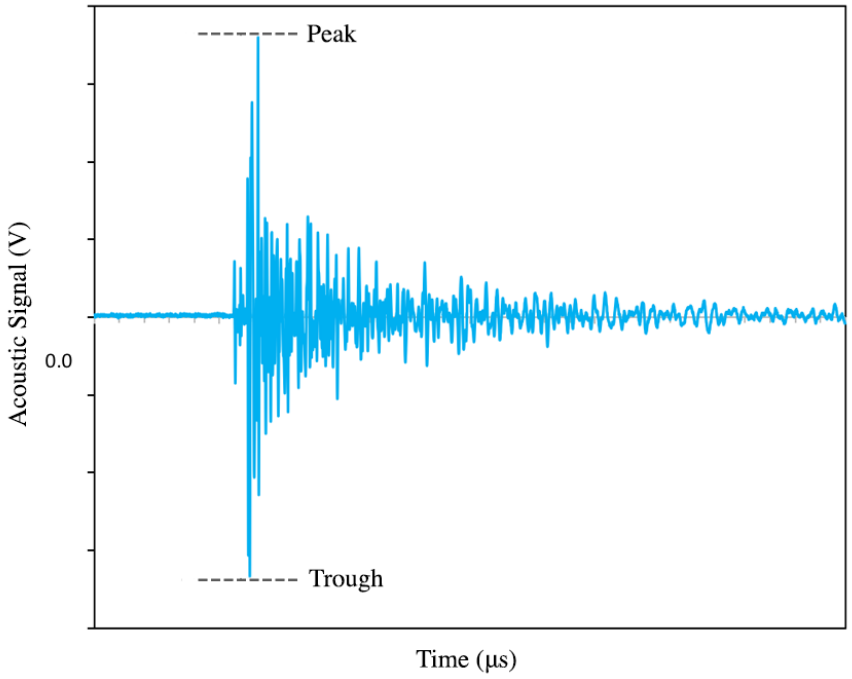

Figure 10.2: The PT amplitude of an acoustic signal recorded by a PVDF sensor on the terminal IDG (syntactic foam).

10.4 Normalised Peak-to-Peak Averaging

The process of averaging the four normalised PT amplitude values is similar to the one utilised by the PTD and is not repeated in this section as it was discussed in Chapter 9.

10.5 Kinetic Energy Calibration

The fifth step in the process is also similar to the one utilised by the PTD subsystem. However, rather than calculating the diameter of OD/ID, the PTE subsystem calculates the kinetic energy of OD/ID particles that impact the terminal IDG.

If a correlation exists between the kinetic energy of OD/ID and the PT amplitude, recorded by the PVDF sensors during impacts with the terminal IDG, it can be used to approximate its kinetic energy. Specifically, the kinetic energy could be calculated from pre-calibrated plots of kinetic energy against PT amplitude.

10.6 PTE Proof-of-Concept

Two sets of experiments were designed to simulate OD/ID impacts with prototypes of ODIN so that kinetic energy calibration plots could be created. The calibration plots were then used to assess the performance of the PTE under test conditions. The process was as follows:

1. Experimentally simulate OD/ID impacts with prototypes of the detector.
2. Create calibration plots for PT amplitude against projectile kinetic energy.
3. Compare calculated kinetic energies with the true kinetic energies.

10.6.1 Simulating OD/ID Impacts

As with the previous proof-of-concept experiments, OD/ID impacts were simulated using the LGG facility at the University of Kent. The acoustic data were then processed by the ICC algorithm so that the impact coordinates could be calculated. The PTE algorithm was then run to calculate the PT amplitude for each impact. The ODIN-SF and ODIN-2 prototypes were used during the PTE proof-of-concept experiments.

Projectiles with a range of diameters (0.1 – 1.5 mm) and velocities (2.0 – 5.0 kms^{-1}) were used in the PTE proof-of-concept experiments. A selection of projectile materials were also used, which provided a means of achieving a wider range of kinetic energies. The materials included; aluminium, stainless steel, titanium and tungsten carbide (WC). Two sets of experiments were conducted during the proof-of-concept phase. Full details of each set of experiments are presented below.

10.6.2 PTE-1 Experiments

The first set of experiments, PTE-1, included 10 impacts with the ODIN-SF prototype. Spherical projectiles with diameters ranging from 0.3 mm - 1.0 mm were accelerated to speeds between $\sim$2.0 kms^{-1} and $\sim$5.0 kms^{-1} with an incident impact angle of 0.0°. Full details of these experiments can be found in Table 10.1.

The purpose of the first suite of experiments was to establish a correlation between kinetic energy and PT-amplitude. A set of projectiles with a range of densities were selected to test the sensitivity of the terminal IDG to material parameters.

10.6.3 PTE-2 Experiments

The second set of experiments, PTE-2, comprised 10 impacts with the ODIN-2 prototype. Spherical projectiles with diameters ranging from 0.1 mm - 1.5 mm were accelerated to velocities between $\sim$3.0 kms^{-1} and $\sim$5.0 kms^{-1} with an incident impact angle of 0.0°. Full details of these experiments can be found in Table 10.2.

Table 10.1: Data from the PTE-1 experiments, including the material, diameter and velocity (±1.0 %) of each projectile. (Note: WC grade 10)

Experiment	Projectile Material	Density ($kg\,m^{-3}$)	Diameter (mm)	Velocity (kms^{-1})
PTE-1.01	Stainless Steel	7800	0.3	5.06
PTE-1.02	Aluminium	2700	1.0	1.99
PTE-1.03	Titanium	4500	1.0	2.11
PTE-1.04	Stainless Steel	7800	0.5	5.14
PTE-1.05	Stainless Steel	7800	1.0	2.04
PTE-1.06	Stainless Steel	7800	1.0	3.12
PTE-1.07	Tungsten Carbide	15630	1.0	2.04
PTE-1.08	Stainless Steel	7800	0.8	5.01
PTE-1.09	Stainless Steel	7800	1.0	4.22
PTE-1.10	Stainless Steel	7800	1.0	4.99

The second suite of experiments was used to test the robustness of the calibration plot created from the PTE-1 experiments. Here a projectile of a fixed density, but a range of speeds was used. Additionally, the data from the PTE-2 experiments were used to refine the calibration plot.

Table 10.2: Data from the PTE-2 experiments, including the material, diameter and velocity (±1.0 %) of each projectile.

Experiment	Projectile Material	Diameter (mm)	Velocity (kms^{-1})
PTE-2.01	Stainless Steel	0.3	3.04
PTE-2.02	Stainless Steel	0.5	3.09
PTE-2.03	Stainless Steel	0.8	2.93
PTE-2.04	Stainless Steel	1.0	2.97
PTE-2.05	Stainless Steel	1.5	3.16
PTE-2.06	Stainless Steel	0.1	5.07
PTE-2.07	Stainless Steel	0.4	5.17
PTE-2.08	Stainless Steel	0.5	5.31
PTE-2.09	Stainless Steel	0.8	4.93
PTE-2.10	Stainless Steel	1.0	4.93

10.7 PTE Results

During both sets of experiments, the PTE recorded the PT amplitude values for each impact and plotted them against the true kinetic energy of each projectile. A line of best fit was added to graph, which was used as the calibration plot, described in Section 10.5. The kinetic energy of each projectile was then calculated by the PTE using the best fit equation and was compared with the true kinetic energy of each projectile. This process provided a means to assess the accuracy of the PTE.

10.7.1 PTE-1 Results

The data that were obtained during the PTE-1 experiments were plotted against kinetic energy and are presented in Figure 10.3. The data are plotted in blue and there is a black trend line, which represents the calibration plot. Figure 10.3 shows that there is a positive correlation between the kinetic energy of a projectile and its corresponding PT amplitude.

The equation for the PTE-1 kinetic energy calibration plot was rearranged to give Equation 10.1, which enables the kinetic energy of each projectile to be calculated using the PT amplitude.

$$KE_p = \frac{A - 0.2761}{0.0671} \tag{10.1}$$

Where KE_p (J) is the kinetic energy of the projectile and A (V) is the PT amplitude. The PTE algorithm then used Equation 10.1 to calculate the kinetic energy of each projectile using its respective PT amplitude. A comparison between the true kinetic energy of each projectile and the kinetic energy that was calculated by the PTE algorithm is presented in Table 10.3. The deviations were calculated as a percentage difference between the true kinetic energy and the kinetic energy calculated by the PTE.

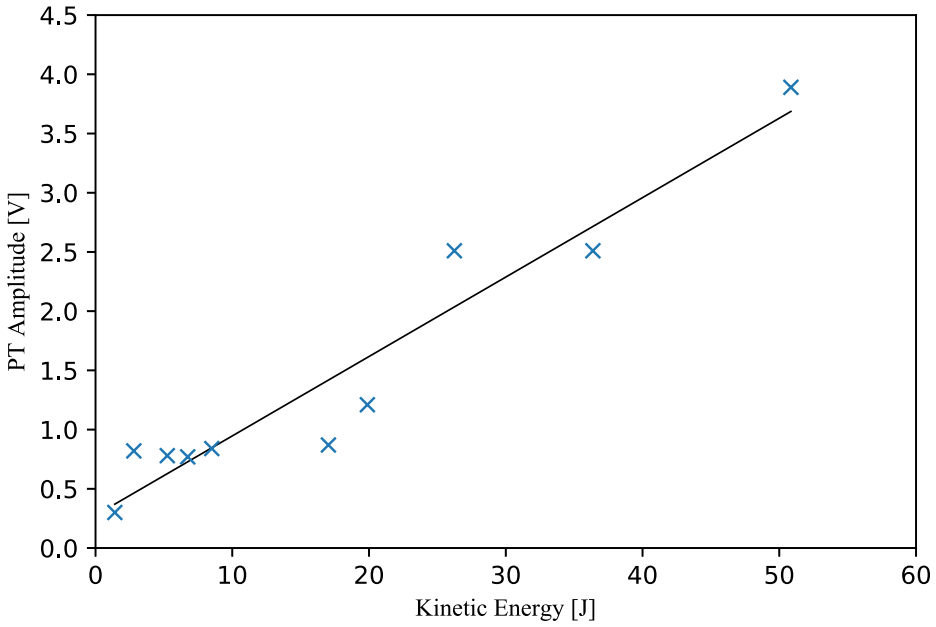

Figure 10.3: PTE-1 calibration plot of the true kinetic energy of projectiles against PT amplitude, with trend line (black).

Table 10.3: Results from the PTE-1 experiments, including the true kinetic energy of each projectile, the kinetic energy that was calculated by the PTE and the deviation between them.

Experiment	True Energy (J)	PTE Energy (J)	Deviation (%)
PTE-1.01	1.41	0.33	76.4
PTE-1.02	2.80	8.15	191.1
PTE-1.03	5.25	7.53	43.6
PTE-1.04	6.74	7.31	8.4
PTE-1.05	8.50	8.35	1.8
PTE-1.06	19.88	13.98	29.7
PTE-1.07	17.03	8.88	47.9
PTE-1.08	26.24	33.32	27.0
PTE-1.09	36.37	33.33	8.3
PTE-1.10	50.85	53.80	5.8

The results obtained during the PTE-1 experiments are presented in Table 10.3 and suggest a lower limit of $\sim$3.0 J for the accurate measurement of kinetic energy using this method. This is demonstrated by experiments PTE-1.01 and PTE-1.02, which had 1.41 J and 2.80 J of kinetic energy and a deviation of 76.4 % and 191.1 %, respectively.

Removing the data from these two experiments yields an average deviation from the calibration plot of 20.5 % across the eight remaining PTE-1 experiments. This seems quite high compared to the other subsystems, but represents a significant improvement over other detectors reviewed in the literature, which appear to have no reliable way of directly measuring kinetic energy (although it should be noted that this 20 % error will likely increase for impactors with unknown physical properties).

10.7.2 PTE-2 Results

The data obtained during the PTE-2 experiments were treated as a "blind" test for the PTE-1 calibration plot, where the PT-amplitudes were used to calculate the kinetic energy of the projectiles using Equation 10.1. Projectiles with a true kinetic energy less than 3.0 J were not included. Additionally, data from PTE-2.05 were removed, as the projectile perforated the terminal IDG, and is unreliable. Table 10.4 shows the results from the test, where an average uncertainty of 30.0 % was recorded. This uncertainty is expected to improve as the calibration plots are refined with additional data.

Table 10.4: Results from the PTE-1 "blind" test, including the true kinetic energy of each projectile, the kinetic energy that was calculated by the PTE-1 calibration plot and the uncertainty. The data has been arranged from lowest to highest true kinetic energy.

Experiment	True Energy (J)	PTE Energy (J)	Uncertainty (%)
PTE-2.07	3.49	3.79	8.4
PTE-2.08	7.20	10.34	43.7
PTE-2.03	8.98	5.25	41.5
PTE-2.04	18.01	11.80	34.5
PTE-2.09	25.41	34.27	34.9
PTE-2.10	49.63	58.10	17.1

The data that was obtained during the PTE-2 experiments was also used to refine the calibration plots. Hence, the data were plotted against the true kinetic energy and is presented in Figure 10.4. The data are plotted in blue and there is a black trend line representing the calibration plot. The outlier from experiment PTE-2.05, where

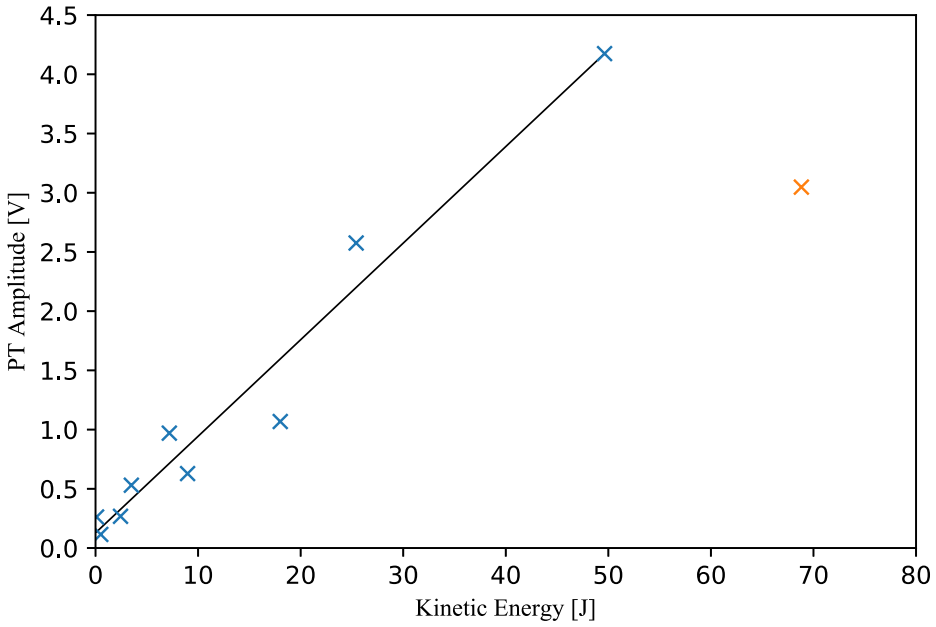

Figure 10.4: PTE-2 calibration plot of the true kinetic energy of projectiles against PT amplitude (blue), with trend line (black). The orange data point represents the outlier from experiment PTE-2.05, which completely penetrated the syntactic foam block.

the projectile perforated the syntactic foam, is represented by the orange data point. PTE-2.05 has the greatest kinetic energy (68.8 J), yet its PT amplitude is ~3.0 V, which according to the graph should represent a particle with a kinetic energy of 35.0 J. This demonstrates that the terminal IDG must completely capture a particle, with minimum ejecta and spall, to perform reliably.

The plot suggests that there is a strong positive correlation between the true kinetic energy of the projectile and PT amplitude. The equation of the best-fit line was rearranged to give Equation 10.2, which enables the kinetic energy of each projectile to be calculated using the PT amplitude.

$$KE_p = \frac{A - 0.1278}{0.0816} \tag{10.2}$$

Where KE_p(J) is the kinetic energy of the projectile and A(V) is the PT amplitude. As previously, the PTE used Equation 10.2 to calculate the kinetic energy of each projectile in the PTE-2 experiments using their PT amplitudes. A comparison between the true kinetic energy of each projectile and the kinetic energy that was calculated by the PTE is presented in Table 10.5. The deviations were calculated as a percentage between the true kinetic energy and calculated kinetic energy.

Table 10.5: Results from the PTE-2 experiments, including the true kinetic energy of each projectile, the kinetic energy that was calculated by the PTE and the deviations between them. The data has been arranged from lowest to highest true kinetic energy.

Experiment	True Energy (J)	PTE Energy (J)	Deviation (%)
PTE-2.06	0.10	1.65	1505.4
PTE-2.01	0.51	-0.16	131.3
PTE-2.02	2.44	1.71	29.7
PTE-2.07	3.49	4.93	41.2
PTE-2.08	7.20	10.32	43.4
PTE-2.03	8.98	6.14	31.6
PTE-2.04	18.01	11.52	36.0
PTE-2.09	25.41	30.00	18.0
PTE-2.10	49.63	49.60	0.10
PTE-2.05	68.82	35.78	48.0

The results obtained during the second set of experiments are presented in Table 10.5 and, like the PTE-1 experiments, suggest a lower limit for the accurate measurement of kinetic energy. In the PTE-2 experiments this limit was ∼1.0 J and is demonstrated by experiments PTE-2.01 and PTE-2.06, which had 0.51 J and 0.10 J of kinetic energy and a deviation from the calibration plot of 131.3 % and 1505.4 %, respectively. Removing data from experiments PTE-2.01, PTE-2.05 and PTE-2.06 yields an average deviation of 28.6 % across the seven remaining PTE-2 experiments.

10.7.3 Collated PTE-1 and PTE-2 Results

The data that were obtained during the PTE-1 and PTE-2 proof-of-concept experiments were then collated. This was possible because the same syntactic foam block

was used on both, the ODIN-SF and ODIN-2, prototypes. As before, the PT amplitude was plotted against the true kinetic energy and a calibration plot was established from the line of best fit (Figure 10.5).

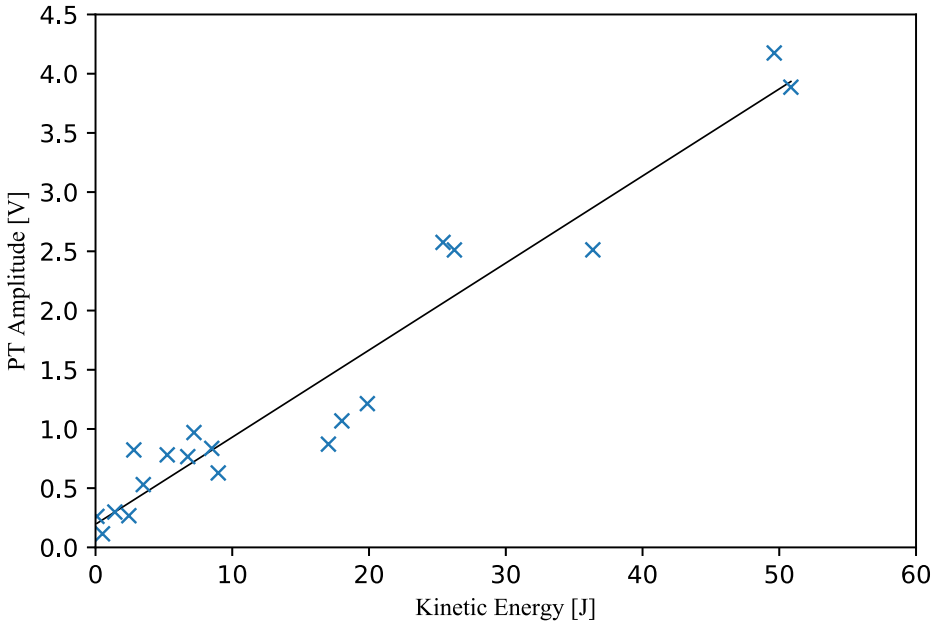

Figure 10.5: Calibration plot for the true kinetic energy of projectiles against PT amplitude, with trend line (black), for the collated data from PTE-1 and PTE-2. The outlier (PTE-2.05) has been removed.

The equation for the collated line of best fit was rearranged to give Equation 10.3, which enables the kinetic energy of each projectile to be calculated using the PT amplitude.

$$KE_p = \frac{A - 0.1953}{0.0735} \tag{10.3}$$

Where KE_p (J) is the kinetic energy of the projectile and A (V) is the PT amplitude. As previously, the PTE used Equation 10.3 to calculate the kinetic energy of each projectile, in the collated data set, using their respective PT amplitudes. A comparison between the true kinetic energy of each projectile and the kinetic energy calculated by

the PTE is presented in Table 10.6. The deviations were calculated as a percentage between the actual kinetic energy and calculated kinetic energy.

Table 10.6: Results from the collated PTE-1 and PTE-2 experiments, including the true kinetic energy of each projectile, the kinetic energy that was calculated by the PTE and the deviations between them. The data from each experiment has been arranged from lowest to highest true kinetic energy.

Experiment	True Energy (J)	PTE Energy (J)	Deviation (%)
PTE-1.01	1.41	1.40	0.5
PTE-1.02	2.80	8.54	205.0
PTE-1.03	5.25	7.98	52.1
PTE-1.04	6.74	7.77	15.2
PTE-1.05	8.50	8.72	2.6
PTE-1.06	19.88	13.86	30.3
PTE-1.07	17.03	9.20	46.0
PTE-1.08	26.24	31.52	20.1
PTE-1.09	36.37	31.53	13.3
PTE-1.10	50.85	50.21	1.2
PTE-2.06	0.10	0.91	786.5
PTE-2.01	0.51	-1.10	314.9
PTE-2.02	2.44	0.98	59.6
PTE-2.07	3.49	4.56	30.4
PTE-2.08	7.20	10.54	46.4
PTE-2.03	8.98	5.90	34.3
PTE-2.04	18.01	11.88	34.1
PTE-2.09	25.41	32.38	27.4
PTE-2.10	49.63	54.14	9.1

The collated results obtained during the first and second set of experiments are presented in Table 10.6. The calculated kinetic energies are different to those in the PTE-1 and PTE-2 results as they were calculated using a different calibration plot. Like the PTE-1 and PTE-2 experiments, the data indicates that there is a lower limit for the accurate measurement of kinetic energy at $\sim$3.0 J. This was demonstrated by experiments PTE-1.02, PTE-2.01, PTE-2.02 and PTE-2.06, which had kinetic energies of 2.80 J, 0.51 J, 2.44 J and 0.10 J and a deviation of 205.0 %, 314.9 %, 59.6 % and 786.5 %, respectively. Removing the data from the experiments where the kinetic energy was less than $\sim$3.0 J yields an average deviation of 25.9 % across the 14 remaining experiments.

10.7.4 Fourier Transform Analysis

An attempt was made to establish a relationship between the distinct frequencies of the acoustic data and the kinetic energy of individual particles. This was done by applying a fast Fourier transform (FFT) across the data to divide it into its frequency components.

The FFT was applied to data from each sensor on the terminal IDG and plotted on a graph of frequency against amplitude. An envelope encompassing the frequency spectrum was added to each plot, and the peak was used to approximate the characteristic frequency.

Figure 10.6 and 10.7 shows the FFT and envelopes from each sensor for a projectile with 8.5 J and 50.8 J, respectively. The envelopes are similar for each sensor and there is an increase in peak frequency as the kinetic energy increases.

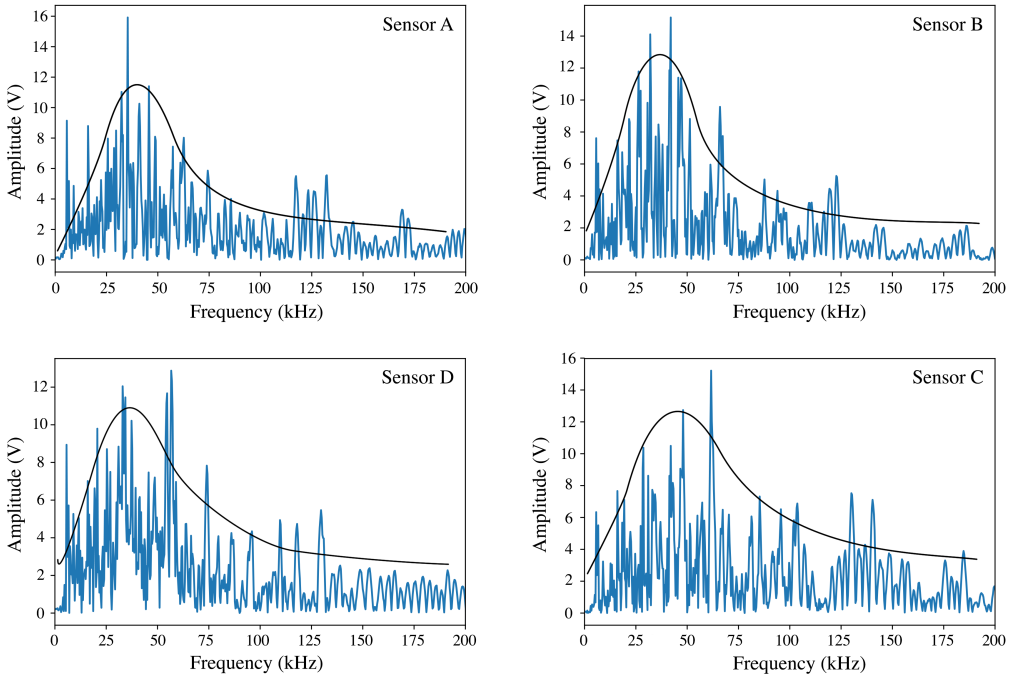

Figure 10.6: Fourier transforms of the data recorded by each sensor on the terminal IDG for an impact with 8.5 J of kinetic energy.

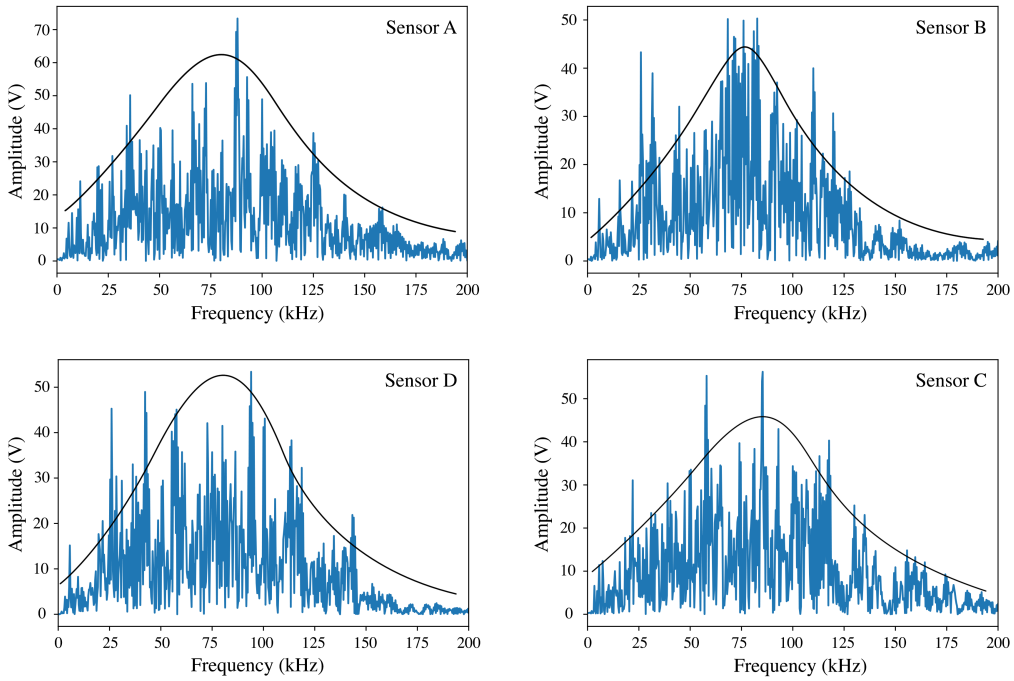

Figure 10.7: Fourier transforms of the data recorded by each sensor on the terminal IDG for an impact with 50.8 J of kinetic energy.

A sample of the PTE-1 data were analysed to see if this correlation of peak frequency to kinetic energy was potentially useful. This is shown in Figure 10.8, where it can be seen that there is a weak positive correlation between the peak frequency and projectile kinetic energy. A possible explanation for the weak correlation could be a result of the inhomogeneous nature of the syntactic foam, so small domains in the foam will have different frequency responses.

Although this was interesting observation, and is worthy of further research, it was deemed too computationally intesive and inaccurate to be of use on ODIN. Further work might involve doing more extensive filtering and frequency analysis.

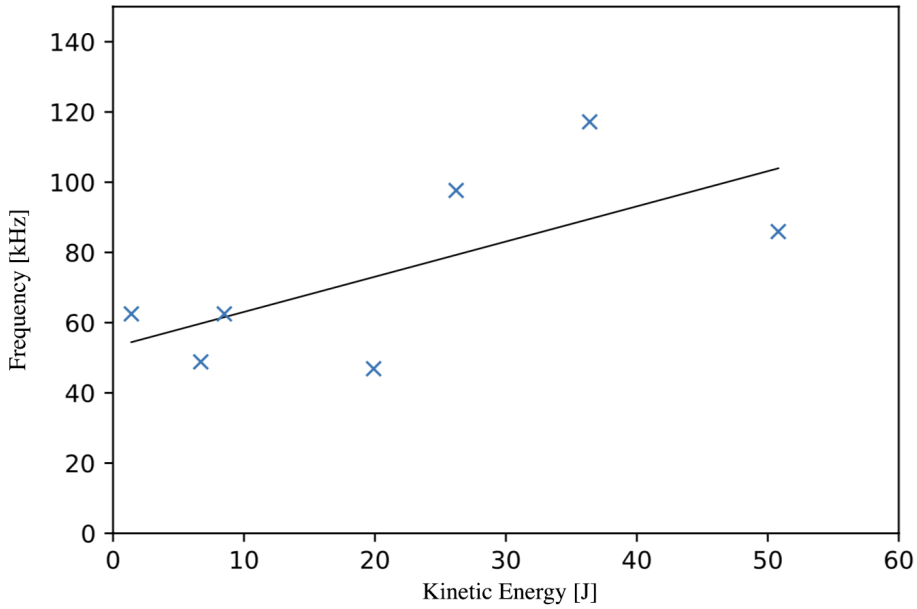

Figure 10.8: A plot of the peak frequencies (Hz) against kinetic energy (J) for a sample of the PTE-1 data. The line of best fit demonstrates the weak postive correlation between the peak frequency and projectile kinetic energy.

10.7.5 Mass and Density Calculations

In Chapter 1 it was stated that the kinetic energy, combined with the velocity and diameter of particles recorded by the PTE, IGV and PTD subsystems, respectively, could be used to calculate the mass and density of OD/ID passing through the detector.

The mass and density of three particles that were analysed by the PTE, IGV and PTD were calculated and compare with the preimpact characteristics. The results are presented in Table 10.7 and Table 10.8, respectively.

Table 10.7: Comparison between the mass of particles calculated from the PTE and IGV results and their pre-impact mass.

Experiment	True Mass (kg)	Calculated Mass (kg)	Uncertainty (%)
PTE-2.02	5.1×10^{-7}	3.9×10^{-7}	24.1
PTE-2.03	2.1×10^{-6}	1.6×10^{-6}	22.4
PTE-2.04	4.1×10^{-6}	2.8×10^{-6}	30.5

Table 10.8: Comparison between the density of particles calculated from the PTE, IGV and PTD results and their pre-impact densities.

Experiment	True Density ($\mathrm{kg\,m^{-3}}$)	Calculated Density ($\mathrm{kg\,m^{-3}}$)	Uncertainty (%)
PTE-2.02	7800	9994.6	28.1
PTE-2.03	7800	5047.6	35.3
PTE-2.04	7800	3756.0	51.8

Considering the errors in IGV (v^2) and PTE (KE) calculations are both incorporated into the mass calculations, an average uncertainty of 25.6 % is well received. In addition to the IGV and PTE uncertainties, the density calculations also incorporate the PTD (r^3) uncertainties. The average uncertainty for the density was 38.4 %. However, the method of calculating density assumes a spherical projectile, and in practice would be less accurate than the results exhibited here.

10.8 Discussion

The fifth scientific objective outlined at the start of this research was to create a detector capable of measuring the kinetic energy of OD/ID particles. The proof-of-concept experiments were carried out to create calibration plots which, in turn, could be used to calculate the kinetic energy of projectiles using their PT amplitude.

The proof-of-concept experiments indicated that the amplitude of the acoustic signals in the syntactic foam are independent of the individual speed, mass and density of a particle, but are directly linearly proportional to the kinetic energy of the projectile. This proves that the syntactic foam directly measures the kinetic energy of the captured projectile, and is thus independent of the physical properties of the impactor. This relationship, however, is dependent on the particle being captured by the terminal IDG, without perforation or spall. This was demonstrated in experiment PTE-2.05, where the projectile had a kinetic energy of 68.8 J, but a PT amplitude of only ∼3.0 V, which is more typical of a particle with a kinetic energy of 35.0 J. As the particle perforated the terminal IDG, it only deposited a fraction of its kinetic energy into the syntactic

foam, which explains the shortfall in the kinetic energy that was calculated by the PTE algorithm.

The sensitivity of the PTE subsytem is approximately 3.0 J, below which, the kinetic energy measurements are unreliable. To put this into context, OD composed of aluminium ($\rho = 2700\,\mathrm{kg\,m^{-3}}$), with a diameter between 0.4 mm and 1.0 mm and a velocity of $10\,\mathrm{km\,s^{-1}}$, which is realistic in LEO, would have a kinetic energy ranging between ∼5 J and ∼70 J. Furthermore, ID such as micrometeoroids ($\rho = 500\,\mathrm{kg\,m^{-3}}$ – $3000\,\mathrm{kg\,m^{-3}}$), with a diameter between 0.4 mm and 1.0 mm and a velocity of $20\,\mathrm{km\,s^{-1}}$, would have a kinetic energy between ∼3 J and ∼300 J. Experiments could be performed using the LGG to validate the accuracy of the PTE subsystem for higher kinetic energy impacts.

To conclude, ODIN is the first detector that is capable of directly measuring kinetic energy of OD/ID particles, which is possible due to the development of the syntactic foam terminal IDG. Hence, the PTE subsystem cannot be compared with any other detectors. Considering it is the first attempt at directly measuring the kinetic energy of particles, the average deviation of ∼26 %, for the collated PTE-1 and PTE-2 data, is reasonable.

Chapter 11

Conclusions

The overall goal of this research was to design and construct a working prototype of an orbital debris and interplanetary dust detector that could contribute to advancements in the next generation of detectors. As a proof-of-concept it was necessary to perform hypervelocity impact experiments with debris and dust particle analogs and determine characteristics of specific interest including flux, size, velocity, trajectory, kinetic energy, density and mass. Although previously flown detectors are capable of measuring a number of these parameters, none have integrated the capacity to measure all of them simultaneously. In the past, post-flight surface analysis on the Space Shuttle provided routine updates on the characteristics of millimeter and submillimeter particles in low Earth orbit. However, since the retirement of the Space Shuttle program in 2011, there has been very little new data available and, consequently, research in this area is urgently needed for both scientific and commercial purposes. The ODIN detector was designed in order to achieve the following scientific objectives for all orbital debris and interplanetary dust impacting on the detection surface:

1. Measure the flux.
2. Calculate the trajectory.
3. Calculate the speed.

4. Determine the size.
5. Determine the kinetic energy.
6. Approximate the mass and density.

In addition to the scientific objectives, the detector was expected to achieve the following design objectives:

7. Large detection area to maximise the efficiency of the scientific analysis.
8. Constructed with low cost materials which are space qualified, or qualifiable.
9. A lightweight construction to minimise launch costs.
10. Low computational and electrical requirements to minimise operation and maintenance costs.

After preparing theoretical designs based on previous detector constraints, and testing a range of detector concepts, configurations and materials, a prototype was constructed that successfully achieved each of these objectives, but with varying degrees of accuracy and precision.

The Impact Cartesian Coordinate (ICC) subsystem described in Chapter 6 was designed to measure the flux and record the impact coordinates of particles that interact with ODIN. The ICC directly achieved the first objective by providing a means of counting distinct impacts, in real-time, up to a maximum rate of approximately 2940 impacts per second. Previous detectors, such as LDEF, require post-flight analysis which limits them to an average flux calculation across their mission duration. The ICC's ability to record the flux in real-time provides an advancement in scientific analysis as periods of high and low flux can be detected and catalogued for use in future environment models.

A comprehensive algorithm was developed for the ICC providing it with a method of calculating the impact coordinates of particles interacting with the primary, secondary and terminal IDGs. This method is different to those used by current detectors, such as NASA's Space Debris Sensor (SDS), which uses a set of algebraic equations to calculate impact coordinates using acoustic signals from three orthogonally located sensors. Accurate impact coordinates were necessary for acoustic normalisation and trajectory/time-of-flight calculations. Seven experiments were performed on the ODIN-Beta prototype, while fourteen experiments were performed on the ODIN-2 prototype as a proof-of-concept for the ICC subsystem. The average uncertainty on ODIN-Beta was a 2.8 mm deviation between the true impact coordinates and those that were calculated by the ICC algorithm. The average uncertainty on ODIN-2 was a 1.4 mm deviation between the true impact coordinates and those that were calculated by the ICC algorithm. These results represent a significant improvement when comparing the ICC with alternative detectors currently in operation, such as the SDS, which has an uncertainty of ± 8 mm when calculating impact coordinates.

The Unit Vector Trajectory (UVT) subsystem described in Chapter 7 was designed to achieve the second scientific objective and calculate the trajectory of particles that interact with ODIN. A set of experiments were conducted to analyse three different impactor trajectories as a proof-of-concept for the UVT subsystem. These demonstrated that the UVT can, on average, calculate the trajectory of particles to a $\pm 0.4^{\circ}$ level of confidence. This demonstrates a significant improvement on comparable detectors such as the SDS, which calculates the trajectory of particles to $\pm 3^{\circ}$ on average.

The third scientific objective was achieved using the Impact Gate Velocity (IGV) subsytem described in Chapter 8. It was designed to use the time-of-flight and the known distance between the primary and secondary IDGs to calculate the velocity of particles interacting with ODIN. Eight proof-of-concept experiments were performed on the ODIN-2 prototype, which yielded an average uncertainty of 4.0 % between the true velocity and that calculated by the IGV subsystem. Although there are several

other detectors that are capable of measuring the velocity of particles, including the SDS, which is considered as state-of-the-art and in use today, the accuracy of the IGV calculations on ODIN represent an improvement by more than a factor of four.

The Peak-Trough Diameter (PTD) subsystem described in Chapter 9 was designed to calculate the diameter of particles passing through the primary IDG. The most common method of analysing the size of particles is through post-flight inspections of impact craters, which has financial disadvantages and scientific constraints as the size of particles cannot be related to time of impact. An obvious advancement would include accurate real-time measurements of particle diameters. Three sets of experiments were conducted as a proof-of-concept for the PTD subsystem. The first set included seven impacts with the ODIN-Beta prototype, the second and third sets included nine and five impacts on the ODIN-2 prototype, respectively. The experiments conducted on the ODIN-2 prototype demonstrated that an average confidence of $\pm 8.5\,\%$ is achievable. The smallest particle that was included in the experiments was a 100 µm stainless steel sphere. The PTD calculated this particle to be $\sim$90 µm, suggesting that the sensitivity of the PTD is reliable to at least $\sim$100 µm, although this could change as a function of particle density. An interesting observation, but not unexpected, was the effect of impact angle on the PT-amplitude, which increases with respect to impact angle. This is due to the increased amount of Kapton that is removed during impacts with oblique angles.

The fifth scientific objective was achieved using the Peak-Trough Energy (PTE) subsystem described in Chapter 10. The PTE was designed to measure the kinetic energy of particles using the PT-amplitude, which is a measurement unique to ODIN. Calculating the kinetic energy of individual particles was of particular interest as it allows the mass and density to be calculated. The PTE was designed to capture particles in the terminal IDG, which absorbs their kinetic energy and can be measured using PVDF sensors. Twenty experiments were conducted as a proof-of-concept on the ODIN-SF and ODIN-2 prototypes. The PTE demonstrated its ability to measure the

kinetic energy of particles with an uncertainty of 26 %. Interestingly, this uncertainty quickly rises for particles with kinetic energy less than ∼3 J. It is difficult to compare these results with other detectors as direct measurements of kinetic energy are unique to ODIN. It should be noted that by using a combination of velocity, kinetic energy and diameter readings, the mass, and possible impactor composition (density) was calculated and had average uncertainties of 25.6 % and 38.4 %, respectively.

In addition to the scientific objectives, several design objectives were outlined and addressed during the design and construction process of this research. Steps were taken to increase the detection area of ODIN while minimising its weight. Additionally, low cost materials that were either space qualified, or qualifiable, were used where possible. A full discussion of the design and construction of each prototype can be found in Chapter 4.

To conclude, this research achieved its overall goal of designing and constructing a working prototype of an OD/ID detector that builds on the design of detectors in current use, and has several new and unique features that improve its overall performance. The detector, ODIN, is capable of calculating the flux, trajectory, speed, size, kinetic energy, mass and density of particles that interact with it - and does so to a higher degree of accuracy than other detectors currently in operation.

11.1 Future Work

There are three main areas of interest that could be explored in future work. Broadly, these areas include; (1) the acoustic signals, (2) the PVDF sensors, and (3) particle dynamics.

The acoustic signals are the ingredients for all measurements and data analysis carried out by the subsystems on ODIN. Hence, given more time, it would be interesting to investigate the physical properties of the acoustic signals in more detail. A dedicated study of the signal speed in Kapton would be interesting, as this might change with

respect to impact conditions (speed and angle) and impactor morphology (shape, size and density). It is also likely that shock waves occur over very short distances from the impact location, but then decay to stress waves, which travel at slower speeds. Furthermore, wave speeds may vary depending on their direction of travel. A thorough understanding of the waves may help improve the accuracy of the subsytems. Additionally, knowledge regarding acoustic edge reflections could potentially contribute to refinements in the physical configuration of the detector. This could be investigated further using hydrocode modelling with codes such as Ansys' AUTODYN. Additionally, the frame could be designed to better absorb the acoustic waves by impedence matching techniques, allowing the sensors to be positioned closer to the frame. Finally, it is possible that acoustic diffraction occurs around impact holes and could have an effect on the accuracy and life-time of the detector. If a wave diffracts around an impact hole caused by another particle, the distance it travels to the PVDF sensor increases. As the impact holes on the Kapton accumulate, the distance travelled by the waves increases due to additional diffraction. After a period of time, these distances could build up, affecting the arrival time of the acoustic signals recorded by the sensors, which could lead to uncertainties in the analytical subsytems. Again, it is suggested that hydrocode modelling with codes such as Ansys' AUTODYN could be utilised to resolve the specific increase in distance travelled by the acoustic waves and the expected arrival time delays caused by degredation of the Kapton caused by impact holes.

The PVDF sensors are accountable for the consistent, and accurate, collection of acoustic data. Variables, such as the acoustic signal's angle of approach, can have an effect on the sensitivity of the sensors and could be explored in more detail. Additionally, unexplored factors, such as the substrate's thickness, which was 25 µm on ODIN, may improve the sensitivity of the detector to particles smaller than ∼100 µm. Finally, the effect of the aging of the detectors after (potentially) years in space could be investigated.

There are several areas of interest surrounding particle dynamics. A study focusing on the primary IDG and its affect on incident particles would be of particular interest, as little is understood regarding the change in velocity (speed and direction) of particles as they pass through the Kapton. There was no definitive evidence to suggest a change in a particle's trajectory as it impacts the primary IDG. However, there was evidence to suggest that its speed may change. Hence, a dedicated set of experiments could be conducted to explore this.

While calibrating the PTD subsytem, it was observed that the correlation between a particle's diameter and its PT amplitude is dependent on the impact speed. Additional experiments could be used to improve the accuracy of the PTD calibration plots, which were created for the $3.0\,\mathrm{km\,s^{-1}}$ and $5.0\,\mathrm{km\,s^{-1}}$ speed regimes. Specifically, calibration plots for the $1.0\,\mathrm{km\,s^{-1}}$ to $7.0\,\mathrm{km\,s^{-1}}$ speed regimes would provide greater confidence in the PTD subsystem.

During the proof-of-concept experiments, it was demonstrated that the impact angle of incident projectiles can affect the PT amplitude of the acoustic signals. The experiments conducted in this research were limited to incident angles of 0.0°, 15.0° and 30.0°. Hence, an investigation encompassing a larger range of incident angles would be of interest.

Finally, it was acknowledged that ideal, spherical, non-porous partciles were used throughout the proof-of-concept experiments, which is not neccessarily a fair representation of the population of OD/ID particles. Although it would be experimentally challenging, an investigation into the affect of irregular projectiles on the acoustic data would be interesting.

Bibliography

Alby, F., Lansard, E., and Michal, T. (1997). Collision of cerise with space debris. In Second European Conference on Space Debris, volume 393, page 589.

Anderson, C. (2013). Rethinking public–private space travel. Space Policy, 29(4):266–271.

Bauer, W., Romberg, O., Wiedemann, C., Drolshagen, G., and Vrsmann, P. (2014). Development of in-situ Space Debris Detector. Advances in Space Research, 54(9):1858 – 1869.

Bernhard, R., Christiansen, E., and Kerr, J. (2001). Space Shuttle Meteoroid and Orbital Debris Impact Damage. International Journal of Impact Engineering, 26(1):33 – 38.

Bernhard, R., Christiansen, E., and Kessler, D. (1997). Orbital debris as detected on exposed spacecraft. International journal of impact engineering, 20(1-5):111–120.

Burchell, M. J., Cole, M. J., McDonnell, J., and Zarnecki, J. C. (1999). Hypervelocity impact studies using the 2 MV Van de Graaff accelerator and two-stage light gas gun of the University of Kent at Canterbury. Measurement Science and Technology, 10(1):41.

Burchell, M. J., Corsaro, R., Giovane, F., Cole, M., Sadilek, A., Price, M., and Liou, J.-C. (2013). A New Cosmic Dust Detector with a Novel Method Using a Resistive Grid Sensitive to Hypervelocity Impacts. Procedia Engineering, 58(Supplement C):68 – 76. Proceedings of the 12th Hypervelocity Impact Symposium.

Caswell, R. D., McBride, N., and Taylor, A. (1995). Olympus end of life anomaly a perseid meteoroid impact event? International Journal of Impact Engineering, 17(1):139 – 150. Hypervelocity Impact.

Christiansen, E., Hyde, J., and Bernhard, R. (2004). Space shuttle debris and meteoroid impacts. Advances in Space Research, 34(5):1097 – 1103.

Christiansen, E. L. (1993). Design and performance equations for advanced meteoroid and debris shields. International Journal of Impact Engineering, 14(1-4):145–156.

Christiansen, E. L. (2003). Meteoroid/debris shielding. National Aeronautics and Space Administration, Lyndon B. Johnson Space Center.

Christiansen, E. L. and Kerr, J. H. (1993). Mesh double-bumper shield: A low-weight alternative for spacecraft meteoroid and orbital debris protection. International Journal of Impact Engineering, 14(1):169 – 180.

Christiansen, E. L., Nagy, K., Lear, D. M., and Prior, T. G. (2009). Space station MMOD shielding. Acta Astronautica, 65(7):921 – 929.

Corsaro, R. D., Giovane, F., Liou, J.-C., Burchell, M. J., Cole, M. J., Williams, E. G., Lagakos, N., Sadilek, A., and Anderson, C. R. (2016). Characterization of space dust using acoustic impact detection. The Journal of the Acoustical Society of America, 140(2):1429–1438.

Crozier, W. and Hume, W. (1957). High-Velocity, Light-Gas Gun. Journal of Applied Physics, 28(8):892–894.

Curdt, W. and Keller, H. (1990). Large dust particles along the Giotto trajectory. Icarus, 86(1):305 – 313.

Dietzel, H., Eichhorn, G., Fechtig, H., Grn, E., Hoffmann, H. J., and Kissel, J. (1973). The HEOS 2 and HELIOS micrometeoroid experiments. Journal of Physics E: Scientific Instruments, 6(3):209.

Doolan, C. (2001). A two-stage light gas gun for the study of high speed impact in propellants. Technical report, Aeronautical and Maritime Research Lab Salisbury (Australia) Weapons Systems Div.

Faure, P., Masuyama, S., Nakamoto, H., Akahoshi, Y., Kitazawa, Y., and Koura, T. (2013). Space dust impacts detector development for the evaluation of ejecta. Procedia Engineering, 58(Supplement C):594 – 600. Proceedings of the 12th Hypervelocity Impact Symposium.

Greenberg, J. M. (2002). Cosmic dust and our origins. Surface Science, 500(1):793 – 822.

Grün, E., Sternovsky, Z., Horanyi, M., Hoxie, V., Robertson, S., Xi, J., Auer, S., Landgraf, M., Postberg, F., Price, M., Srama, R., Starkey, N., Hillier, J., Franchi, I., Tsou, P., Westphal, A., and Gainsforth, Z. (2012). Active Cosmic Dust Collector. Planetary and Space Science, 60(1):261 – 273. Titan Through Time: A Workshop on Titans Formation, Evolution and Fate.

Hamilton, J., c. Liou, J., Anz-meador, P., Corsaro, R., Giovane, F., Matney, M., and Christiansen, E. (2017). Development of the Space Debris Sensor (SDS). 7th European Conference on Space Debris, 7.

Hirai, T., Cole, M. J., Fujii, M., Hasegawa, S., Iwai, T., Kobayashi, M., Srama, R., and Yano, H. (2014). Microparticle impact calibration of the Arrayed Large-Area Dust Detectors in INterplanetary space (ALADDIN) onboard the solar power sail demonstrator IKAROS. Planetary and Space Science, 100(Supplement C):87 – 97. Cosmic Dust VI.

Hoffman, H.-J., Fechtig, H., Grn, E., and Kissel, J. (1975). Temporal fluctuations and anisotropy of the micrometeoroid flux in the Earth-Moon system measured by HEOS 2. Planetary and Space Science, 23(6):985 – 991.

Horanyi, M., Hoxie, V., James, D., Poppe, A., and Bryant, C. (2009). The Student Dust Counter on the New Horizons Mission. Space Science Reviews, pages 387–402.

Hörz, F. (1986). Trajectory determinations and collection of micrometeoroids on the space station. Report of the Workshop on Micrometeorite Capture Experiments.

Hörz, F., See, T., P. Bernhard, R., and E. Brownlee, D. (1995). Natural and orbital debris particles on LDEF's trailing and forward-facing surfaces. LDEF: 69 Months in Space. Third Post-Retrieval Symposium, pages 415–429.

Humes, D. H. (1993). Small craters on the meteoroid and space debris impact experiment. NASA Conference Publication, 3275(Part 1):287 – 321.

Hyde, J., Christiansen, E., Bernhard, R., Kerr, J., and Lear, D. (2001). A history of meteroid and orbital debris impacts on the Space Shuttle. European Space Agency-Publications-ESA SP, 473:191–196.

Inagaki, M., Harada, S., Sato, T., Nakajima, T., Horino, Y., and Morita, K. (1989). Carbonization of polyimide film Kapton. Carbon, 27(2):253 – 257.

Jayavardhan, M., Kumar, B. B., Doddamani, M., Singh, A. K., Zeltmann, S. E., and Gupta, N. (2017). Development of glass microballoon/hdpe syntactic foams by compression molding. Composites Part B: Engineering, 130:119 – 131.

Johnson, N. L. (2010). Orbital debris: the growing threat to space operations. 33rd Annual Guidance and Control Conference; 6-10 Feb. 2010; Breckenridge, CO; United States, (AAS 10-011, JSC-CN-19694).

Juvela, M. (2015). Dust emission and scattering in dense interstellar clouds. Planetary and Space Science, 116(Supplement C):64 – 72. Cosmic Dust VII.

Kearsley, A., Graham, G., McDonnell, J., Taylor, E., Drolshagen, G., Chater, R., McPhail, D., and Burchell, M. (2007). The chemical composition of micrometeoroids impacting upon the solar arrays of the Hubble Space Telescope. Advances in Space Research, 39(4):590 – 604.

Kelso, T. et al. (2009). Analysis of the iridium 33-cosmos 2251 collision. Advances in the Astronautical Sciences, 135(2):1099–1112.

Kessler, D. J., Reynolds, R. C., and Anz-Meador, P. D. (1989). Orbital debris environment for spacecraft designed to operate in low earth orbit. Technical report, National Aeronautics and Space Administration Washington DC.

Klinkrad, H. (2006). Space debris: Models and Risk Analysis. Published in association with Praxis Pub.

Klinkrad, H. and Sdunnus, H. (1997). Concepts and applications of the master space debris environment model. Advances in Space Research, 19(2):277–280.

Kreowski, J. (2017). Hunting for invisible dust in the milky way. Planetary and Space Science, 149(Supplement C):72 – 76. Special Issue: Cosmic Dust IX.

Krisko, P., Flegel, S., Matney, M., Jarkey, D., and Braun, V. (2015). Ordem 3.0 and master-2009 modeled debris population comparison. Acta Astronautica, 113(Supplement C):204 – 211.

Krisko, P. H. (2014). The new nasa orbital debris engineering model ordem 3.0. In AIAA/AAS Astrodynamics Specialist Conference, page 4227.

Lal, D. and Jull, A. T. (2002). Atmospheric cosmic dust fluxes in the size range 10–4 to 10 centimeters. The Astrophysical Journal, 576(2):1090–1097.

Lambert, M., Schfer, F. K., and Geyer, T. (2001). Impact damage on sandwich panels and multi-layer insulation. International Journal of Impact Engineering, 26(1):369 – 380.

Leinert, C. and Grün, E. (1990). Interplanetary dust. In Physics of the inner heliosphere I, pages 207–275. Springer.

Levin, E., Pearson, J., and Carroll, J. (2012). Wholesale debris removal from leo. Acta Astronautica, 73(Supplement C):100 – 108.

Levin, G. and Christiansen, E. (1997). The space shuttle program pre-flight meteoroid and orbital debris risk/damage predictions and post-flight damage assessments. Second European Conference on Space Debris, ESA-SP 393:633.

Liou, J., Dermott, S., and Xu, Y. (1995). The contribution of cometary dust to the zodiacal cloud. Planetary and Space Science, 43(6):717 – 722. Asteroids, Comets and Meteors 1993-V.

Liou, J., Johnson, N., and Hill, N. (2010). Controlling the growth of future LEO debris populations with active debris removal. Acta Astronautica, 66(5):648 – 653.

Liou, J.-C. (2011). An active debris removal parametric study for LEO environment remediation. Advances in Space Research, 47(11):1865 – 1876.

Liou, J.-C., Corsaro, R., Giovane, F., Anderson, C., Sadilek, A., Burchell, M., and Hamilton, J. (2015). Dragons-a micrometeoroid and orbital debris impact sensor.

Liou, J.-C. and Johnson, N. (2009). Characterization of the cataloged fengyun-1c fragments and their long-term effect on the leo environment. Advances in Space Research, 43(9):1407 – 1415.

Liou, J.-C., Matney, M. J., Anz-Meador, P. D., Kessler, D., Jansen, M., and Theall, J. R. (2002). The new NASA orbital debris engineering model ORDEM2000. NASA STI/Recon Technical Report N.

Loft, K., Price, M. C., Cole, M. J., and Burchell, M. J. (2013). Impacts into metals targets at velocities greater than 1 km/s: A new online resource for the hypervelocity impact community and an illustration of the geometric change of debris cloud impact patterns with impact velocity. International Journal of Impact Engineering, 56:47–60.

Loftus, J., Christiansen, E., Schneider, W., and Hasselbeck, M. (1997). Shuttle modifications for station support. 48th International Astronautical Congress, (IAF-97-IAF.I.3.08).

Maas, D., Gller, J., Grn, E., Lange, G., McDonnell, J., Nappo, S., Perry, C., and Zarnecki, J. (1989). Cometary dust particles detected by the DIDSY-IPM-P sensor on board GIOTTO. Advances in Space Research, 9(3):247 – 252.

McBride, N., Green, S. F., and McDonnell, J. (1999). Meteoroids and small sized debris in Low Earth Orbit and at 1 au: Results of recent modelling. Advances in Space Research, 23(1):73–82.

McDonnell, J., Ratcliff, P., Green, S. F., McBride, N., and Collier, I. (1997). Microparticle Populations at LEO altitudes: Recent spacecraft measurements. Icarus, 127(1):55–64.

Mitri, G., Postberg, F., Soderblom, J. M., Wurz, P., Tortora, P., Abel, B., Barnes, J. W., Berga, M., Carrasco, N., Coustenis, A., et al. (2018). Explorer of enceladus and titan (e2t): Investigating ocean worlds' evolution and habitability in the solar system. Planetary and Space Science, 155:73–90.

National Research Council and others (1995). Orbital debris: A technical assessment. National Academies Press.

Nazarenko, A. and Usovik, I. (2013). Gravitation effect on a flux of sporadic micrometeoroids in the vicinity of near-Earth orbits. Acta Astronautica, 84(Supplement C):153 – 160.

Ortner, H. and Stadermann, F. (2009). Degradation of space exposed surfaces by hypervelocity dust bombardment, and refractory materials for space. International Journal of Refractory Metals and Hard Materials, 27(6):949 – 956.

Perkins, M., Simpson, J., and Tuzzolino, A. (1985). A cometary and interplanetary dust experiment on the Vega spacecraft missions to Halley's Comet. Nuclear Instruments and Methods in Physics Research Section A: Accelerators, Spectrometers, Detectors and Associated Equipment, 239(2):310 – 323.

Poppe, A., James, D., and Hornyi, M. (2011). Measurements of the terrestrial dust influx variability by the cosmic dust experiment. Planetary and Space Science, 59(4):319 – 326.

Porco, C. C. (2017). A Community Grows around the Geysering World of Enceladus. In Astrobiology, volume 17, page 815.

Postberg, F., Kempf, S., Hillier, J., Srama, R., Green, S., McBride, N., and Grn, E. (2008). The E-ring in the vicinity of Enceladus: II. Probing the moon's interiorThe composition of E-ring particles. Icarus, 193(2):438 – 454.

Povarnitsyn, M. E., Khishchenko, K. V., and Levashov, P. R. (2008). Simulation of melting and vaporization of metals at hypervelocity impact. Journal of Physics: Conference Series, 98(4):042025.

Reinhard, R. (1982). The Giotto mission to Halley's comet. Advances in Space Research, 2(12):97 – 107.

Rickman, S. L., Richards, W. L., Christiansen, E. L., Piazza, A., Pena, F., and Parker, A. R. (2017). Micrometeoroid/Orbital Debris (MMOD) Impact Detection and Location Using Fiber Optic Bragg Grating Sensing Technology. Procedia Engineering, 188(Supplement C):233 – 240.

Sanchez-Ortiz, N., Bell-Mora, M., and Klinkrad, H. (2006). Collision avoidance manoeuvres during spacecraft mission lifetime: Risk reduction and required IV. Advances in Space Research, 38(9):2107 – 2116.

Schaub, H., Jasper, L. E., Anderson, P. V., and McKnight, D. S. (2015). Cost and risk assessment for spacecraft operation decisions caused by the space debris environment. Acta Astronautica, 113(Supplement C):66 – 79.

Severin, D. (2008). Study of the degradation process of polyimide induced by high energetic ion irradiation. Thesis submitted for PhD.

Shams, A., Panteghini, A., Bardella, L., and Porfiri, M. (2017). A micromechanical model to study failure of polymer-glass syntactic foams at high strain rates. Computational Materials Science, 135(Supplement C):189 – 204.

Simpson, J., Sagdeev, R., Tuzzolino, A., Perkins, M., Ksanfomality, L., Rabinowitz, D., Lentz, G., Afonin, V., Erö, J., Keppler, E., et al. (1986). Dust counter and mass analyser (DUCMA) measurements of comet Halley's coma from Vega spacecraft. Nature, 321(6067):278–280.

Simpson, J. and Tuzzolino, A. (1985). Polarized polymer films as electronic pulse detectors of cosmic dust particles. Nuclear Instruments and Methods in Physics Research Section A: Accelerators, Spectrometers, Detectors and Associated Equipment, 236(1):187–202.

Skinner, M. A. (2017). Orbital debris: What are the best near-term actions to take? a view from the field. Journal of Space Safety Engineering, 4(2):105 – 111.

Spahn, F., Albers, N., Hrning, M., Kempf, S., Krivov, A. V., Makuch, M., Schmidt, J., Sei, M., and Sremevi, M. (2006a). E ring dust sources: Implications from Cassini's dust measurements. Planetary and Space Science, 54(9):1024 – 1032.

Spahn, F., Schmidt, J., Albers, N., Hörning, M., Makuch, M., Seiß, M., Kempf, S., Srama, R., Dikarev, V., Helfert, S., et al. (2006b). Cassini dust measurements at Enceladus and implications for the origin of the E ring. Science, 311(5766):1416–1418.

Srama, R., McDonnell, J. A. M., Tuzzolino, A. J., and et al. (2004). The Cassini Cosmic Dust Analyzer. Space Science Reviews, 1(114):465–518.

Sridharan, R. and Pensa, A. F. (1998). US Space Surveillance Network Capabilities. In Image Intensifiers and Applications; and Characteristics and Consequences of Space Debris and Near-Earth Objects, volume 3434, pages 88–101.

Thomas, N. and Keller, H. U. (1988). Fine dust structures in the emission of comet P/Halley observed by the Halley Multicolour Camera on board Giotto, pages 843–846. Springer Berlin Heidelberg, Berlin, Heidelberg.

Throop, H. B. and Esposito, L. W. (1998). G ring particle sizes derived from ring plane crossing observations. Icarus, 131(1):152 – 166.

Tuzzolino, A., Economou, T., McKibben, R., Simpson, J., BenZvi, S., Blackburn, L., Voss, H., and Gursky, H. (2005). Final results from the space dust (SPADUS) instrument flown aboard the earth-orbiting ARGOS spacecraft. Planetary and Space Science, 53(9):903 – 923.

Tuzzolino, A. J., Economou, T. E., McKibben, R., Simpson, J., McDonnell, J., Burchell, M. J., Vaughan, B., Tsou, P., Hanner, M., Clark, B., et al. (2003). Dust flux monitor instrument for the stardust mission to comet wild 2. Journal of Geophysical Research: Planets, 108(E10).

Whipple, F. L. (1947). Meteorites and Space Travel. The Astronomical Journal, 52:131–139.

Whittet, D. C. B. (1989). The Composition of Dust in Stellar Ejecta, pages 455–466. Springer Netherlands, Dordrecht.

Wiegert, P., Vaubaillon, J., and Campbell-Brown, M. (2009). A dynamical model of the sporadic meteoroid complex. Icarus, 201(1):295 – 310.

Willis, P. B. and Hsieh, C.-H. (2000). Space applications of polymeric materials. Kobunshi, 49(2):52–56.

Ye, S., Gurnett, D., and Kurth, W. (2016). In-situ measurements of Saturn's dusty rings based on dust impact signals detected by Cassini RPWS. Icarus, 279(Supplement C):51 – 61.

Zhukovska, S., Gail, H.-P., and Trieloff, M. (2008). Evolution of interstellar dust and stardust in the solar neighbourhood. A&A, 479:453–480.

Zolensky, M. E., Zook, H. A., Horz, F., Atkinson, D. R., Coombs, C. R., Watts, A. J., Dardano, C. B., See, T. H., Simon, C. G., and Kinard, W. H. (1992). Interim report of the meteoroid and debris special investigation group.

Zook, H., McKay, D., and Bernhard, R. (1990). Results from returned spacecraft surfaces. In Orbital Debris Conference: Technical Issues andFuture Directions, page 1349.

Appendix A

Experiment Details

Appendix A includes tables of all the experiments conducted throughout this research with references to their Kent shot ID numbers. It should be noted that in some cases multiple experiments were conducted during the same shot as multiple subsystems could be tested simultaneously. For example experiments ICC-3.04, ICC-3.07 and ICC-3.08 were conducted during the same shots as experiments UVT-1.01, UVT-1.02 and UVT-1.03, respectively.

Table A.1: ICC-1 Experiments

Experiment	Kent Shot ID	Diameter	Velocity	Impact Angle	Material
ICC-1.01	G140515#1	1.0	4.90	0.0	Stainless Steel
ICC-1.02	G140515#2	2.0	5.00	0.0	Stainless Steel
ICC-1.03	G140515#3	0.8	5.04	0.0	Stainless Steel
ICC-1.04	G040615#1	0.5	5.05	0.0	Stainless Steel
ICC-1.05	G110615#1	0.4	5.08	0.0	Stainless Steel
ICC-1.06	G140815#1	1.5	5.04	0.0	Stainless Steel
ICC-1.07	G301015#1	0.3	4.47	0.0	Stainless Steel

Table A.2: ICC-2 Experiments

Experiment	Kent Shot ID	Diameter	Velocity	Impact Angle	Material
ICC-2.01	G140116#1	0.3	5.25	0.0	Stainless Steel
ICC-2.02	G210116#1	0.8	4.93	0.0	Stainless Steel
ICC-2.03	G210116#2	0.5	5.31	0.0	Stainless Steel
ICC-2.04	G120216#1	1.0	4.93	0.0	Stainless Steel
ICC-2.05	G150216#1	0.4	5.17	0.0	Stainless Steel
ICC-2.06	G250216#1	0.1	5.07	0.0	Stainless Steel

Table A.3: ICC-3 Experiments

Experiment	Kent Shot ID	Diameter	Velocity	Impact Angle	Material
ICC-3.01	G110417#1	1.0	4.61	0.0	Stainless Steel
ICC-3.02	G110417#2	1.5	3.16	0.0	Stainless Steel
ICC-3.03	G110417#3	1.0	2.97	0.0	Stainless Steel
ICC-3.04	G120417#1	0.8	2.93	0.0	Stainless Steel
ICC-3.05	G120417#2	0.5	3.09	0.0	Stainless Steel
ICC-3.06	G120417#3	0.3	3.04	0.0	Stainless Steel
ICC-3.07	G130417#1	0.8	4.99	30.0	Stainless Steel
ICC-3.08	G130417#2	0.8	4.88	15.0	Stainless Steel

Table A.4: UVT-1 Experiments

Experiment	Kent Shot ID	Diameter	Velocity	Impact Angle	Material
UVT-1.01	G120417#1	0.8	2.93	0.0	Stainless Steel
UVT-1.02	G130417#1	0.8	4.99	30.0	Stainless Steel
UVT-1.03	G130417#2	0.8	5.00	15.0	Stainless Steel

Table A.5: IGV-1 Experiments

Experiment	Kent Shot ID	Diameter	Velocity	Impact Angle	Material
IGV-1.01	G110417#1	1.0	4.61	0.0	Stainless Steel
IGV-1.02	G110417#2	1.5	3.16	0.0	Stainless Steel
IGV-1.03	G110417#3	1.0	2.97	0.0	Stainless Steel
IGV-1.04	G120417#1	0.8	2.93	0.0	Stainless Steel
IGV-1.05	G120417#2	0.5	3.09	0.0	Stainless Steel
IGV-1.06	G120417#3	0.3	3.04	0.0	Stainless Steel
IGV-1.07	G130417#1	0.8	4.99	30.0	Stainless Steel
IGV-1.08	G130417#2	0.8	4.88	15.0	Stainless Steel

Table A.6: PTD-1 Experiments

Experiment	Kent Shot ID	Diameter	Velocity	Impact Angle	Material
PTD-1.01	G301015#1	0.3	4.47	0.0	Stainless Steel
PTD-1.02	G110615#1	0.4	5.08	0.0	Stainless Steel
PTD-1.03	G040615#1	0.5	5.05	0.0	Stainless Steel
PTD-1.04	G140515#3	0.8	5.04	0.0	Stainless Steel
PTD-1.05	G140515#1	1.0	4.90	0.0	Stainless Steel
PTD-1.06	G140815#1	1.5	5.04	0.0	Stainless Steel
PTD-1.07	G140515#2	2.0	5.00	0.0	Stainless Steel

Table A.7: PTD-2 Experiments

Experiment	Kent Shot ID	Diameter	Velocity	Impact Angle	Material
PTD-2.01	G250216#1	0.1	5.07	0.0	Stainless Steel
PTD-2.02	G140116#1	0.3	5.25	0.0	Stainless Steel
PTD-2.03	G150216#1	0.4	5.17	0.0	Stainless Steel
PTD-2.04	G210116#2	0.5	5.31	0.0	Stainless Steel
PTD-2.05	G210116#1	0.8	4.93	0.0	Stainless Steel
PTD-2.06	G120216#1	1.0	4.93	0.0	Stainless Steel
PTD-2.07	G110417#1	1.0	4.61	0.0	Stainless Steel
PTD-2.08	G130417#1	0.8	4.99	30.0	Stainless Steel
PTD-2.09	G130417#2	0.8	5.00	15.0	Stainless Steel

Table A.8: PTD-3 Experiments

Experiment	Kent Shot ID	Diameter	Velocity	Impact Angle	Material
PTD-3.01	G120417#3	0.3	3.04	0.0	Stainless Steel
PTD-3.02	G120417#2	0.5	3.09	0.0	Stainless Steel
PTD-3.03	G120417#1	0.8	2.93	0.0	Stainless Steel
PTD-3.04	G110417#3	1.0	2.97	0.0	Stainless Steel
PTD-3.05	G110417#2	1.5	3.16	0.0	Stainless Steel

Table A.9: PTE-1 Experiments

Experiment	Kent Shot ID	Diameter	Velocity	Impact Angle	Material
PTE-1.01	G140416#3	0.3	5.06	0.0	Stainless Steel
PTE-1.02	G020616#1	1.0	1.99	0.0	Aluminium
PTE-1.03	G020616#2	1.0	2.11	0.0	Titanium
PTE-1.04	G140416#2	0.5	5.14	0.0	Stainless Steel
PTE-1.05	G280416#2	1.0	2.04	0.0	Stainless Steel
PTE-1.06	G120516#1	1.0	3.12	0.0	Stainless Steel
PTE-1.07	G020616#3	1.0	2.04	0.0	Tungsten Carbide
PTE-1.08	G280416#1	0.8	5.01	0.0	Stainless Steel
PTE-1.09	G180516#1	1.0	4.22	0.0	Stainless Steel
PTE-1.10	G140416#1	1.0	4.99	0.0	Stainless Steel

Table A.10: PTE-2 Experiments

Experiment	Kent Shot ID	Diameter	Velocity	Impact Angle	Material
PTE-2.01	G120417#3	0.3	3.04	0.0	Stainless Steel
PTE-2.02	G120417#2	0.5	3.09	0.0	Stainless Steel
PTE-2.03	G120417#1	0.8	2.93	0.0	Stainless Steel
PTE-2.04	G110417#3	1.0	2.97	0.0	Stainless Steel
PTE-2.05	G110417#2	1.5	3.16	0.0	Stainless Steel
PTE-2.06	G250216#1	0.1	5.07	0.0	Stainless Steel
PTE-2.07	G150216#1	0.4	5.17	0.0	Stainless Steel
PTE-2.08	G210116#2	0.5	5.31	0.0	Stainless Steel
PTE-2.09	G210116#1	0.8	4.93	0.0	Stainless Steel
PTE-2.10	G120216#1	1.0	4.93	0.0	Stainless Steel

Appendix B

Supplementary Items

Appendix B includes screenshots of a raw data file and lookup table. Additionally, Python scripts that were used to calculate impact locations (ICC), time delays and PT amplitudes (PTD and PTE) are included below. The algorithms for the velocity (IGV) and trajectory (UVT) calculations were trivial and therefore performed in Excel.

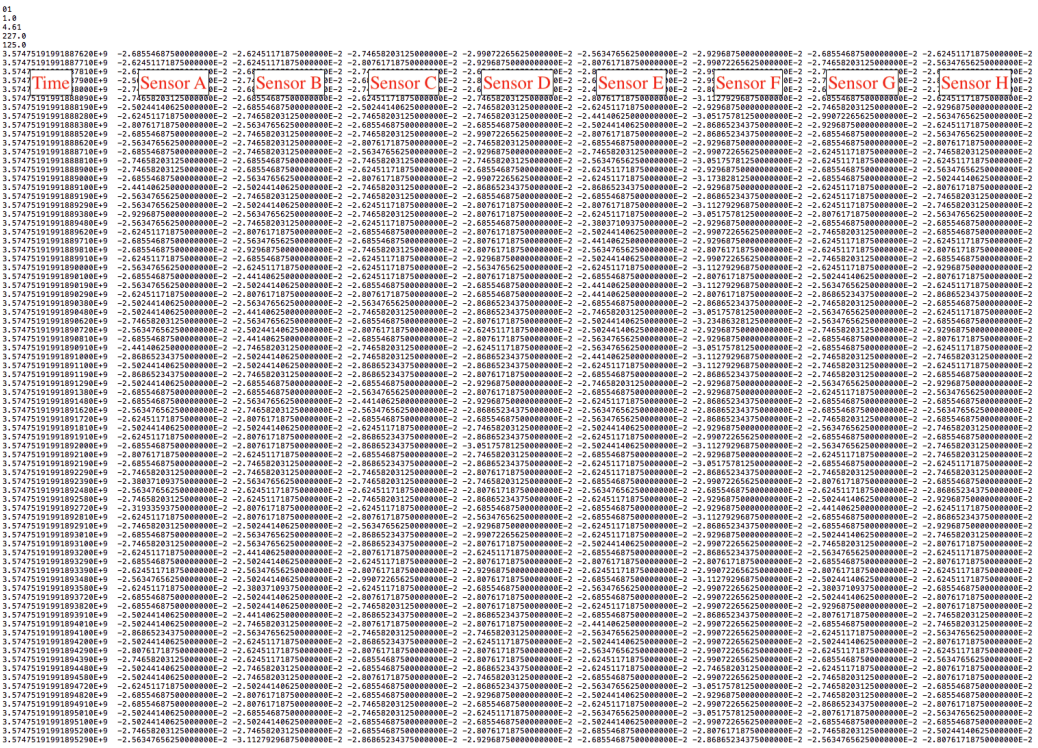

Figure B.1: Example of a raw data file, where the first, second, third, fourth and fifth rows describe the shot number in the series, projectile diameter, impact velocity, x-coordinate and y-coordinate, respectively. The first column represents the time and the remaining columns represent the voltage recorded by the PVDF sensors.

```
x y tdA tdB tdD
194 0 151 151 0
194 1 150 150 0
194 2 150 150 0
194 3 149 149 0
194 4 149 149 0
194 5 148 148 0
194 6 147 147 0
194 7 147 147 0
194 8 146 146 0
194 9 146 146 0
194 10 145 145 0
194 11 144 144 0
194 12 144 144 0
194 13 143 143 0
194 14 143 143 0
194 15 142 142 0
194 16 141 141 0
194 17 141 141 0
194 18 140 140 0
194 19 140 140 0
194 20 139 139 0
194 21 138 138 0
194 22 138 138 0
194 23 137 137 0
194 24 136 136 0
194 25 136 136 0
194 26 135 135 0
```

Figure B.2: Example of a section of a (C-quadrant) lookup table, where the columns x, y, tdA, tdB and tdD represent the x-coordinate, y-coordinate and signal time delay at sensor A, B and D, respectively.

```
import matplotlib.pyplot as plt
from pylab import *
from numpy import *
import os

array = loadtxt('/Users/[redacted]/Impact_Coordinates/SC.txt',skiprows=1,unpack=True)

shot = 4

tdA = 133
tdB = 66
tdD = 85

error = 3

results = [] #This is defining a list

for line in range(0,len(array[0])):
    if array[2,line] >tdA-error and array[2,line] <tdA+error:
        if array[3,line] >tdB-error and array[3,line] <tdB+error:
            if array[4,line] >tdD-error and array[4,line] <tdD+error:
                results.append(array[0:2,line]) # Writes the temp values into the results list.

#fout.write('%s'%(results))
savetxt('/Users/[redacted]/Impact_Coordinates/results/159/Array_Odin3P_S%.0f_159.txt'%(shot),results,fmt='%.0f')

savetxt('/Users/[redacted]/Impact_Coordinates/results/temp.txt',results,fmt='%.0f')

colx, coly = loadtxt('/Users/[redacted]/Impact_Coordinates/results/temp.txt',unpack=True)

x=(max(colx)+min(colx))/2
y=(max(coly)+min(coly))/2

temp = (x, y)

fout=open('/Users/[redacted]/Impact_Coordinates/results/159/Odin3P_S%.0f_coordinate_159'%(shot),'w')

fout.write('%.1f %.1f'%(temp[0],temp[1]))
```

Figure B.3: Python script used by the ICC to calculate the location of an impact from a lookup table.

```
import matplotlib.pyplot as plt
import numpy as np
import os

colT, colA, colB, colC, colD, col6, col7, col8, col9 = np.loadtxt('/Users/[redacted]/Time_Delays/Data/
seriesOdintwo_shot2.txt',skiprows=5,unpack=True) # This calls in the data from the collumns but skips the first row.

time = np.arange(1,len(colT)+1) #This replaces all the time values and orders them 1 to 3000 in increments of 1.

i = 480 ####### Use data between i and f
f = 640 ####### Use data between i and f

data_A =colA[i:f]
data_B =colB[i:f]
data_C =colC[i:f]
data_D =colD[i:f]

max_A = max(data_A)  # Find the maximum acoustic signal in data_y
tA = i + time[data_A.argmax()]  # Find the time of maximum signal

max_B = max(data_B)
tB = i + time[data_B.argmax()]

max_C = max(data_C)
tC = i + time[data_C.argmax()]

max_D = max(data_D)
tD = i + time[data_D.argmax()]

t0=tD ######### ts equals the sensor which receives signal first. Eg ts=tA means the impact occured in quadrant A.

tdA = tA-t0
tdB = tB-t0 # Finds the delay between S0 and Sx hearing signal
tdC = tC-t0
tdD = tD-t0

print tA
print tB
print tC
print tD

print tdA
print tdB
print tdC
print tdD
```

Figure B.4: Python script used by the ICC to calculate the time delay of signals at each sensor.

```
import matplotlib.pyplot as plt
from pylab import *
from numpy import *
import os

colT, colA, colB, colC, colD, colE, colF, colG, colH = loadtxt('/Users/[redacted]/odin3/PP_Amplitude/txt_data/
Odin3_shot1.txt',skiprows=5,unpack=True)

shot_no, diameter, vel, x_co, y_co = genfromtxt('/Users/[redacted]/odin3/PP_Amplitude/txt_data/Odin3_shot1.txt',max_rows=5,unpack=True)

# Finds distance from impact to each sensor

dA = sqrt((x_co)**2.0+(388.0-y_co)**2.0)
dB = sqrt((382.0-x_co)**2.0+(388.0-y_co)**2.0)
dC = sqrt((382.0-x_co)**2.0+(y_co)**2.0)
dD = sqrt((x_co)**2.0+(y_co)**2.0)

# Selects useful data

data_A = colA[600:750]
data_B = colB[600:750]
data_C = colC[600:750]
data_D = colD[600:750]

# Calculate p/p amp for each sensor

pp_A = max(data_A) - min(data_A)
pp_B = max(data_B) - min(data_B)
pp_C = max(data_C) - min(data_C)
pp_D = max(data_D) - min(data_D)

# Calculates normalised p/p amp for each sensor at a distance of 250 mm

pp_A_250 = pp_A*sqrt(dA/250.0)
pp_B_250 = pp_B*sqrt(dB/250.0)
pp_C_250 = pp_C*sqrt(dC/250.0)
pp_D_250 = pp_D*sqrt(dD/250.0)

av_pp_250 =(pp_A_250 + pp_B_250 + pp_C_250 + pp_D_250)/4.0

print "Peak-to-Peak Amplitude"
print av_pp_250
```

Figure B.5: Python script used by the PTD and PTE to calculate the PT amplitude of an acoustic signal.